# INFORMATION TO USERS

This manuscript has been reproduced from the microfilm master. UMI films the text directly from the original or copy submitted. Thus, some thesis and dissertation copies are in typewriter face, while others may be from any type of computer printer.

**The quality of this reproduction is dependent upon the quality of the copy submitted.** Broken or indistinct print, colored or poor quality illustrations and photographs, print bleedthrough, substandard margins, and improper alignment can adversely affect reproduction.

In the unlikely event that the author did not send UMI a complete manuscript and there are missing pages, these will be noted. Also, if unauthorized copyright material had to be removed, a note will indicate the deletion.

Oversize materials (e.g., maps, drawings, charts) are reproduced by sectioning the original, beginning at the upper left-hand corner and continuing from left to right in equal sections with small overlaps. Each original is also photographed in one exposure and is included in reduced form at the back of the book.

Photographs included in the original manuscript have been reproduced xerographically in this copy. Higher quality 6" x 9" black and white photographic prints are available for any photographs or illustrations appearing in this copy for an additional charge. Contact UMI directly to order.

**UMI**

A Bell & Howell Information Company
300 North Zeeb Road, Ann Arbor MI 48106-1346 USA
313/761-4700 800/521-0600

# ULTRAFAST SPECTROSCOPY
# IN
# BIOLOGICAL AND ORGANIC MATERIALS

by

**GUANG BAI**

A dissertation submitted to the Graduate Faculty in Physics in partial fulfillment of the requirement for the degree of Doctor of Philosophy, The City University of New York.

•1997•

This manuscript has been read and accepted for the Graduate Faculty in Physics in satisfaction of the dissertation requirement for the degree of Doctor in Philosophy.

7/11/97
Date

Chairman of the Examining Committee:
**Dr. Robert R. Alfano,** Distinguished Professor of Science and Engineering, Department of Physics and Department of Electrical Engineering, The City College of The City University of New York.

July 10, 1997
Date

Executive Officer
**Dr. Louis Celenza**

| | |
|---|---|
| **Dr. Robert H. Callender** | Distinguished Professor of Physics and Biochemistry, Department of Physics, The City College of The City University of New York. |
| **Dr. Nan-Loh Yang** | Professor of Chemistry, Department of Chemistry, The College of Staten Island of The City University of New York. |
| **Dr. Anshel A. Gorokhovsky** | Associate Professor of Physics, Department of Applied Sciences, The College of Staten Island of The City University of New York. |
| **Dr. Lewis Rothberg** | Professor of Chemistry, Department of Chemistry, University of Rochester, Rochester, New York. |

Supervisory Committee

The City University of New York

# Abstract

# ULTRAFAST SPECTROSCOPY IN BIOLOGICAL AND ORGANIC MATERIALS

by

**Guang Bai**

**Advisor: Professor Robert R. Alfano**

This thesis consists of an experimental investigation of the dynamics of the biological material, visual pigment rhodopsin, and the persistent hole burning material, octaethylpophine-doped polystyrene(OEP/PS), utilizing femtosecond laser spectroscopy.

The *cis-trans* isomerization of the retinal chromophore in rhodopsin at ambient temperature has been studied by employing a novel three beam femtoscond transient absorption method, and a new model is proposed. Two-thirds of the excited rhodopsin molecules isomerize promptly via curve-crossing to form bathorhodopsin in ~200 femtoseconds. The remaining third will miss curve-crossing and stay in the excited state, which never isomerizes and decays to the ground state rhodopsin in ~3 picoseconds. These results are consistent with recent two-beam femtosecond transient experiments[1-6] and agree well with molecular dynamics calculations[7-8]. The three-beam pump-probe measurement is an important technical advance in the characterization of transient species in the initial step of vision, which directly measures the formation dynamics of the ground state species. Using this technique, we could drive the bathorhodopsin back into

rhodopsin. This is the first experimental evidence of *trans* to *cis* formation of rhodopsin at ambient temperature.

The characteristic parameters and phototransformation pathway of OEP/PS have been studied for optical storage applications. Femtosecond accumulated photon echo and time-resolved absorption spectroscopy were used. The optical dephasing time $T_2$ for a laser bandwidth covering the whole inhomogeneous zero-phonon absorption band is $200 \pm 50$ ps at 1.4 K. $T_2$ reduces significantly to 100 ps when the temperature increases to 4.2 K. This temperature dependence indicates that OEP/PS must operate at very low temperatures. The saturation dose is 6 J/cm$^2$. The maximum number of readings is equivalent to the same amount of energy of writing. 150 fs single-shot detection of a 4-bit packet stored in an OEP/PS sample has been demonstrated for the first time by a novel low-intensity interferometric cross-correlation technique[9], which corresponds to a data readout speed of 27 Tbits/sec. With stimulated emission from the first excited state $S_1$ at 680 nm in addition to a 620 nm writing beam, the phototransformation pathway is altered, leading to a hole burning rate twice as large as the one without stimulated emission.

**Dedicated to Qian, Laura and Jeffrey.**

# Acknowledgments

I wish to thank my thesis advisor Professor Robert R. Alfano for introducing me to the ultrafast laser field. His broad knowledge and deep understanding in this field, and his patience, led me to complete my thesis. I thank Professor Robert Callender, Professor Lewis Rothberg, Professor Anshel Gorokhovsky and Professor Nan-Loh Yang for their expert help in vision, hole burning and laser spectroscopy. I also thank Dr. Iosif Zeylikovich for his expertise in optical storage and interference gating. I thank Dr. Ming Yan for teaching me the laser systems and helpful discussions in vision research. I also thank Dr. Liwen Huang for his expertise in teaching me the rhodopsin sample preparation. I thank Dr. Nathan Ockman for the proofreading of this thesis. I also thank Professor Ping-Pei Ho, Professor Kai Shum, Dr. Quanzhen Wang, Dr. Nick Zhadin, Mr. Alexey Turukhin, Dr. Wubao Wang, Dr. Swapan Gayen, Prof. Feng Liu, Dr. Chenghui Liu, Dr. Guichen Tang, Ms. Xiangchun Liang, Dr. Leming Wang, Ms. Dana Calistru, Mr. Gang Zhang, Ms. Yici Guo, Mr. Leander Kalpaxis, Ms. Megan Gibbs, Ms. Joan Brijlall and other IUSL friends for helpful discussions and their kindly assistance.

This work is dedicated with respect and love to my parents, Jingde Bai and Peixuan Qi. They provided my college education and encouraged me on my pursuing the advanced degree. This work is also dedicated to my parents-in-law, Boru Tang and Wenying Yu, for their help in taking care of my daughter and son so that I could complete writing this thesis. This thesis is also dedicated to my wife Qian, my daughter Laura and my son Jeffrey.

# Table of Contents

# List of Tables

# List of Figures

# Chapter 1

# Introduction

## 1.1) Ultrafast Processes in Biological and Organic Materials

Ultrafast laser spectroscopic techniques[10-12] has been used to significantly advance investigations in rapid physical, chemical and biological phenomena. The high time resolution attained and broad spectral range covered allow for new and deeper insights into the nature, and especially, into the temporal evolution of some fundamental processes in biological and organic materials. Vibrational energy exchange, molecular structural rearrangement, electronic relaxation and temperature fluctuation processes[13-16] are a few examples. The nature of the primary photochemical process in vision has long been a subject of extensive research. In such a system, optical excitation results in the distortion of the delocalized electronic distribution, which leads to the extremely fast molecular structure changes of the chromophore from 11-*cis* to the all-*trans* configuration with significant shifting of the absorption spectrum. A number of mechanisms were proposed and it was a subject of debate[17-29]. A clear understanding of such an ultrafast process will improve our basic knowledge about the fundamental properties of this important class of bio-systems, such as how nature has optimized the photochemistry of the visual pigment rhodopsin. It may also be beneficial to potential applications which may require the manipulation of the protein, synthesis of new molecular systems, and the optimization of photonic performance of potential devices.

The demand for high-speed and high-density memories has stimulated the investigation of new materials for optical data storage. Large efforts have been made to use biological molecules and organic materials for optical memory devices. The photochemistry in the visual system mentioned above is a well known fast process[1-6], which may have a potential application for a high speed optical switch. In optical memory techniques, a fundamental limitation on data density is imposed by the dimension of the diffraction spot. It has been suggested that this limitation in 3-D space could be overcome by the addition of a fourth dimension - the spectral domain - to the storage volume[30-31]. Persistent spectral hole burning(PHB) techniques provide such state of the art applications. Dye-doped polymers at low temperature are hole burning materials available for optical memory, for example, octaethylporphine-doped polystyrene(OEP/PS). When the OEP/PS sample is exposed to a laser light at very low temperature, the central hydrogens in the porphyrin ring will change orientation and a persistent spectral hole is burned in its inhomogeneously broadened absorption band centered at the laser frequency. Since the phase relaxation time for these materials is in the nanosecond time scale or less, picosecond or subpicosecond data pulses must be employed to achieve high data density when time-domain PHB storage is used. Thus fast detection and analysis systems are also required.

The femtosecond time-resolved interferometry technique can be employed to achieve ultrafast detection[9] for optical storage. The future applications for high speed signal processing and high density optical data storage using the unique nature of biological and organic materials depends on our understanding of the basic properties of these materials. The processes in which light interacts with these materials are themselves

very interesting topics in physics. The study of the dynamics of such materials is important both for application and fundamental research. Ultrafast spectroscopy makes it possible for temporal spectroscopic studies in such materials in the time range of $10^{-10}$ to $10^{-14}$ second.

## 1.2) Thesis Statement

The focus of my thesis research is to study the ultrafast phenomena associated with the structural rearrangements after photoexcitation of organic materials utilizing femtosecond spectroscopy and interferometry. The two important organic materials in this study are the visual pigment rhodopsin and the persistent hole burning(PHB) optical storage material octaethylporphine-doped polystyrene(OEP/PS). In the study of the primary event of vision, a novel femtosecond transient absorption measurement was performed to obtain information on the dynamics of the initial molecular structural change from rhodopsin(11-*cis*) to bathorhodopsin(all-*trans*). In OEP/PS, the central hydrogens change orientation after photoexcitation. The femtosecond accumulated echo method was employed to characterize dephasing, saturation and other processes involved in the OEP/PS persistent hole burning. The emphasis of the research is on the application of optical memory. Terabit speed of information retrieval based on the PHB accumulated photon echo is achieved by a novel femtosecond single shot cross-correlation interferometric method. The writing efficiency is improved by altering the natural pathway of photochemistry with stimulated emission from the first excited state $S_1$.

## 1.3) Thesis Outline

In Chapter 1, a general introduction of the thesis, the thesis statement and the thesis outline are presented.

In Chapter 2, the CPM femtosecond laser and amplification system used in this thesis research is introduced. A brief review on the ultrafast laser generation technique, modelocking, pulse compression and supercontinuum generation is given. The experimental methods used in this thesis, including the 3-beam pump-probe method for vision measurement, the special amplitude correlator for ultrafast information retrieval on the optical storage material OEP/PS and the stimulated emission setup for efficient writing on OEP/PS are described in detail.

Chapters 3 to 5 focus on the research on primary events in vision. In Chapter 3, the structure of visual pigment rhodopsin and the background of the visual process, especially the primary event are described. Chapter 4 presents various previous experimental research on the primary events of vision, including resonance Raman spectroscopy, fluorescence kinetic measurements and transient absorption measurements. It also describes the models and theoretical simulations based on such research. In Chapter 5, the discrepancy between two important models are discussed. A new experiment is designed and performed using a modified 3-beam pump-probe method. The results establish a new model for primary events of vision.

Chapters 6 to 8 focus on the ultrafast information retrieval and writing on the persistent hole burning optical storage material OEP/PS. In Chapter 6, the background of persistent hole burning optical storage is provided, including the frequency domain and

time domain approaches. In Chapter 7, a set of preliminary experimental results for the characterization of OEP/PS are given, including the optical dephasing time, the saturation effect, the maximum reading dose and the temperature dependence of OEP/PS. In Chapter 8, the results of this thesis research on OEP/PS are presented. Section 8.1 describes the ultrafast information retrieval on OEP/PS using amplitude correlation technique. Section 8.2 describes the improvement of writing efficiency using the stimulated emission.

Future experiments on visual pigment rhodopsin and OEP/PS are discussed in Chapter 9.

## References


1. Ming Yan, D. Manor, G. Weng, H. Chao, L. Rothberg, T. M. Jedju, R. R. Alfano and R. H. Callender *Proc. Natl. Acad. Sci. (USA)* **88**, 9809(1991)

2. R. W. Schoenlein, L. A. Peteanu, R. A. Mathies, C. V. Shank *Science* **254**, 412(1991)

3. M. Yan and R. R. Alfano *Bio-Laser News* (Spring 1992)

4. M. Yan, D. Manor, R. R. Alfano and R. H. Callender, L. J. Rothberg *Proc. of the International Conference on Lasers '92, Dec. 7 - 10*, 422(1992)

5. L. A. Peteanu, R. W. Schoenlein, Q. Wang, R. A. Mathies and C. V. Shank *Proc. Natl. Acad. Sci. (USA)* **90**, 11762(1993)

6. Q. Wang, R. W. Schoenlein, L. A. Peteanu, R. A. Mathies and C. V. Shank *Science* **266**, 422(1994)

7. R. R. Birge, L. M. Hubbard *J. Am. Chem. Soc.* **102**, 2195(1980)

8. J. R. Tallent, E. W. Hyde, L. A. Findsen, G. L. Fox, R. R. Birge *J. Am. Chem. Soc.* **114**, 1581(1992)

9. I. Zeylikovich, G. Bai, A. Gorokhovsky and R. R. Alfano *Optics Letters* **20**, 749(1995)

10. R. L. Fork, C. V. Shank, R. Yen and C. A. Hirlimann *IEEE J. Quantum Electron.* **19**, 500(1983)

11. C. V. Shank in *Ultrafast Laser Pulses and Applications* ed. by W. Kaiser, Topics in Applied Physics **60**, Springer-Verlag, New York (1988)

12. D. J. Bradley in *Ultrafast Laser Pulses ch2* ed. by S. L. Shapiro, Springer-Verlag, New York (1977)

13. M. D. Levenson in *Introduction to Nonlinear Spectroscopy*, Academic Press, San Diego (1981)

14. P. M. Rentzpis *Science* **202**, 174(1978)

15. S. L. Shapiro ed. *Ultrashot light Pulses*, Springer-Verlag, New York (1977)

16. R. R. Alfano ed. *Biochemical events Probed by Ultrafast Laser Spectrascopy*, Academic Press, San Diego (1982)

17. K. Peters, M. Applebury and P. Rentzepis *Proc. Natl. Acad. Sci. U.S.A.* **74**, 3119(1977)

18. B. Green, T. Monger, R. Alfano, B. Aton and R. Callender *Nature (London)* **264**, 179(1977)

19. T. G. Monger, R. R. Alfano and R. H. Callender *Biophys. J.* **27**, 105(1979)

20. G. Busch, M. Applebury, A. Lamola and P. Rentzepis *Proc. Natl. Acad. Sci. U.S.A.* **69**, 2802(1972)

21. B. Honig, T. Ebrey, R. H. Callender, U. Dinur and M. Ottolenghi *Proc. Natl. Acad. Sci. U.S.A.* **76**, 2503(1979)

22. R. M. Weiss and A. Warshel *J. Am. Chem. Soc.* **101**, 6131(1979)

23. R. R. Birge, L. M. Hubbard *Biophys. J.* **34**, 517(1981)

24. K. Taiji, K. Bryl, M. Nakagawa, M. Tsuda and T. Kobayashi *Photochem. Photobiol.* **56**, 1003(1992)

25. Y. Shichida, S. Matuoka and T. Yoshizawa *Photobiochem. Photobiophys.* **7**, 221(1984)

26. H. Kandori, S. Matuoka, Y. Shichida and T. Yoshizawa *Photochem. Photobiol.* **49**, 181(1989)

27. H. Kandori, Y. Shichida and T. Yoshizawa *Biophys. J.* **56**, 453(1989)

28. A. Popp, L. Ujj and G. H. Atkinson *Journal of Physical Chemistry* **99**, 10043(1995)

29. T. Rosenfeld, B. Honig, M. Ottolenghi, j. Hurley and T. G. Ebrey *Pure Appl. Chem.* **49**, 341(1977)

30. A. Szabo, U.S. patent 3,896,420(July 22, 1975)

31. G. Castro, D. Haarer, R. M. Macfarlane and H. P. Trommsdroff, U.S. patent 4,101,976(July 18, 1978)

# Chapter 2

# Experimental Methods

This chapter introduces the experimental methods needed in the thesis to generate and detect ultrafast laser pulses.

## 2.1) Ultrafast Laser System

A Colliding Pulse Modelocking (CPM) dye laser oscillator, with a four stage amplifier, a pulse compressor, supercontinuum generation and amplification system were used in this thesis. A block diagram of the system is shown in Figure 2.1. The CPM ring dye laser is pumped by a cw Spectra-Physics® model 171 Argon laser and produces a 620 nm, 65 fs pulse of 40–80 pJ energy at a repetition rate of 120 MHz. The CPM pulses are amplified by a four stage dye amplifier, pumped by the second harmonic of a Quanta-Ray (Spectra-Physics®) Model DCR IIA Q-switched Nd:YAG laser with a repetition rate of 20 Hz. The amplified CPM pulse is compressed by a prism compressor to 100 fs with an energy of a few microjoules and is ready for supercontinuum generation through an ethylene glycol cell.

The amplification of various wavelengths selected by narrow band filters from the supercontinuum is achieved through a single stage dye amplifier pumped by either the second harmonic or third harmonic of the 1.06 μm leak from the Nd:YAG laser. The overall ultrafast laser system produces a 150 fs duration pump pulse of tunable

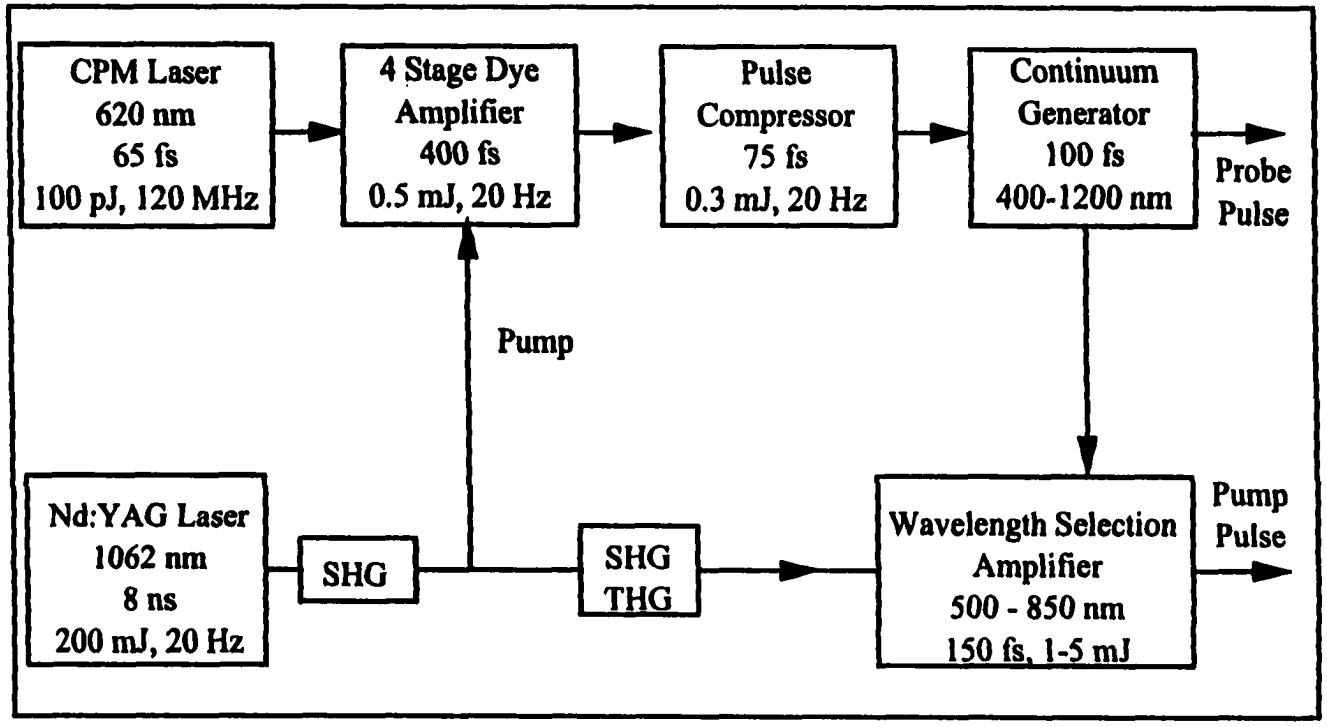


Fig. 2.1 Block diagram for the femtosecond tunable laser source. The range of the excitation wavelength is form 500 to 850 nm and the range of the probe wavelength is from 400 to 1400 nm.

wavelength from 500 nm to 850 nm, with a few microjoules of energy at a repetition rate of 20 Hz. It is capable of probing the wavelength range 400 nm to 1200 nm.

### 2.1.1 Generation of ultrafast laser pulses: the modelocking technique

The origin of the generation of an ultrafast laser pulse is connected to the fact that in laser materials having a relatively large bandwidth of the laser transition, very many longitudinal eigen modes can be simultaneously excited[1]. The total field strength

$$E(t) = \sum_{n=-(N-1)/2}^{(N-1)/2} \frac{1}{2} \hat{E}_n(t) e^{i(\omega_0 + n\omega)t + i\varphi_n} + C.C. \qquad (2.1)$$

of the laser radiation results from the superposition of the field strength $E_n$ of $N$ single longitudinal modes. $\Delta\nu = \omega / 2\pi = c / 2L$ is the frequency spacing between the allowed resonator modes, where $L$ is the optical path length of the laser resonator, and c is the speed of light. $\omega_0$ is the center frequency. The phases of various modes $\varphi_n$ can be statistically dependent or statistically independent of one another, depending on the properties of the active material and the resonator. In typical continuous-wave lasers, the phases $\varphi_n$ are likely to vary randomly with time, causing the intensity of the laser output to fluctuate randomly due to random interference between modes. In this case of statistically independent, fluctuating phases $\varphi_n$, the total intensity can be represented as the sum of the intensities of the individual mode

$$I \sim \overline{E(t)^2} = \sum_n \frac{1}{2} \left| \hat{E}_n \right|^2 . \qquad (2.2)$$

In the time domain, the field consists of an intensity distribution that has the characteristic properties of Gaussian noise as depicted in figure 2.2a.

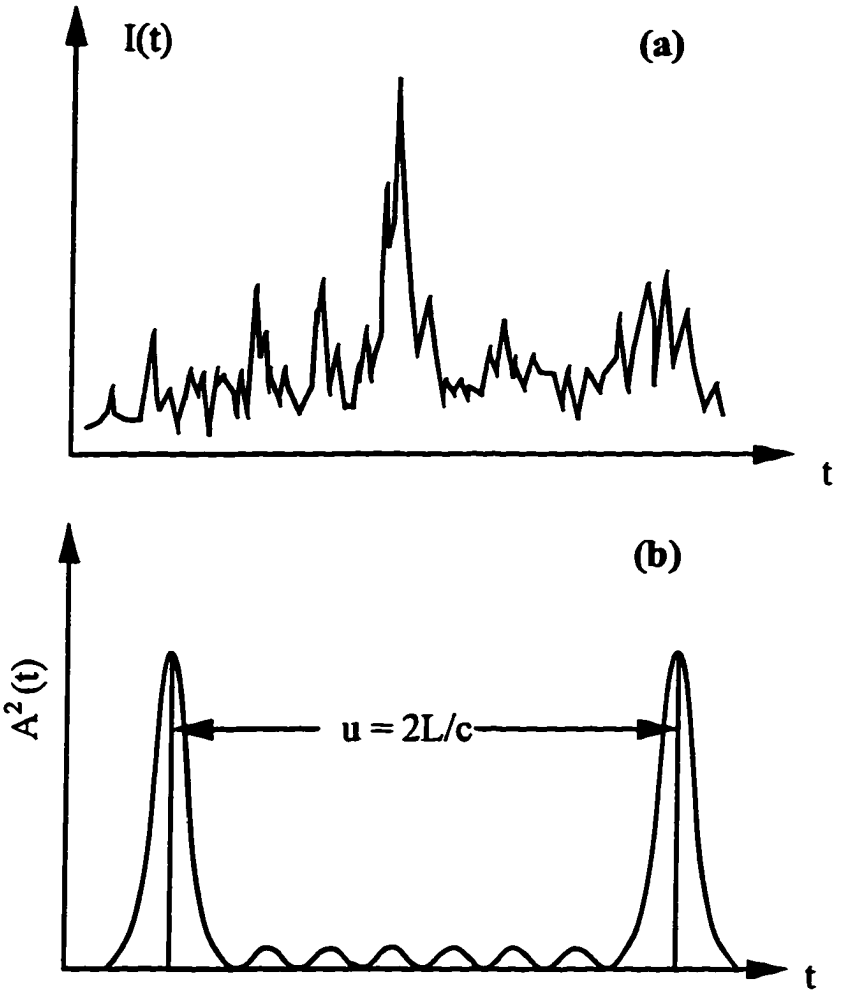


Fig. 2.2 (a) Laser intensity when mode phases are random.
(b) Laser intensity when mode phases are locked.

If, however, one succeeds in producing by a suitable mechanism steady relations among the phases of the various modes, then the laser is designated as modelocked and the coherent summation of frequency components is called modelocking. Modelocking[2-3] is the basic principle of generation of ultrashort pulses, and it is possible to generate laser pulses with duration on the femtosecond time scale. Modelocking can be achieved through a modulation of the loss (or gain) or internal phase of the laser at a frequency $f = c/2L$, where $L$ is the length of the cavity. A qualitative description of modelocked lasers is given by the following consideration. Assume that all modes possess approximately the same amplitude $E_0$ and between their phases, the relationship

$$\varphi_n - \varphi_{n-1} = \alpha = const \tag{2.3}$$

is fulfilled. Then the total field can be obtained analytically

$$E(t) = \hat{E}_0 \frac{\sin[\frac{N}{2}(\omega t + \alpha)]}{\sin[\frac{\omega t + \alpha}{2}]} e^{i(\omega_0 t + \varphi_0)} + C.C. \tag{2.4}$$

Due to the locking of phases, the modes in the resonator interfere so that the laser emits radiation in the form of short light pulses as depicted in figure 2.2b. The peaks of the pulses appear at those moments in which the denominator in equation (2.4) vanishes, i.e., when $(\omega t + \alpha)/2\pi = q$ holds, where $q$ is an integer. The concept of modelocking is to be understood such that, at these times $t_q$, every mode provides a maximum contribution to the total field strength. Thus the time interval $T$ between two neighboring pulse peaks is $T = 2L/c = 2\pi/\omega$. This is the time that is necessary for a complete round trip in the resonator. Therefore modelocking causes the oscillation energy of the laser to be

condensed into an optical pulse that travels back and forth between the mirrors of the resonator. The pulse duration, defined as the time from the peak to the first zero, is

$$\tau = \frac{T}{N} = \frac{2\pi}{N\omega} = \frac{2\pi}{\Delta\omega}, \tag{2.5}$$

where $\Delta\omega$ is the frequency interval in which laser modes are excited. In the above equation (2.5) the number of oscillating modes is estimated by $N \cong \Delta\omega / \omega$ - that is the ratio of the transition linewidth to the frequency spacing $\omega$ between modes. In general cases, between $\tau$ and $\Delta\nu$ the relation

$$\Delta\nu \cdot \tau \geq C_B \tag{2.6}$$

can be given, where $C_B$ is a number factor of the order one, whose precise value is determined by the temporal shape of the pulse under consideration. For a band limited (or transform limited) pulse the equality holds. Considering a Gaussian profile for the mode amplitude, for instance, on can obtain the uncertainty relation

$$\Delta\nu \cdot \tau \geq 0.441 \tag{2.7}$$

If the lasing linewidth is 10 nm at 620 nm, the pulse width $\tau$ is about 56.5 fs, which is called a transform limited pulse width. Thus the minimum temporal duration of the modelocked pulses is inversely proportional to the gain linewidth of the lasing medium. The more modes which are modelocked, the shorter the pulse. The vibration- and rotation-broadened electronic energy levels in organic dyes result in a broad spectral linewidth $\Delta\omega$, with the gain over a wide range of frequencies[4-6]. Therefore, a large range of frequency components can be coherently summed to produce short, tunable pulses, and picosecond or femtosecond laser pulses can thus be obtained. The pulses of modelocked lasers are distinguished not only by ultrafast pulse duration but also high peak intensities.

The maximum intensity is proportional to $N^2\left|\hat{E}_0\right|^2$, whereas for the case of non-modelocked laser the expectation value for the peak intensity is proportional to $N\left|\hat{E}_0\right|^2$. Thus, given in both cases the same number of modes, $N$, the peak intensity in the case of modelocking is larger by the factor $N$ than the expectation value of the intensity under generation of laser radiation with stochastic relations between the phases of the individual modes.

### 2.1.2 Colliding pulse modelocking (CPM) dye laser

The CPM dye laser oscillator is the basis of the ultrafast laser system used in this thesis research. It uses passive modelocking [1,5,7]. The saturable absorber dye inserted in the cavity modulates the loss of light in the cavity and acts in concert with the gain medium to produce subpicosecond pulses. The ring cavity CPM laser is optically pumped by Spectra-Physics® Model 171 argon laser with 2-3 watts cw power at 514.5 nm wavelength. The CPM laser oscillator consists of 7 mirrors, 2 jet streams and four prisms as shown in figure 2.3. Three mirrors (including the output coupler) are flat and used to close the ring. The other four cavity mirrors, two with 10 cm radius for the laser medium Rh6G and two with 5 cm radius for the saturable absorber DODCI, are used to focus the beam at the dye jet streams. The dye gain medium Rhodamine 6G is at a concentration of about $1.5 \times 1.0^{-3}$ molar in a jet stream of ethylene glycol produced by a 300 μm nozzle. The saturable absorber dye DODCI flowing in a second jet stream through a 100 μm nozzle is at $10^{-4}$ molar concentration in an ethylene glycol solution. The laser mode is

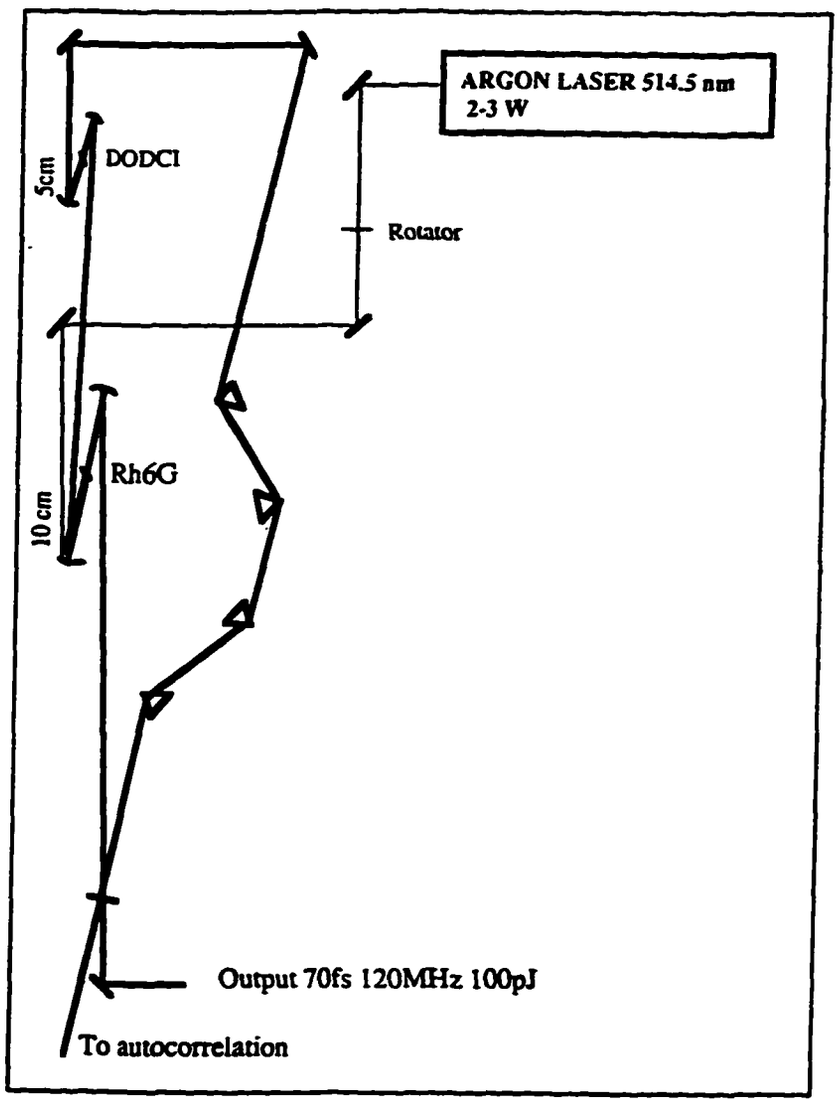


**Fig. 2.3 Schematic diagram of CPM laser cavity.**

focused more tightly in the absorber stream than in the gain stream to enhance the non-linearity of the saturable absorber for better stability.

In colliding pulse modelocking, the two counterpropagating pulses in the ring resonator are synchronized to precisely overlap in the saturable absorber[5,7]. This is controlled by the system itself due to the sharp reduction of intracavity loss for that condition, and is achieved by separating the absorber and gain media by a quarter of the cavity round trip length, as indicated in figure 2.4. Interference of the two overlapping pulses creates a transient standing wave pattern in the saturable absorber. It reduces the energy required to saturate the absorber[3,7-8] and thus reduces the intracavity loss. These two pulses saturate the absorber while only one saturates the gain at a given time, which increase the stability of the mode-locked laser[2,7-9]. The quarter cavity length between the gain and absorber media ensures that clockwise and counterclockwise circulating pulses are equally amplified through the gain medium. Such an arrangement reduces the formation of additional pulses in the cavity, since the continuously pumped gain dye has the same period of time to recover following each pulse. The ring cavity also eliminates the need to precisely position the saturable absorber stream as required in the linear geometry.

Besides the bandwidth of the gain and absorber media, the group velocity dispersion (GVD) in the optical cavity[5-7], which would increase the temporal duration of the pulse, is the fundamental constraint of a CPM laser. The 19 1/4-wave layer dielectric coated mirrors minimizes the intracavity group velocity dispersion, while the 4 quartz prisms compensate the group velocity dispersion caused by self-phase modulation (SPM)[10-11] in the absorber jet. The negative dispersion provided by the prism set can be

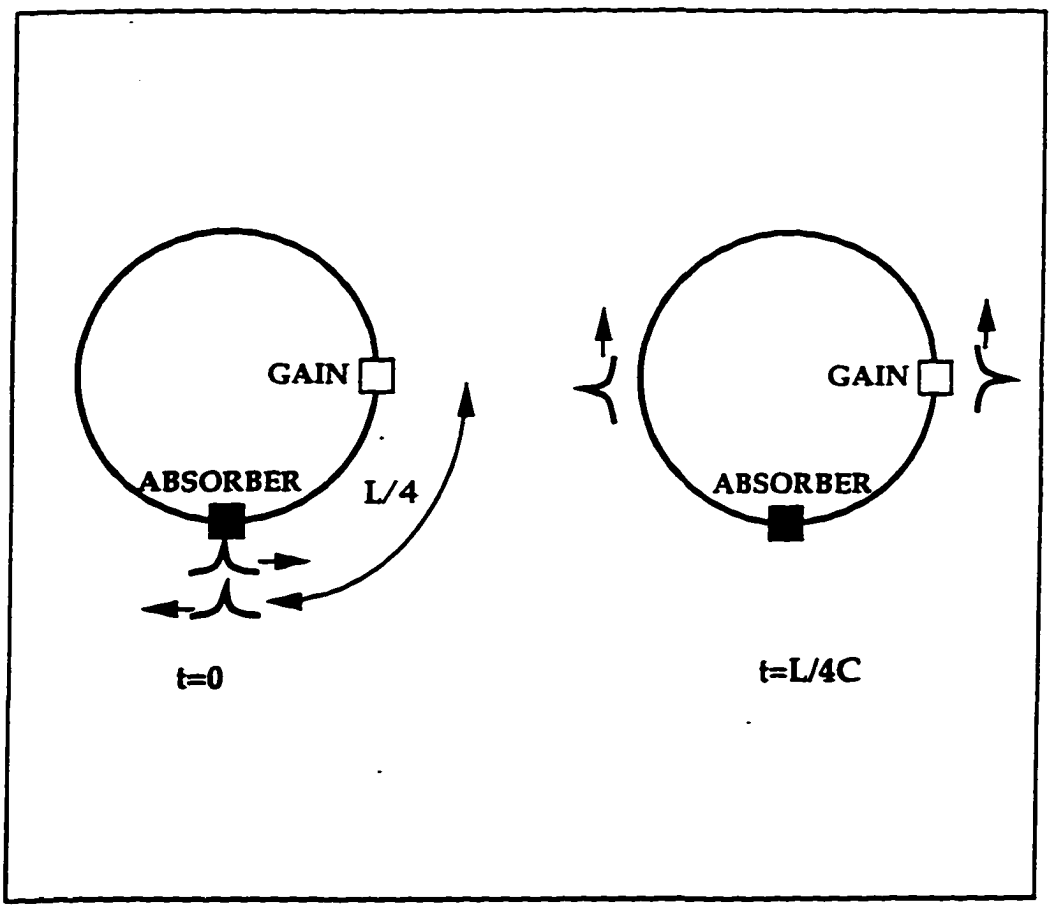


Fig. 2.4 Schematic diagram of a CPM laser. The spacing between the gain medium and the absorber is a quarter of the circumference of the cavity.

adjusted continuously by moving a prism along a normal to the prism base to optimize the compensation. With the prism set, the output pulse width is improved from 100 fs to 56 fs which is close to the transform limit of the 12 nm laser bandwidth. Optical pulses generated by the CPM oscillator have a central wavelength of 620 nm, a FWHM bandwidth of about 12 nm, energy of 80 pJ per pulse and a repetition rate of 120 MHz. Figure 2.5 shows a typical autocorrelation trace from CPM laser measured by its SHG at 310 nm, in which the 100 fs FWHM of the autocorrelation signal yields a pulse width of 65 fs assuming a $sech^2$ pulse shape.

### 2.1.3 Amplification of CPM pulse

Optically pumped organic dyes can be used to amplify the femtosecond laser pulse to several gigawatts while retaining the short duration of the incident pulse by pulse compression[11]. The ultrafast laser pulse from a CPM laser oscillator is amplified for various spectroscopic applications by a four stage dye amplifier as depicted in figure 2.6. The pump laser is a Quanta-Ray DCR-2 Q-switched Nd:YAG laser emitting 1.06 μm light which is doubled to 532 nm. The laser delivers 250 mJ of power in 8 ns pulses at the second harmonic wavelength 532 nm with a 20 Hz repetition rate to excite the four stage dye amplifier. It divides 5%, 10%, 17% and 68% of the power respectively to pump the four stages. The first three stages were pumped transversely and the fourth was pumped longitudinally. The optical length is 3.5 cm for first three stages and 7.5 cm for the fourth stage. The dye in the first stage is Kiton red at $5 \times 10^{-4}$ M concentration. The second, third and fourth stages have Sulforhodamine 640 at concentrations of $6 \times 10^{-5}$ M, $4 \times 10^{-5}$ M

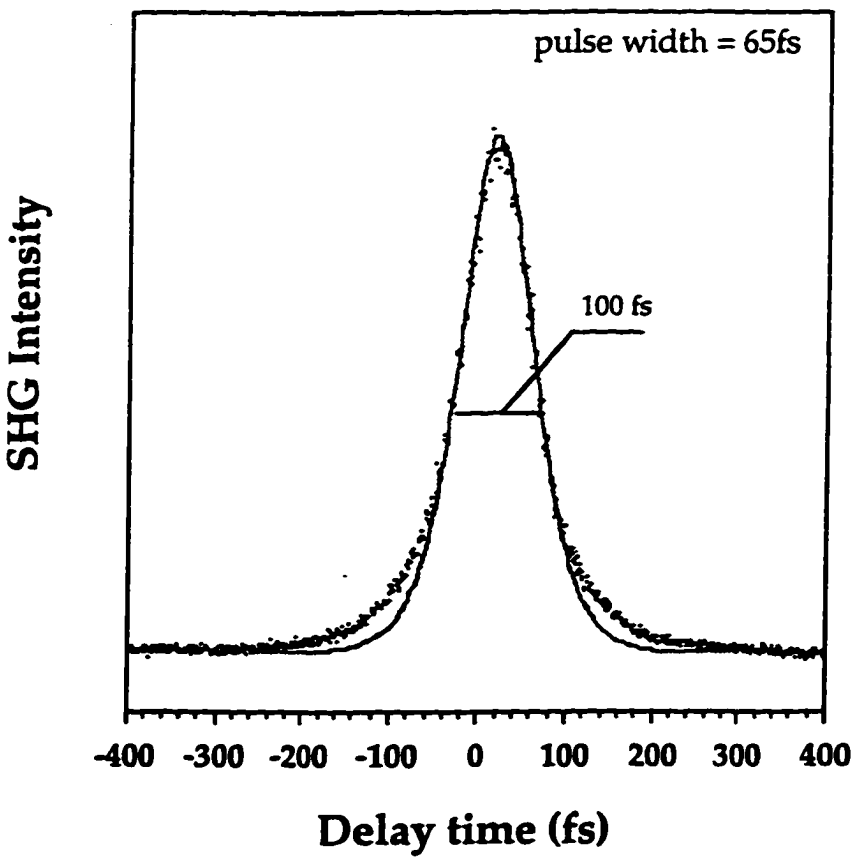


Fig. 2.5 Autocorrelation trace of the CPM laser oscillator obtained by measuring the SHG signal. The pulse width is about 65 fs assuming a $sech^2$ pulse profile.

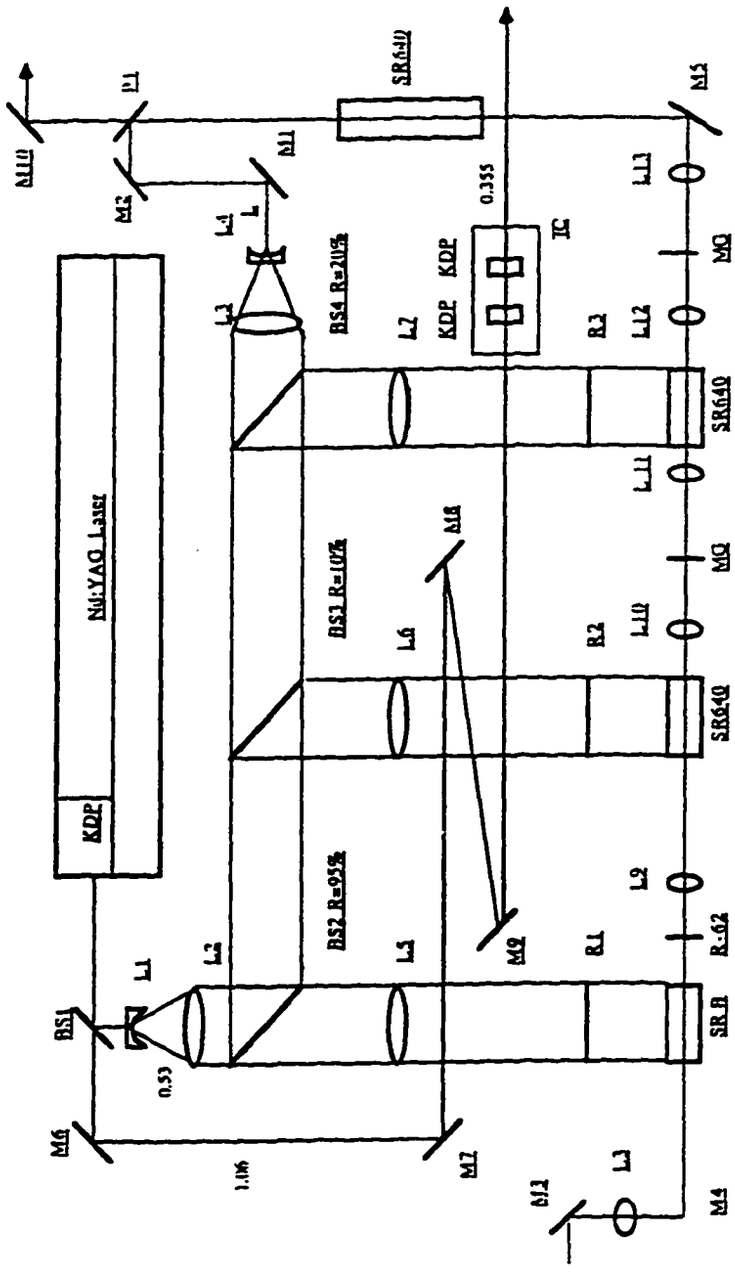


Fig. 2.6 Schematic diagram of the dye laser amplifier system. The frequency doubling of a 20 Hz Nd:YAG laser is used to pump this four stage dye amplifier.

and $1 \times 10^{-5}$ M, respectively. The dye solvent in the first three stages is water and in the fourth stage is methanol. Kiton red has a low absorption at the seed pulse wavelength of 620 nm, which minimizes the absorption loss at the high concentration used in the first stage. The peak net gain of sulforhodamine 640 closely approximates our amplified pulse wavelength 619 nm. Also, sulforhodamine 640 is used to limit distortion due to wavelength dependent gain[5, 11]. A spatial filter (small pin hole) and two thin jets of saturable absorber (Malachite Green in ethylene glycol) were inserted between adjacent stages of the dye amplifier to suppress the amplified spontaneous emission (ASE) and to control preferential amplification of the pulses leading edge[11]. The net amplification gain, including the saturable absorber loss, of the four stages are 200, 150, 30 and 4, respectively, the total gain is about $3 \times 10^6$. Thus, 80 pJ pulses from the CPM laser are amplified to about 0.3 mJ. Amplification of the laser pulse to even higher energy is limited by rapid depletion of gain due to amplified spontaneous emission (ASE) and the short spontaneous emission time of the dyes (~1 ns) in the dye amplifier.

Another problem for the ultrafast pulse amplifier is pulse distortion. The group velocity dispersion (GVD) in the dye solvent and amplifier optics causes significant temporal broadening of the femtosecond pulses. The time delay $\tau_d$ due to group velocity dispersion between two wavelengths with difference $\Delta\lambda$ is

$$\tau_d = \frac{\lambda L}{c}\frac{d^2 n}{d\lambda^2}\Delta\lambda, \qquad (2.8)$$

where L is the medium length, $n$ is the index of refraction, $\lambda$ is the optical wavelength and c is the speed of light. A short pulse corresponds to a broad bandwidth, thus larger group velocity dispersion. In the four stage dye amplifier here, the pulse from the CPM laser is

broadened from 65 fs to 500 fs due to the group velocity dispersion in the dye solution and optical components. The temporal broadening by group velocity dispersion is mostly a linear frequency sweep and therefore can be compensated by an optical device with negative dispersion. The compensation technique is described in the next section. Nonlinear broadening such as nonlinear frequency generation, wavelength dependent gain, saturable absorption and saturable gain also occur in the dye solvents and can combine with group velocity dispersion to yield irreversible temporal broadening. By selecting pump energy and appropriate dyes in each stage[11], such nonlinear broadening is minimized.

In order to maximize gain and prevent amplification of the two CPM laser pulses, the Nd:YAG laser must fire in synchronization with the CPM laser such that the peak of the Nd:YAG pulse excites the amplifier dye cells just as a CPM laser pulse is incident on the cells. This is accomplished by a gated low jitter pulse generator which is shown in the block diagram in figure 2.7. Part of the CPM pulse train is detected by a Enercomp fast photodiode and amplified by a Comlinear Model CLC100 wide band amplifier. The 120 MHz output from the Comlinear amplifier is directed to the trigger input of the Precision Instruments Model 351 clock synchronizer. The 20 Hz Q-switch output of the Nd:YAG is attenuated and directed to an Avtech AVK pulse generator, the output of which is then directed to the gate input of the clock synchronizer. A Q-switch pulse activates the clock synchronizer to generate a synchronized trigger to the Nd:YAG high speed driver which fires the Pockel's cell. A variable delay line of 0.25 ns resolution is adjusted for temporal overlap of the dye and Nd:YAG laser pulses and is set to maximize the four stage dye amplifier gain.

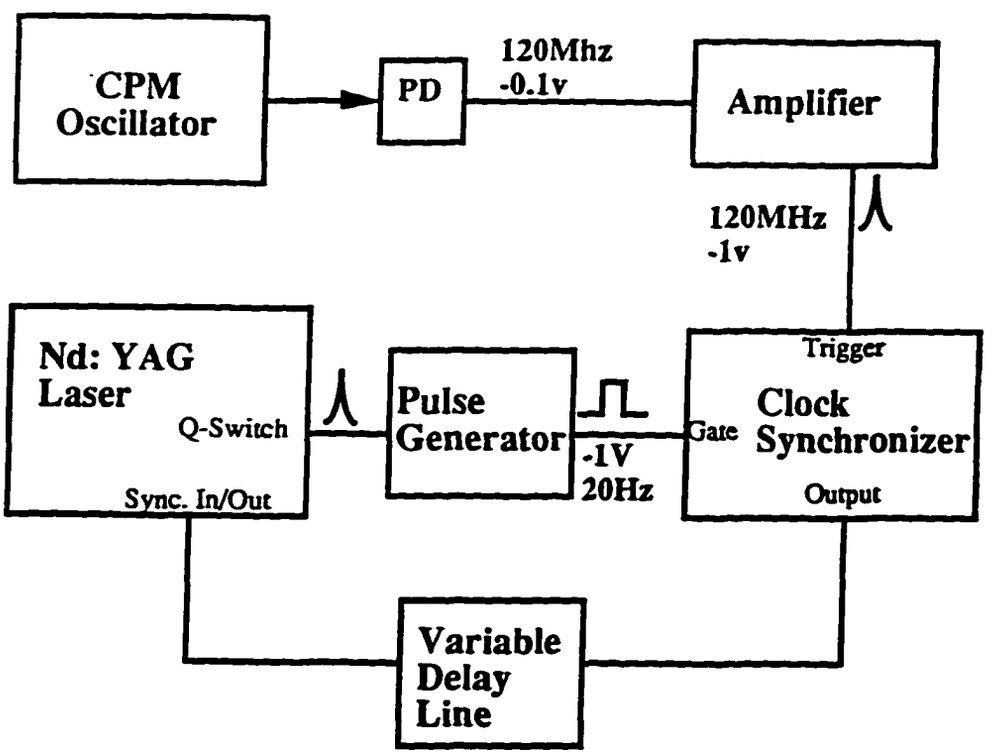


Fig. 2.7 Synchronization between the CPM laser and the Nd:YAG laser.

### 2.1.4 Pulse compression

The prism pulse compressor, consisting of a pair of SF10 glass Brewster angle (60° for 620 nm) prisms with double pass geometry (figure 2.8), is employed after the CPM amplifier to reduce the pulse duration. The amplified CPM pulse is much broader in temporal width than the pulse from the oscillator. This is mainly due to the positive GVD (linear chirp) after passing through a large amount of dispersive material such as dye solution and optical glass. In the positively chirped pulse, the frequency increases in time from the leading to the trailing edge of the pulse, i.e. the pulse is red in front and blue in rear. The pulse phase shift depends on the frequency and can be developed in a power series of $(\omega-\omega_0)$[2, 12-13]

$$\Phi(\omega)=\Phi(\omega_0)+(\omega-\omega_0)\Phi'(\omega_0)+\tfrac{1}{2}(\omega-\omega_0)^2\Phi''(\omega_0), \qquad (2.9)$$

where $\Phi'(\omega_0)=(d\Phi/d\omega)_L$, $\Phi''(\omega_0)=(d^2\Phi/d\omega^2)_L$ and L is the length of the medium. The group velocity dispersion $\Phi''$ increases the output pulse width $\tau_{out}$[2, 13] for Gaussian beam propagation

$$\tau_{out}=\tau_0[1+(4\ln 2\Phi''/\tau_0^2)^2]^{1/2} \qquad (2.10)$$

where $\tau_0$ is the chirp free pulse width or the transform limited pulse width. The GVD introduced by a length L of a transparent medium is:

$$\Phi''_M=(\lambda_0^3/2\pi c^2)n_0''L \qquad (2.11)$$

where $\lambda_0$ is the central wavelength and $n_0''=(d^2n/d\lambda^2)_{\lambda_0}$. The GVD $\Phi''_M$ for the four stage amplifier is shown in Table 2.1.

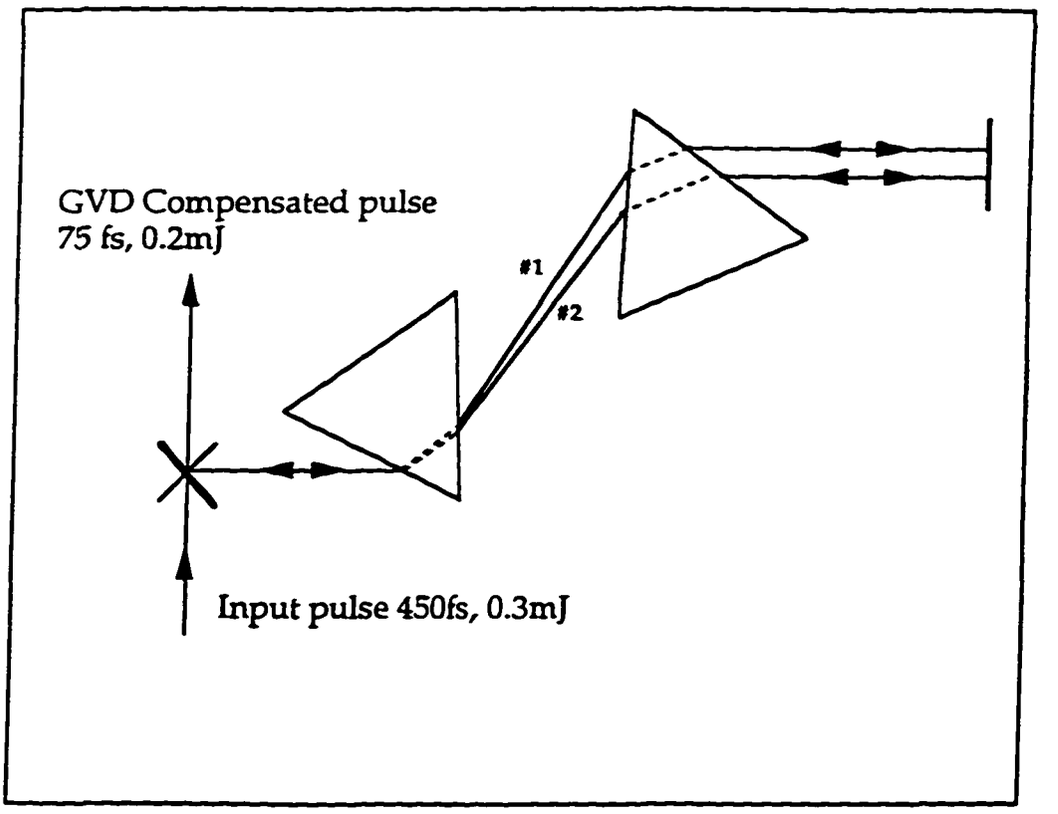


Fig. 2.8 Pulse compression using a prism set as a negative GVD device. Two prisms with double paths are used instead of four prisms.

Table 2.1 The amount of GVD introduced by the four stage amplifier.

| Type | Formula | L(mm) | $\Phi''$ ($fs^2$) |
|---|---|---|---|
| Lens (BK7) | 70.141 | 56.6 ± 4.0 | 3944 ± 280 |
| Water | 54.921 | 225 ± 10 | 12357 ± 550 |
| Glass ($SiO_2$) | 51.191 | 16 ± 3 | 820 ± 154 |

For all elements in the four stage amplifier, the total amount of GVD $\Phi''_M$ is about $1.5\times10^4$ fs$^2$. For the CPM oscillator pulse width $\tau_0$=70 fs, using equation (2.10) we calculated $\tau_{out}$=580 fs which agrees with the amplified pulse width. Therefore, the temporal broadening is mainly introduced by GVD, which significantly affects the short pulse generation, amplification and propagation.

The positive linear chirp, $\Phi''_M$, can be compensated by negative group-velocity dispersion devices such as a prism and grating set[12-15]. The dispersion by the prism pair compressor[12] is:

$$\Phi'_P = \frac{4\lambda^3}{\pi c^2}\{-Sn^2 + \frac{L}{\sqrt{3}}[\frac{nn'}{1+n^2} + n^2(1-\frac{1}{n^2(1+n^2)})]\} \qquad (2.12)$$

where $n$ is the refraction index of SF10 glass, and $L$ is the total pathlength in the prisms. The first term of $\Phi'_P$ proportional to S provides negative GVD. The second term depending on the amount of pathlength in the prism glass (L) contributes positive dispersion. Note, the dispersion of a high index prism is five times that of regular glass. By adjusting the dispersion $\Phi'_P$ of the prism set, the positive dispersion $\Phi'_M$ introduced by the amplifier can be compensated, $\Phi'_{total} = \Phi'_P + \Phi'_M \geq 0$. The 450 fs amplified CPM pulses is compressed to 110 fs by the prism compressor. The autocorrelation of the amplified CPM pulses is measured by their SHG at 310 nm as plotted in Figure 2.9. To compensate the dispersion to the transform limited pulse width, higher order dispersion must be considered, and the combination of a set of prisms and gratings[14] has been demonstrated.

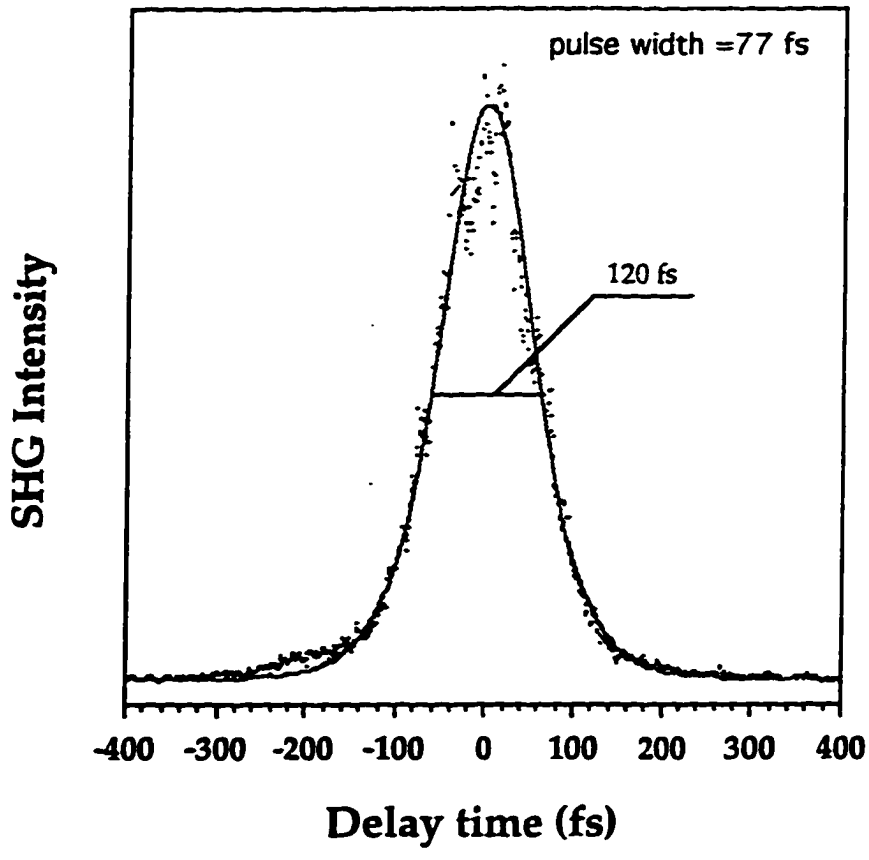


Fig. 2.9 Autocorrelation trace of an amplified CPM laser pulse (dispersion compensated) obtained by measuring the SHG signal. The pulse width is about 77 fs assuming a $sech^2$ pulse profile. The solid line is the $sech^2$ $(t/\tau)$ fitting where $\tau = 70$ fs.

### 2.1.5 Supercontinuum generation and amplification

A CPM pulse after the four stage dye amplifier and prism compressor becomes ~100 fs with ~0.3 mJ. However, the wavelength is limited around 620 nm because of the gain bandwidth of the dye medium. For most spectroscopic experiments, a tunable pump wavelength and a "white" probe pulse is desired. Alfano and Shapiro[16] discovered that when a short pulse is focused into a transparent medium a white light continuum is generated (supercontinuum) and the short pulse width is maintained. The phenomenon is due to self phase modulation (SPM): An intense short pulse distorts the electronic distribution in a medium and induces a refractive index change. The phase of the light in the medium is[10]:

$$\Phi = \omega t + (n_0 + n_2 E^2(t))\frac{z\omega}{c}. \qquad (2.13)$$

This intensity dependence modulates the instantaneous phase of the pulse. The phase modulation leads to a frequency modulation

$$\Delta\omega = -\frac{d\Phi}{dt} = -\frac{n_2 z\omega}{c}\frac{dE^2(t)}{dt}. \qquad (2.14)$$

Both redder and bluer frequencies than the input frequency are generated. The redder components (lower in frequency, $\Delta\omega<0$) arise from the leading edge of the incident pulse ($\frac{dE^2(t)}{dt} > 0$) and bluer components from the trailing edge. Frequency shifts are of the order $\Delta\omega_{MAX} \cong \frac{\omega n_2 Iz}{c\tau}$, and $\Delta\omega_{MAX}$ is inversely proportional to the laser pulse width, $\tau$. In this thesis work, the amplified 100 fs pulse is focused by a 6 cm focal lens into a 1 mm ethylene glycol jet stream or a 1 cm methanol cell to generate a supercontinuum (400 nm-

1200 nm), which is collected by a 4 cm focal lens and collimated into a ~6 mm spot size beam for different measurement purposes. The conversion efficiency of the continuum is very high, approximately, a 50 nJ pulse at 500 nm with a 10 nm band width is generated by about a 100 μJ pulse at 620 nm. The supercontinuum pulse is also highly chirped since the SPM and GVD bring the redder components to the leading edge of the pulse. The GVD is large due to the broad bandwidth. A prism set can be used to compensate for the dispersion and make "chirp free" white light within a limited wavelength range[17].

To generate a tunable wavelength pump, the white-light continuum is passed through a 10 nm interference filter to select the specific wavelength experimentally required, which is further amplified by a single stage dye amplifier. In vision experiments, pulses at 500 nm are amplified to a few microjoules in a 1 cm cell flowing Coumarin 500 dye at a concentration of $5x10^{-4}$ molar in methanol solution. The dye cell is pumped transversely by the third harmonic from the 20 Hz Nd:YAG laser at 353 nm, with 8 ns width and ~10 mJ energy per pulse. The gain in this single stage amplifier is about 200. Other dyes such as LDS 698 were used in hole burning experiments to amplify 680 nm pulses to the same order of energy by the second harmonic from the Nd:YAG laser at 530 nm.

## 2.2) Intensity Correlation Measurements

Intensity interferometric correlation techniques have been widely used to measure ultrashort laser pulse duration[18-19]. In an autocorrelation measurement of a CPM pulse duration (figure 2.10), the 620 nm beam is split into two equal intensity beams. They are

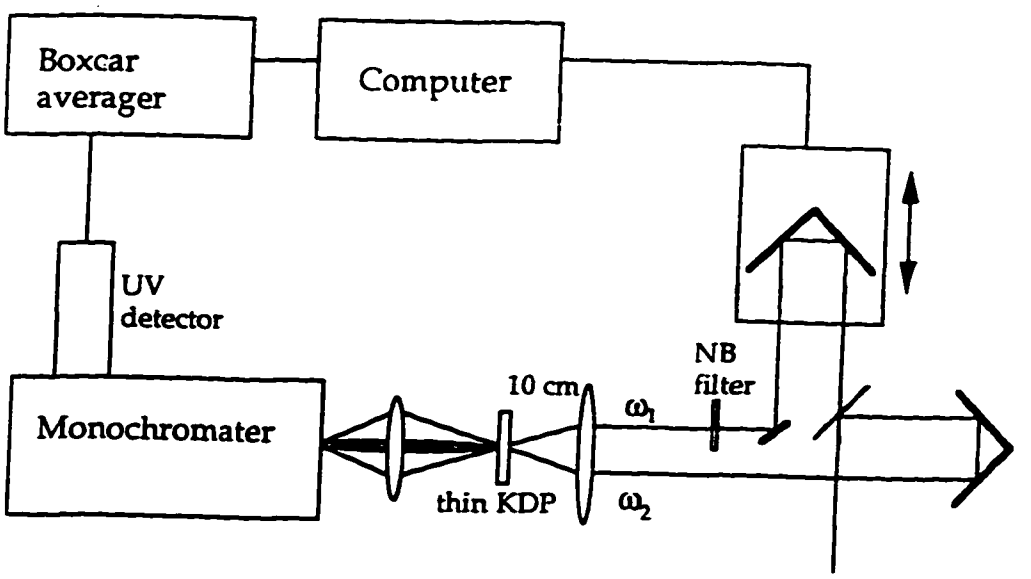


Fig. 2.10 **Pulse duration measurement using correlation method. If $\omega_1 = \omega_2$, the SHG obtained from KDP is called autocorrelation. If $\omega_1 \neq \omega_2$, the sum frequency generated $\omega_s = \omega_1 + \omega_2$ is the cross correlation.**

focused into a 100 μm KDP nonlinear crystal at the phase matching angle to generate a second harmonic at 310 nm, which is detected by a uv sensitive photomultiplier. Since the uv signal in the phase matched direction for absorbing a photon in each beam can only be detected during temporal overlap, the second harmonic signal obtained by varying the delay of one pulse to the other is the pulse autocorrelation. By deconvolution, one can obtain the pulse duration. Assuming a squared hyperbolic secant ($sech^2$) pulse profile, for example, the pulse width is the autocorrelation trace divided by 1.55. If the two pulses have different wavelengths, the sum frequency is generated in the nonlinear crystal and the signal measured at the sum frequency is the cross-correlation. By measuring the zero time of cross-correlation of a fixed frequency with the whole supercontinuum wavelength the dispersion of the continuum light is obtained (figure 2.11).

## 2.3) Amplitude Interferometric Measurements

Besides intensity correlation, the amplitude correlation technique is also used in this thesis. The amplitude correlation gives the coherent length. Since the phase information gets lost, the temporal evolution of field strength $E(t)$, and in particular the parameters such as the pulse duration can not be calculated unambiguously. Determination of the pulse duration from the spectral bandwidth is only possible when we already know that the light pulse is bandwidth limited, or Fourier-limited. In this case the phase of the field strength does not change during the pulse, accordingly, the spectral width is only determined by the profile of the amplitude.

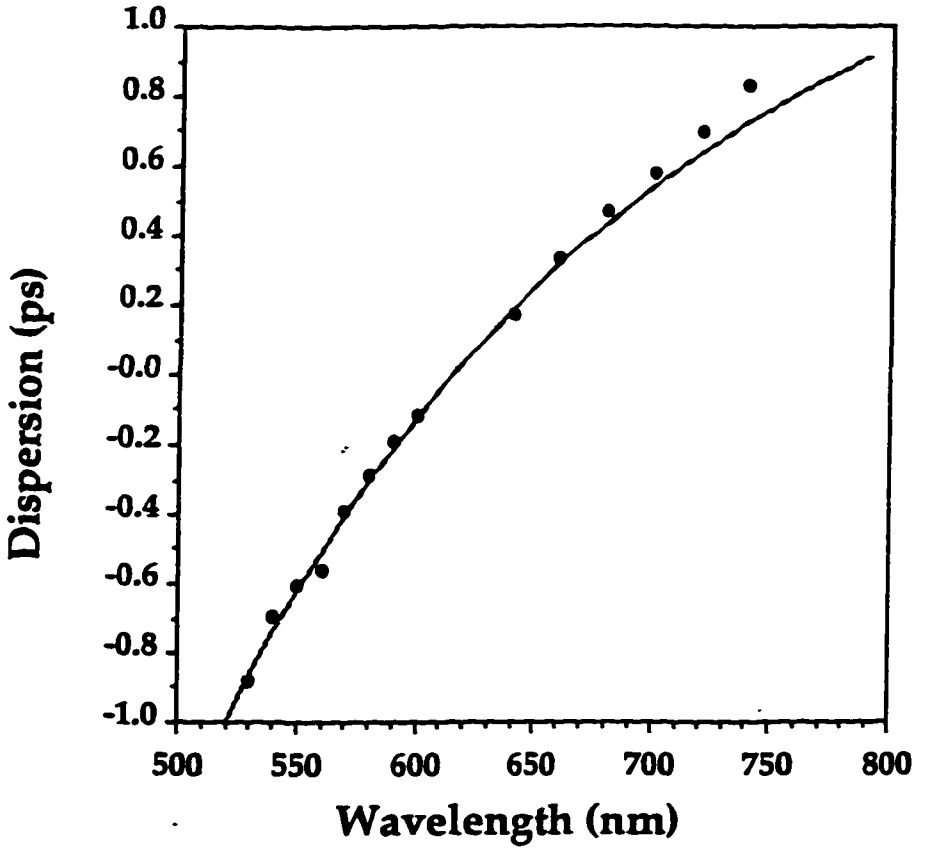


Fig. 2.11 The dispersion curve of continuum light generated by 1 mm ethylene glycol and measured by the zero time of the cross-correlation signal. The solid fitting is the calculation of GVD in 2.4 cm BK7 glass.

Most recently, time-of-flight ultrafast packet detection was demonstrated[20]. The interferometric first-order cross correlation between a reference pulse and a signal pulse occurs directly on the linear detector array, leading to large background noise and a small range of the time window. The novel time-resolved femtosecond amplitude interferometric correlation technique developed here is for the purpose of optical storage and fast information retrieval on the OEP/PS. However, this new method also allows for the conversion of temporal information to spatial information with femtosecond resolution and can be used for scientific, biological and medical research in wavefront registration. The interferometer is described by the following example. It is for the first time, to our knowledge, that the temporal development of the diffraction of light waves from objects by femtosecond correlation interferometry was demonstrated. This technique converts the time development of diffracted wave fronts into motion of a two-dimensional interference pattern of equal phase contours, which is registered on a two-dimensional CCD.

The time development of light pulse diffraction off a half-plane edge is shown in Fig. 2.12. At time $t_0$ the pulse has not arrived at the screen. At time $t_1$ the pulse has undergone diffraction, and at $t_2$ light diffraction has further developed. The basic principle for cross-correlation interferometry to detect the diffracted wave (say at time $t_2$) is shown in Fig. 2.13. A reference ultrashort pulse (R) and a signal diffracted pulse (S) incident at a well-defined angle $\pm\alpha$ to the normal to the diffraction grating are combined on the grating. The positive and negative first diffraction orders from the respective beams propagate along the normal to the grating ($p \sin \alpha = \lambda$, where $p$ is the spacing between

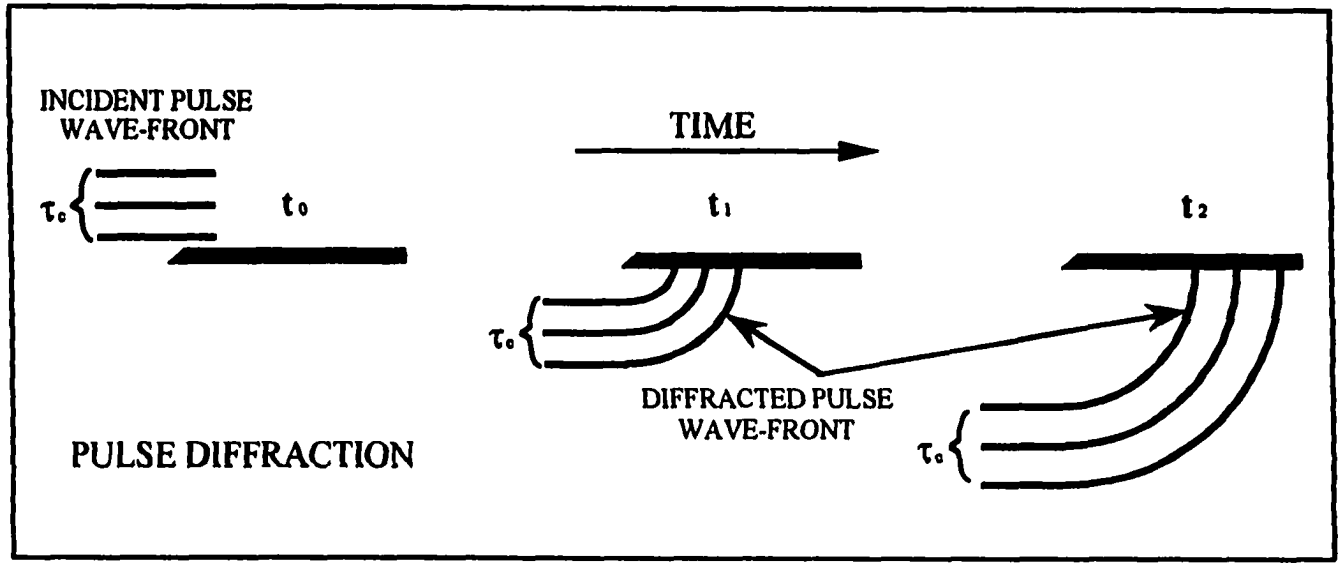


Fig. 2.12 Diagram showing what is to be expected when an ultrashort pulse is diffracted by a half-plane. Contours of equal phase before ($t_0$) and after ($t_1$ and $t_2$) the diffraction are shown. $\tau_c$ is the correlation time.

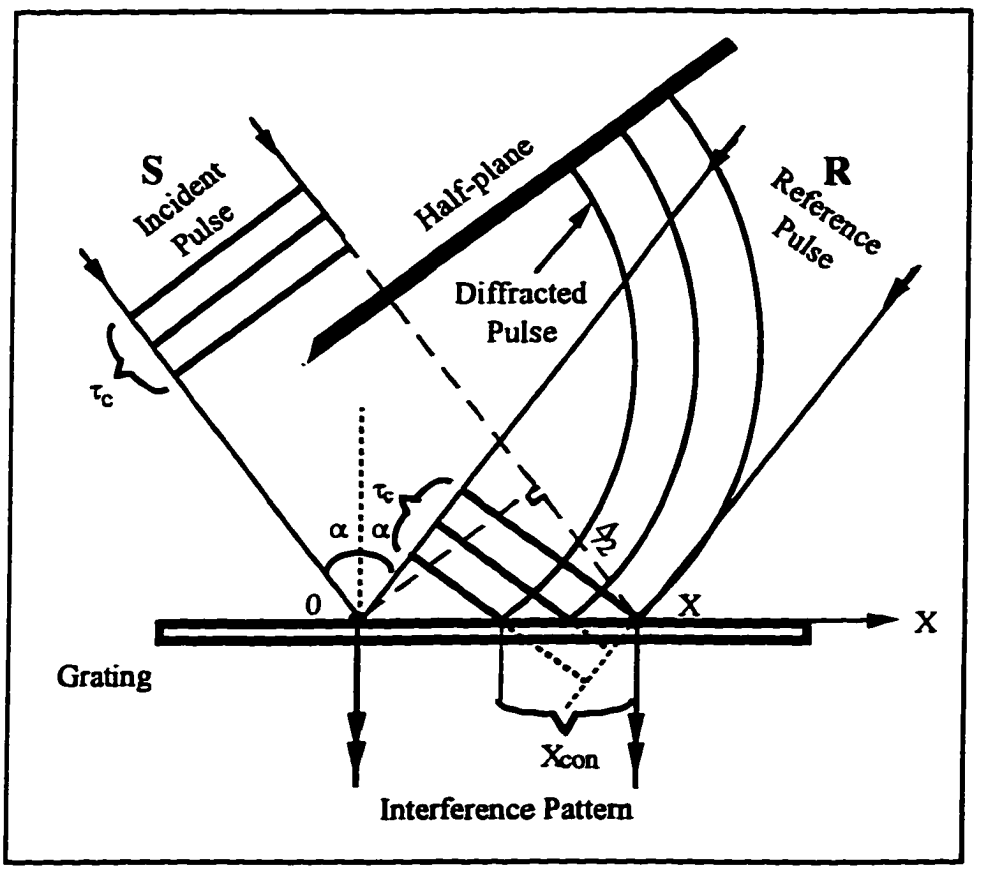


Fig. 2.13 Principle of detecting the diffracted wave front by a cross-correlation interferometer.

grooves). The interference fringes are tuned in the direction of the grating dispersion ( $x$ axis). One of the beams is oriented at a slightly different angle to the plane of incidence to produce the desired fringe pattern in the vertical ($y$ axis) direction[21]. This method gives us the possibility of observing in the $y$ direction several planar cross sections of the diffracted wave fronts. The grating plane is optically conjugated with a CCD detector, which records the interference image.

The diffraction grating introduces a continuous optical time delay along a given interference fringe. The difference in the optical path is

$$\Delta = c\tau = 2x\sin\alpha = 2\lambda x / p \qquad (2.15)$$

where $\lambda$ is the wavelength, $x$ is the linear coordinate, and $\tau$ is the time delay between the reference and signal pulses. The time-delay window is given by $\tau_d = 2\lambda D/cp \cos\alpha$, where $D$ is the diameter of the beams.

Consider $E_{dif}(t)$ and $E_r(t)$, the electric fields for the diffracted and reference pulses, traveling in the two arms of the cross correlator. The intensity distribution recorded by the CCD detector is proportional to the function

$$I(\tau) \sim \int |E_r(t)\exp(i\,2\pi y/d) + E_{dif}(t-\tau)|^2\,dt$$

$$= \int |E_r(t)|^2\,dt + \int |E_{dif}(t)|^2\,dt + 2\mathrm{Re}[g(\tau)\exp(i\,2\pi y/d)], \qquad (2.16)$$

where $d$ is the fringe period along the $y$ axis ($d = \lambda/\sin\beta$). The first-order cross-correlation function is

$$g(\tau) = \int E_{dif}^{*}(t-\tau)\,E_r(t)\,dt. \qquad (2.17)$$

When the duration of the reference pulse is short, $E_r(t) = E_{0r}(t)\delta(t)$ and $E_{dif}(t) = |E_{dif}(t)| \exp[i\phi_{dif}(t)]$, where $\phi_{dif}(t)$ is the phase distribution of the diffracted wave, then relation (2.16) can be expressed as

$$I(\tau) \sim 1 + B|E_{dif}(\tau)| \cos[2\pi y/d - \phi_{dif}(\tau)], \qquad (2.18)$$

where

$$B = 2 \Big/ \Big[ \int |E_r(t)|^2 \, dt + \int |E_{dif}(t)|^2 \, dt \Big].$$

The minima of intensity [relation (2.18)] are given by

$$|2\pi y/d - \phi_{dif}(\tau)| = (2m + 1)\pi/2, \quad m = 0, 1, 2 .... \qquad (2.19)$$

The maxima of intensity are given by

$$|2\pi y/d - \phi_{dif}(\tau)| = 2m\pi \qquad (2.20)$$

The observed shape of the cross-correlation interference fringes is directly determined by the phase distribution of the diffracted wave. The fringes represent contours of equal phase. The fringe visibility function is

$$K(\tau) = B|E_{dif}(\tau)|, \qquad (2.21)$$

which gives information about the amplitude of the diffracted wave.

In the space domain ($x$ direction) the size of high-visibility interference fringes, $x_{con}$, will depend on the pulse correlation time $\tau_c$ and is given by $x_{con} = pc\tau_c / \lambda$. For our measurement, $\tau_c = 100$ fs, $p = 0.01$ mm and $\lambda = 620$ nm. This gives $x_{con} = 0.6$ mm and the time-delay window $\tau_d = 2.3$ ps.

A schematic diagram of the experimental arrangement is shown in Fig. 2.14. The optical pulses are generated by the CPM laser. The grating is a transmission type with

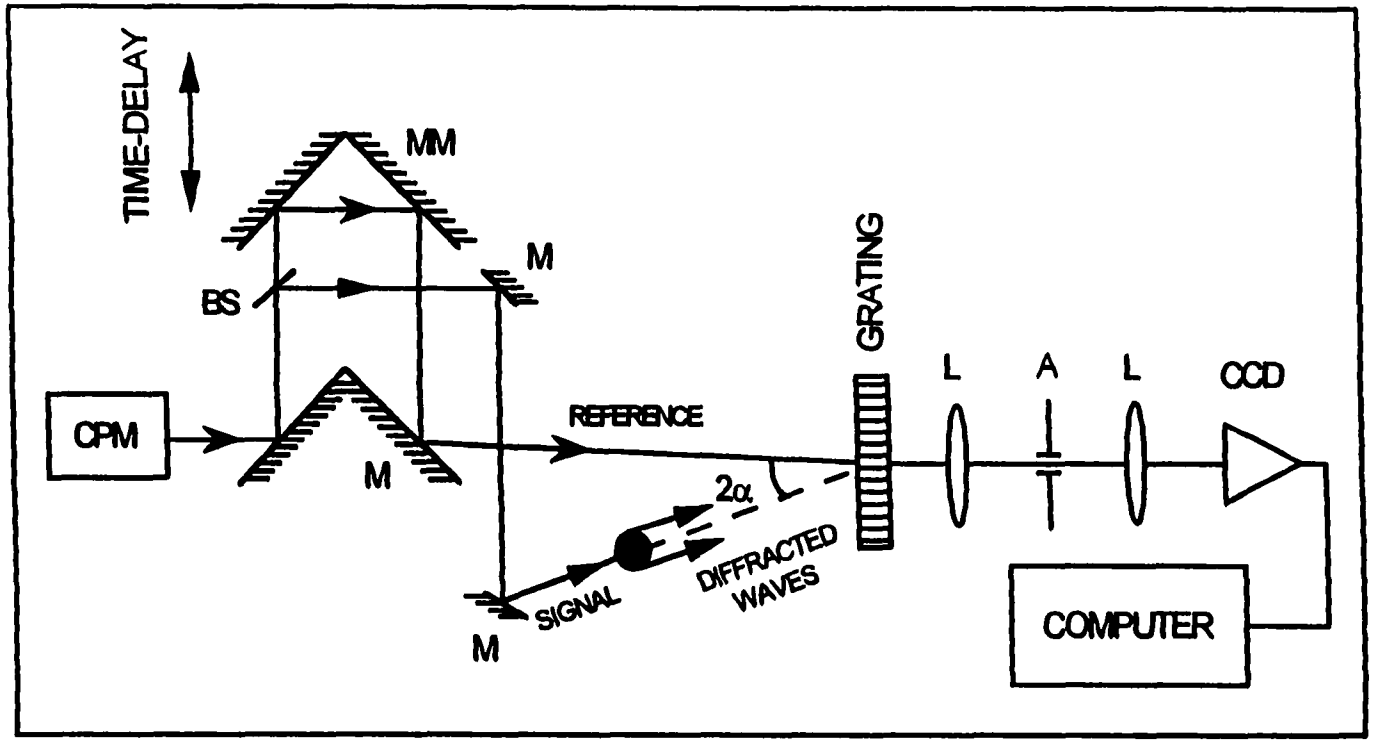


**Fig. 2.14 Experimental arrangement for real-time observation of diffracted light waves: M's , mirrors; MM, movable mirror; BS, beam splitter; A, aperture; L's, lenses (focal length f = 6 cm). The grating, lenses, aperture, and CCD are separated by f.**

100 lines/mm. The CCD detector records the two-dimensional image of interference fringes. When the optical delay between the reference and signal pulses is changed, the high-contrast interference fringes of the zero difference in optical path will move in the continuous optical delay direction in the grating. One can use the light of an ultrashort pulse duration to study in time the shape of the diffracted wave fronts by recording cross-correlation interference. By moving corner mirror MM (Fig. 2.14) continuously, we can study the wave-front propagation as a time motion of the interference pattern. This type of cross-correlation interferometry could be compared with time-gated observation in which the gating effect is caused by the fact that only wave fronts with time delays less than the pulse correlation time will interfere with one another to produce the interference image.

Examples of wave-front propagation in time from diffraction by a metallic half-plane and a rod are shown in Figs. 2.15 and 2.16, respectively. The pattern of Fig. 2.15(a) was made at time $t_0$ (Fig. 2.12) just before the plane-wave front was diffracted by the half-plane. The zero optical delay was in the illuminated region. Figures 2.15(b) and 2.15(c) show the diffracted wave propagation in the half-plane shadow region. The zero optical delay was shifted in the half-plane shadow region approximately 0.6 mm (~ 200 fs time delay between the reference and diffracted beams) and 1.8 mm (~ 600 fs time delay), for figs. (b) and (c) respectively. Pictures taken with a 200 fs time delay [at an early moment $t_1$(Fig. 2.12)] shown in Fig. 2.15(b), and with a 600 fs time delay [at later time $t_2$(Fig. 2.12)] shown in Fig. 2.15(c) clearly reflect the cylindrical wave-front propagation from the half-plane edge in the shadow region. The interference fringes in the $y$ direction represent planar cross sections of the diffracted cylindrical wave-front (separated by time

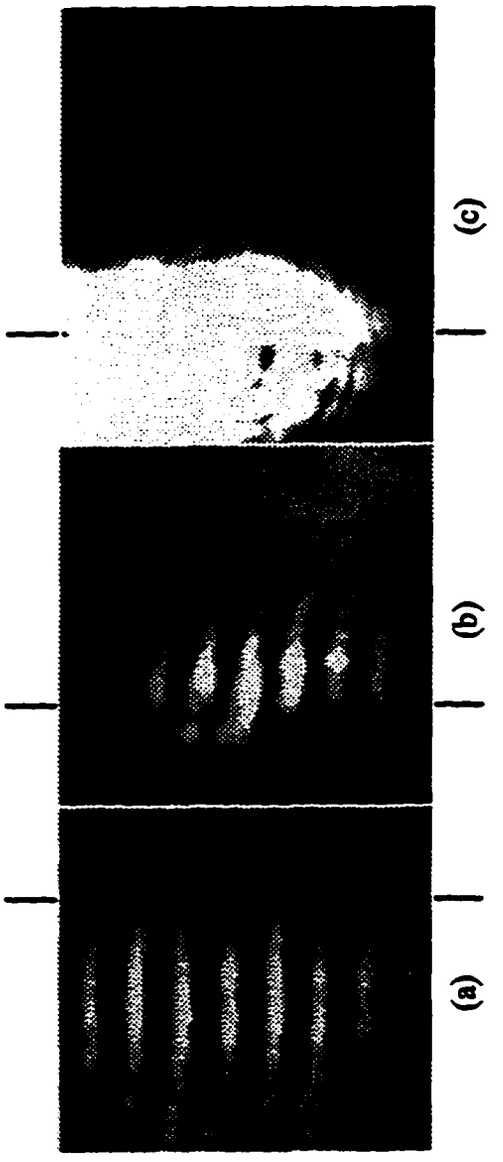


Fig. 2.15 Diffraction from a half metallic plane at different times.

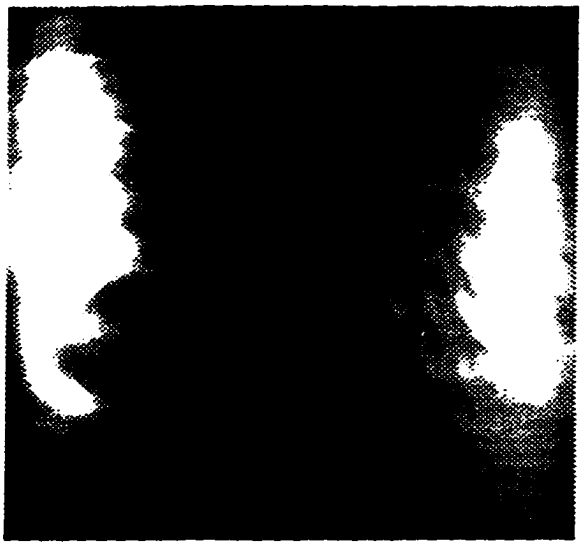

**Fig. 2.16 Diffraction from a metallic rod.**

interval $\lambda/c \sim 2$ fs). The images in Fig. 2.15 show how the diffracted wave front propagates from the half-plane edge in time. The arc becomes longer and its radius of curvature increases with time. The bright region in Fig. 2.15(c) on the left is due to the high intensity of the diffracted wave near the half-plane edge. Figure 2.15(a) was obtained with equal intensities of reference and signal beams.

The CCD recorded image of Fig. 2.16 shows the intersection of two cylindrical wave fronts diffracted by the metallic rod of diameter of 1.2 mm. The bright regions at the right and left rod edges are due to the high intensity of the diffracted wave near the rod edge. The zero difference of the optical path between the reference and the signal wave fronts was in the rod shadow center which combines contours of equal phase from the left and right rod edges. The intersections of these equal phase contours represent the stationary diffraction pattern.

This time-resolved correlation interferometry method with ultrashort pulses and a continuous optical delay allows time-to-space-domain conversion with femtosecond resolution. It is used in this thesis work for the ultrafast detection of photon echo bit information, which is plane wave diffracted from the OEP/PS optical storage material.

## 2.4) 3-beam Accumulated Photon-echo Measurements

Photon echoes refer to the appearance of coherent emission pulses following successive applications of resonant excitation pulses. Their existence depends on the reversibility of dipole dephasing due to inhomogeneous broadening. However, the dipoles should also experience an intrinsic dephasing process with a dephasing time $T_2$

related to the homogeneous broadening. This intrinsic broadening is not reversible. Photon echoes can appear only before the intrinsic phase coherence of the dipole is destroyed. Therefore, to observe a photon echo, the time delay between the first excitation pulse and the photon echo should not be much longer than $T_2$. The basic form of photon echo, the 2-beam photon echo, is described in the Appendix.

Time domain optical storage on the spectral hole burning material OEP/PS is based on a special kind of photon echo called the 3-beam photon echo by accumulated grating and is shown in figure 2.17. The bandwidth of the excitation pulses should be less than the inhomogeneous broadening $\Gamma_I$, and the time delay between a pair of excitation pulses, $t_{12}$, should be less than $1/\Gamma_H$. When a pair of excitation pulses corresponding to the reference and signal are incident on a PHB material, due to the temporal interference, the power spectrum will be modulated(Fig. 2.17a). The system behaves as a two-level system. It can be shown that immediately after the first two excitation pulses(at time $t_{12}^+$) the lower- and upper-state density-matrix elements have become[22]

$$\rho_{11}(t_{12}^+) = \frac{1}{2}[\,1 + \cos\theta_1 \cos\theta_2 - \sin\theta_1 \sin\theta_2 \exp(-t_{12}/T_2) \cos(\Delta t_{12} + \phi_{12})]\,, \qquad (2.22)$$

$$\rho_{22}(t_{12}^+) = 1 - \rho_{11}(t_{12}^+), \qquad (2.23)$$

where $\theta_i = (\mu_{12}E_0/h)\delta t_i$ is the rotation angle of the Block vector induced by the $i$th excitation pulse, $\Delta$ is the off-resonance frequency, and $t_{12}$ and $\phi_{12}$ are the time duration and phase difference between the excitation pulses. Equations (2.22) and (2.23) show that two excitation pulses produce a grating $[\cos(\Delta t_{12} + \phi_{12})]$ in both ground and excited states. Notice that each grating contains, via the amplitude factor $\exp(-t_{12}/T_2)$, information on the optical phase loss in time between the excitation pulses. As time proceeds a fraction of

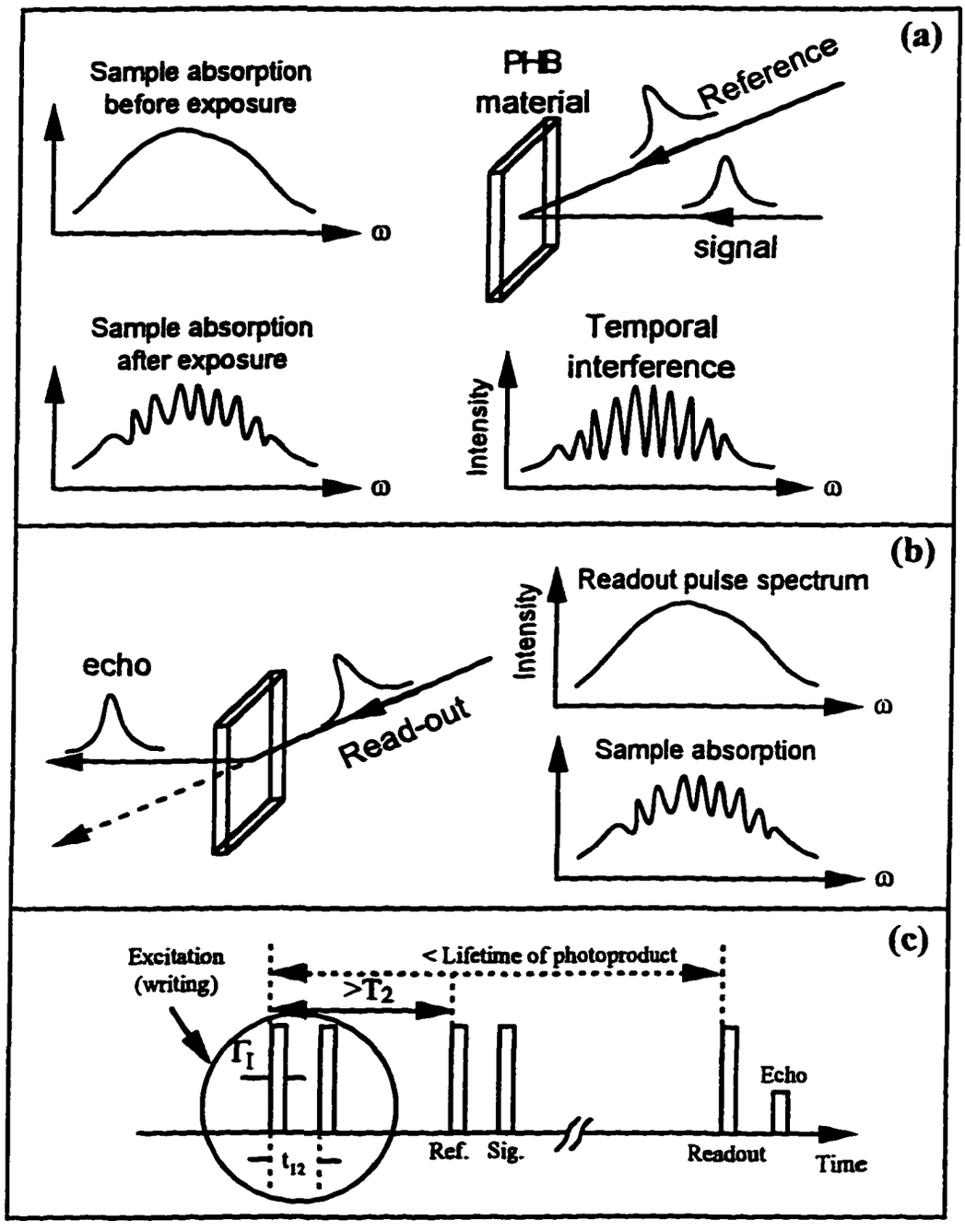


Fig. 2.17 Principle of accumulated photon echo on PHB materials.
(a) Writing, (b) reading and (c) timing sequence.

the molecules in the upper state decays into a photoproduct. At the time that the upper state is effectively depleted, but the grating in the ground state is not, $\rho_{11}(t) = 1 - \rho_{pp}(t)$. Therefore the temporal information is stored in the PHB material for the lifetime of the photoproduct. By applying a train of the twin excited pulses, the modulated part of $\rho_{11}$ builds up in time to a steady value far exceeding the initial one, and thus produces the accumulated population grating. When at a later time(could be very long like days, years depending on the lifetime of the photoproduct) an independent pulse passes such a grating, its spectrum would be modulated by the population grating, and an echo is produced (Fig. 2.17b,c). This is a kind of time domain holography. The photon echo amplitude is proportional to $\exp(-2t_{12}/T_2)$, thus its intensity is proportional to $\exp(-4t_{12}/T_2)$. The optical dephasing time $T_2$ in PHB materials determined by a two-beam echo and the accumulated echo usually are different. This is due to the spectral diffusion effect of a two level system(TLS), which is known to exist in glassy and polymer materials[23]. The long time scale fluctuation of energy levels of such materials leads to the increment of homogeneous broadening $\Gamma_H$, thus reducing the optical dephasing time $T_2$. Since the two-beam echo is obtained on a nanosecond scale or less while the accumulated echo is obtained in seconds or on a longer time scale, the spectral diffusion will certainly be significant in the case of the accumulated echo and insignificant in the case of the two-beam echo.

Two types of experimental setups were used in the studies of photon echoes. The spectral setup and the fast retrieval setup.

The spectral setup is depicted in figure 2.18. The laser beam from a CPM or amplifier is split into two beams. The monitoring beam is coupled into one of the two tracks of the CCD detector through a bundle of optical fibers and a spectrograph. It is used as baseline-reference to compensate for the laser fluctuations. Another beam is further split into a reference beam and a signal beam, and the time delay between them can be varied. The echo can be measured by blocking the signal beam after superimposing the reference and signal on an OEP/PS sample to produce a population grating. The echo is coupled into the remaining track of the CCD. The sample is kept in the Cryostat, in which the temperature can be as low as 1.2 Kelvin. Using this setup, the laser and echo spectra, the echo intensity as a function of time delay between the signal and reference, and the echo intensity as function of temperature can be measured.

The fast retrieval setup is similar to that of the spectral setup and is shown in figure 2.19. It is actually a combination of the echo spectral setup and the interferometric correlator detection technique described in the previous section. Multi-plates of glass inserted into the signal beam produces coded optical pulses. The cross-reference beam forms an interference pattern with the echo signal on the transmission holographic grating, which is conjugated with the CCD camera. The retrieved code is read out as a two-dimensional image on the CCD and processed through the computer.

## 2.5) Time-resolved Pump-probe Transient Absorption Measurements

The pump-probe technique is a basic method for transient absorption spectroscopy.

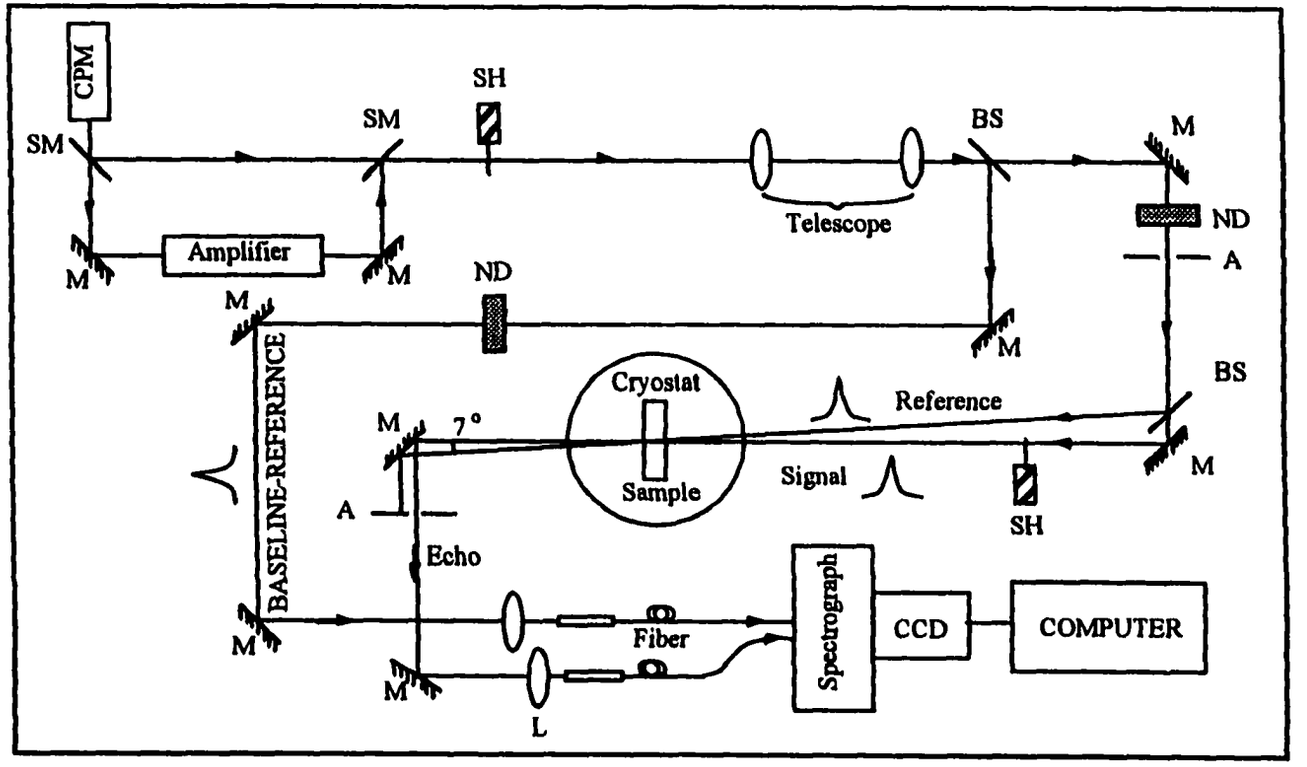


Fig. 2.18 Experimental arrangement for hole burning to measure the spectra of accumulated echo signals: SM's, switch mirrors; M's, mirrors; ND's, neutral-density filters; BS's, beam splitters; SH's, shutters; L, lenses; A's, apertures.

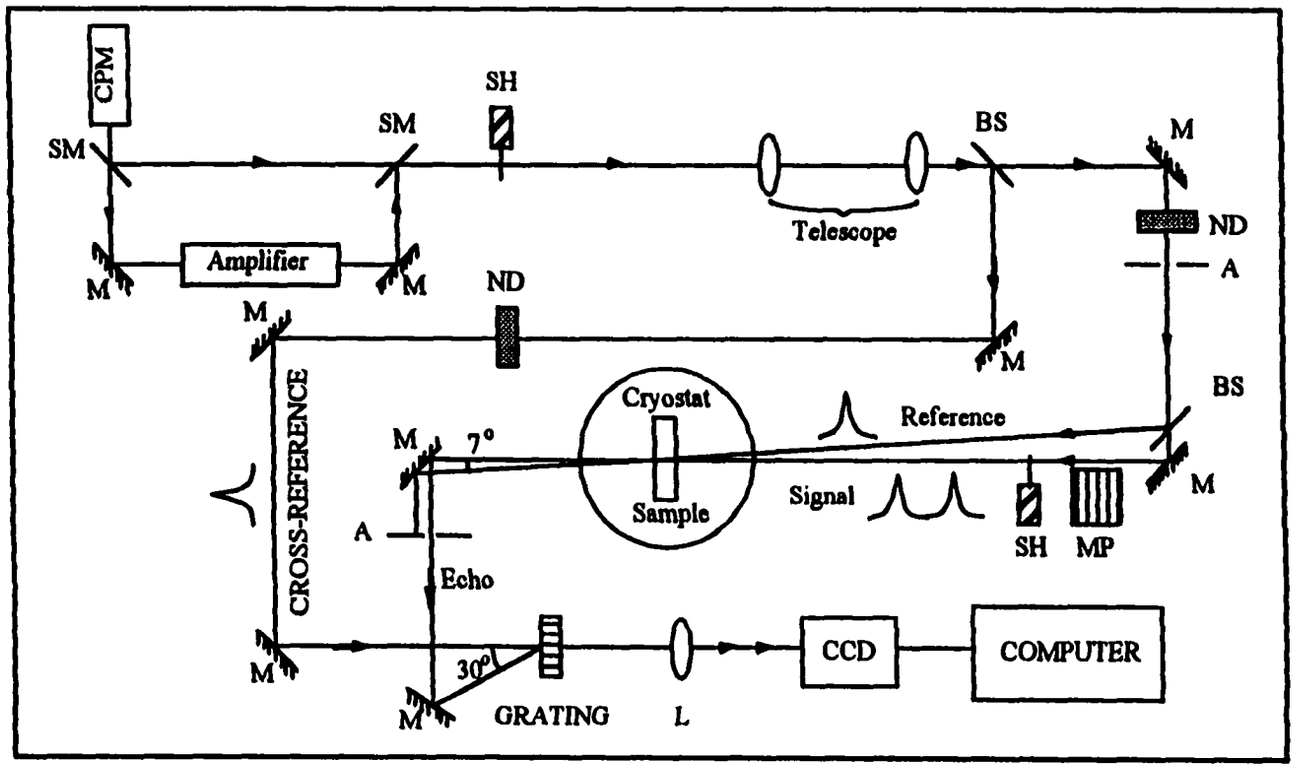


Fig. 2.19 Experimental arrangement for hole burning holography using a CPM laser and ultrafast cross-correlation detection of accumulated echo signals: SM's, switch mirrors; M's, mirrors; ND's, neutral-density filters; BS's, beam splitters; MP, multi-step glass plate; SH's, shutters; L, lens; A's, apertures.

### 2.5.1 Conventional 2-beam pump-probe

The sample is first excited with a strong pump pulse. Its absorption is subsequently measured by a weak probe pulse as the sample material relaxes to its original state or moves through some photochemical reactions. The absorption change for the probe pulse of intensity $I_b(\lambda,t)$ is

$$\Delta\alpha(\lambda,t) = \int_{-\infty}^{\infty} I_b(\lambda,t')\Delta\alpha'(\lambda,t-t')dt' = I_b(\lambda,t) \otimes \Delta\alpha'(\lambda,t) \qquad (2.24)$$

where $\Delta\alpha'(\lambda,t)$ denotes the impulse response of the molecular absorption change. The 2-beam pump-probe setup, for example, in a vision experiment is depicted in figure 2.20. The pump is a 500 nm pulse and the probe is selected by a narrow band filter from the 400 nm-1200 nm continuum. The reference beam is split from the probe beam to compensate for the laser intensity fluctuations. Both beams take about 4% from the continuum via a wedge. The remainder of the continuum is passed through a 500 nm narrow band filter and further amplified to ~1 μJ in a single stage dye amplifier, consisting of 1 cm cell of flowing Coumarin-500 dye in methanol. The pump and probe pulses are focused into the sample by an 8 or 15 cm achromatic lens.

The kinetics of the absorption changes is obtained by measuring the absorption at different time delays between the pump and the probe pulses. The delay is varied by changing the pathlength with a computer-controlled translation stage. The transmitted signal $I_t(\lambda,t)$ and reference signal $I_r(\lambda,t)$ at wavelength $\lambda$ and delay time $t$ are both acquired by S-20 photodiodes and sent to a boxcar integrator at the same time. The

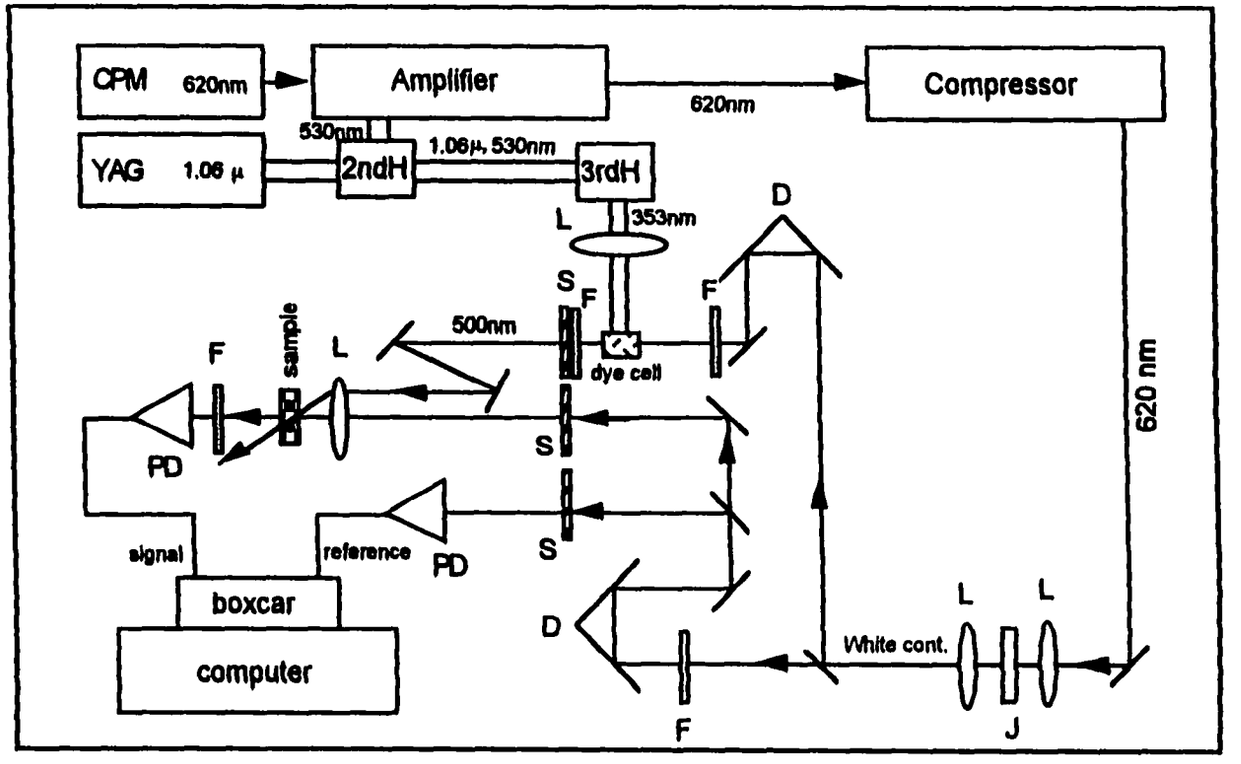


Fig. 2.20 Two-beam pump-probe setup. L: lenses. J: ethylene glycol jet. F: narrow- band filters. S: shutters. D: optical delay lines. PD: photodiodes.

normalized transmission $T(\lambda,t)$ is the ratio $I_t(\lambda,t)/I_r(\lambda,t)$. The transmission change $\Delta T/T+1$ is the ratio of $T(\lambda,t)$ to the transmission $T(\lambda)$ when the pump is blocked. The change in the optical density is:

$$\Delta OD(\lambda,t) = -\log[T(\lambda,t)/T(\lambda)]. \qquad (2.25)$$

In contrast to above the procedure which detects transmission changes in one wavelength at a time, an alternative is to use white light probe and reference pulses focusing into two optical fiber bundles and couple them into separate tracks of a CCD (Photometrics) through a spectrograph(Jarrell-Ash). In this case, the whole spectrum of absorption changes can be obtained at discrete delays. For each delay, however, the dispersion of the white probe (see figure 2.11) must be considered in order to get the correct delay time for each different wavelength.

The temporal resolution of the transient absorption technique is limited only by the duration of the laser pulse. It was determined to be about 200-250 fs at FWHM in the whole visible range by the cross correlation trace using a thin KDP nonlinear crystal. The probe pulse is highly chirped due to self-phase modulation. The zero delay time for each probe wavelength was also determined by cross-correlation.

### 2.5.2 Novel 3-beam pump-probe

To help resolve the controversy on the different rhodopsin models, we have modified the conventional 2-beam pump-probe technique to develop a novel 3-beam pump-probe method. The schematic diagram of the experiment setup and timing are shown in Fig. 2.21 and Fig. 2.22, respectively. The experimental setup consists of three

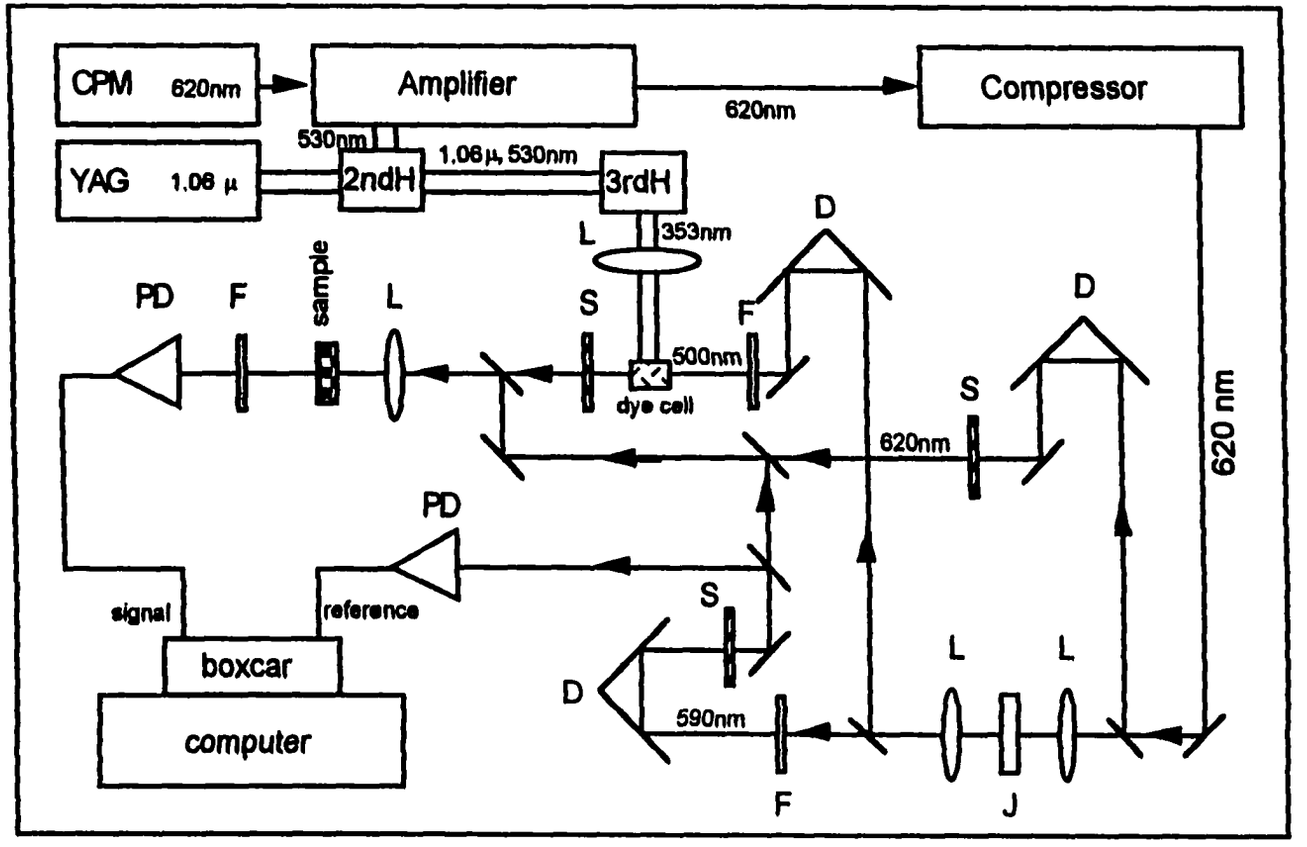


Fig. 2.21 Three-beam pump-probe setup. L: lenses. J : ethylene glycol jet. F: narrow- band filters. S: shutters. D: optical delay lines. PD: photodiodes.

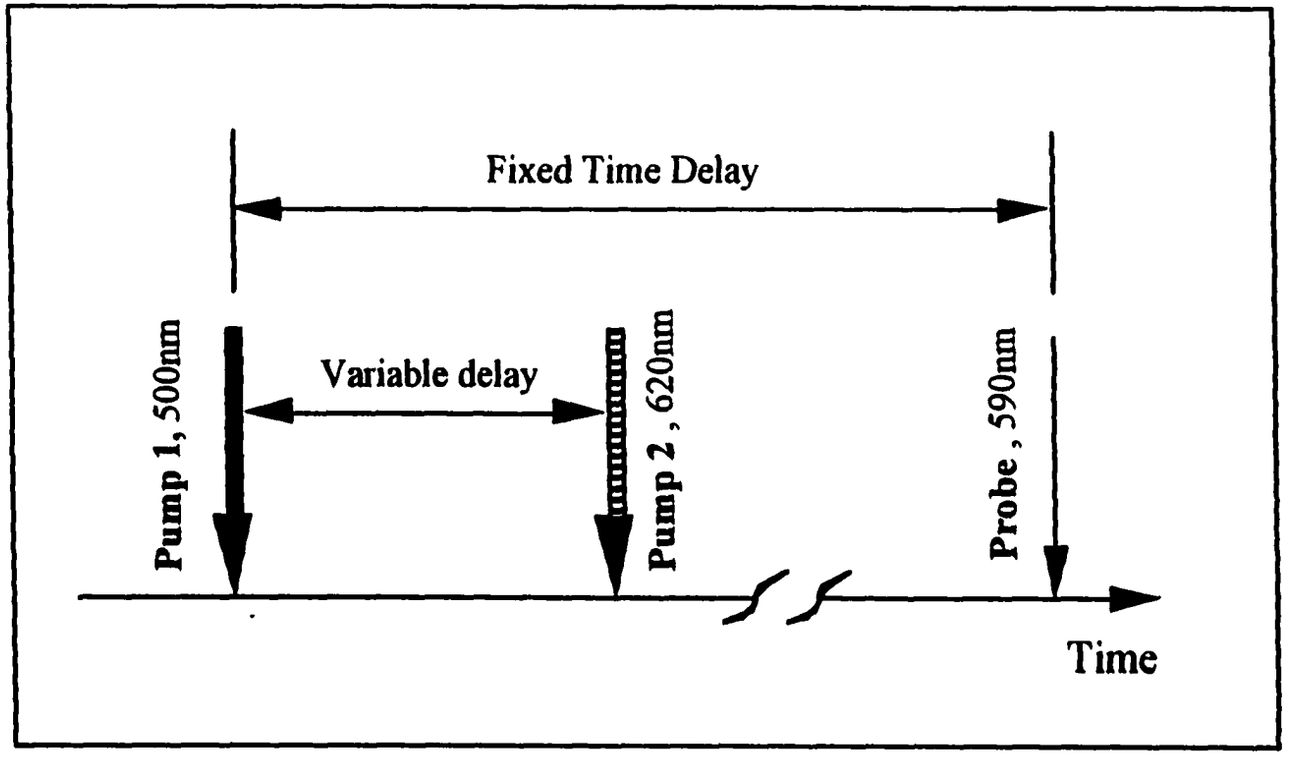


Fig. 2.22 The timing diagram for three-beam experiment.

laser beams: two pump beams and one probe beam. All beams originate from an amplified CPM laser. After pulse compression, the 620 nm laser pulse becomes 150 fs wide with 100 μJ (4-stage amplification) of energy at a 20 Hz repetition rate. The beam is divided by a beam splitter. One part is directed as the second pump and the other is focused on an ethylene glycol cell to generate a white light continuum. Again the white continuum is split into two beams. One beam is spectrally filtered by a 590 nm narrow band filter to become the probe. The remaining portion of the white continuum is filtered by a 500 nm narrow band filter and amplified in a Coumarin-500 dye cell pumped by the third harmonic of a Nd:YAG laser. It generates a 250 fs pulse with 1 μJ of energy and was used as the first pump in the 3-beam experiment. The three beams propagate collinearly through the sample. Narrow band filters are used before the photodiode detector to block the two pump pulses. To compensate for the laser fluctuations a portion of the probe is taken as the reference. Signals from the probe and the reference are sampled by a boxcar averager, and the data are sent to a microcomputer for processing.

The basic principle of the 3-beam pump-probe technique is to use the first pump to excite the molecules, then use the second pump at various time delays to re-excite the photoproduct produced by the first pump excitation. A probe beam at a fixed long time delay detects the change of transmission due to the second pump. Therefore the photoproduct formation time can be determined from the transition time of the transmission change. The 3-beam method is also capable of measuring the excited state dynamics by careful rearrangement of timing after the first pump excitation. At a fixed time delay within the lifetime of the first excited state, the second pump is applied to

excite the molecule to higher excited states. A probe beam with the proper wavelength at various temporal delays monitors the transmission change due to both pumps. By comparison with the result of the 2-beam pump probe measurement, one may extract useful information about excited state dynamics.

## 2.6) 3-beam Stimulated Emission Measurements

In an attempt to improve the writing efficiency on OEP/PS, a 3-beam stimulated emission method was used. The experimental setup is shown in figure 2.23, which is similar to that of the 3-beam pump probe method. The 680 nm pulse selected from the white continuum is amplified by a single stage dye amplifier, consisting of an LDS-698 dye cell transversely pumped by the 530 nm green pulse from the second harmonic of the Nd:YAG laser. In the experimental arrangement, a part of the 620 nm beam after the pulse compressor is separated by a wedge to pump OEP molecules into the first excited singlet state $S_1$. The 680 nm pulse is then applied to the sample within the life time of $S_1$ to bring the molecules down to higher vibrational levels of the ground state by stimulated emission. This new pathway bypasses the first triplet and thus avoids the bottleneck. The hole burning effect is monitored by the third pulse from the sample transmission, before and after the exposure of 620 nm burning pulses. By comparing the results in which the 680 nm stimulated pulse is present or absent, one obtains the change in hole burning efficiency. Two sets of detection apparatus are used. One is the boxcar averager with photodiodes, in which case the wavelength of the third pulse is also 620 nm; The other is

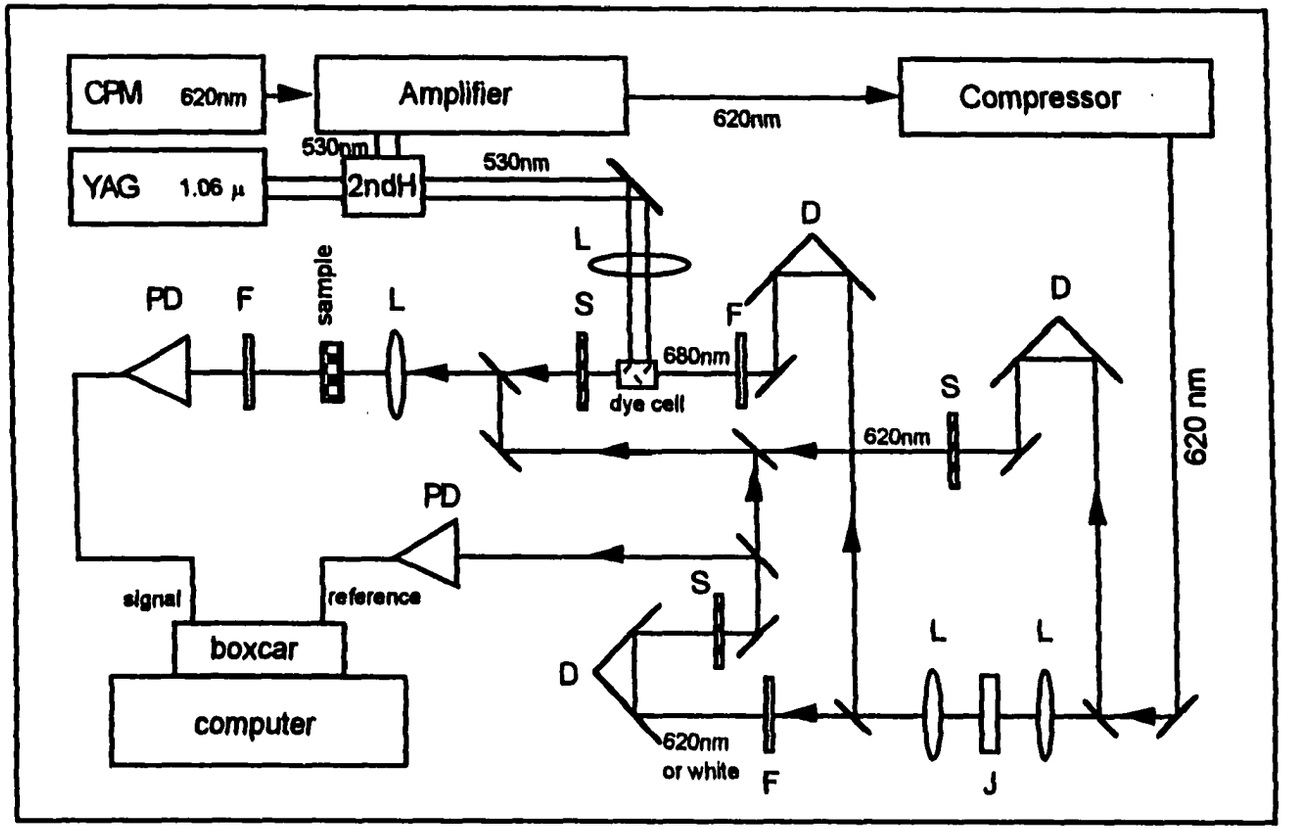


Fig. 2.23 Three-beam stimulated emission setup. L: lenses. J: ethylene glycol jet. F: narrow-band filters. S: shutters. D: optical delay lines. PD: photodiodes.

the spectrograph coupled with a CCD camera, in which case the third pulse is a white continuum.

## References


1. Joachim Herrmann and Bernd Wilhelmi *Lasers For Ultrashort Light Pulses*, Akademie-Verlag Berlin (1987).

2. A. Yariv *Quantum Electronics* 3rd Ed., Wiley, New York(1989)

3. J. T. Verdeyen *Laser Electronics* Prentice-Hall, New Jersey(1981)

4. M. D. Levenson *Introduction to Nonlinear Spectroscopy* Academic Press, San Diego (1981)

5. C. V. Shank in *Ultrafast Laser Pulses and Applications* ed. by W. Kaiser, Topics in Applied Physics **60**, Springer-Verlag, New York (1988)

6. D. J. Bradley in *Ultrafast Laser Pulses ch2* ed. by S. L. Shapiro, Springer-Verlag, New York(1977)

7. R. L. Fork, C. V. Shank, R. Yen and C. A. Hirlimann *IEEE J. Quantum Electron.* **19**, 500(1983)

8. R. L. Fork, B. I. Greene and C. V. Shank *Appl. Phys. Lett.* **38**, 671(1981)

9. M. Stix and E. P. Ippen *IEEE J.* **19**, 250(1983)

10. R. R. Alfano *The Supercontinuum Laser Source*, Springer-Verlag New York(1989)

11. R. L. Fork, C. V. Shank and R. T. Yen *Appl. Phys. Lett.* **41**, 233(1982)

12. F. Salin and A. Brun *J. Appl. Phys.* **61**, 4736(1987)

13. R. L. Fock, O. E. Martinez and J. P. Gondon *Optics Lett.* **9**, 150(1984)

14. R. L. Fock *Optics Lett.* **11**, 629(1986)

15. J. D. Kafka and T. Baer *Optics Lett.* **6**, 401(1987)

16. R. R. Alfano and S. L. Shapiro *Phys. Rev. Lett.* **24**, 584(1970)

17. B. I. Greene, J. Orenstein, R. R. Millard and L. R. Williams *Chem.Phys. Lett.* **139**, 381(1987)

18. E. P. Ippen and C. V. Shank in *Ultrashot light Pulses* ed by S. L. Shapiro, Springer-Verlag, New York (1977)

19. A. G. Doukas, J. Buchert and R. R. Alfano in *Biochemical events Probed by Ultrafast Laser Spectrascopy* ed by R. R. Alfano, Academic Press, San Diego (1982)

20. K. G. Purchase, D. J. Brady and K. Wagner *Optics Letters* **18**, 2129(1993).

21. I. Zeylikovich, Q. D. Liu, G. Bai, N. Zhadin, A. Gorokhovsky and R. R. Alfano *Opt. Commun.* **115**, 485(1995).

22. W. H. Hesselink and D. A. Wiersma *Phys. rev. Lett.* **43**, 1991(1979)

23. R. M. Macfarlane and R. M. Shelby, *Journal of Luminescence* **36**, 179(1987)

# Chapter 3

# Background of Primary Events in Vision

In this chapter, the background of the visual pigment rhodopsin and the visual process is described.

## 3.1) Photoreceptor Cells and the Visual Pigment Rhodopsin

Two different types of light-sensitive cells, called rods and cones because of their shapes, are the photoreceptors of the retina. Cones work in bright light and are responsible for color vision while rods function in low intensity light and are unable to distinguish colors. Visual pigment rhodopsin, a chromoprotein located in rods and cones, is the basis of the vision process. When the photoreceptor cells absorb light, they transmit signals across contact sites (synapses) to nerve cells that are also part of the retina. From there, nerve impulses travel along the optic nerve to the brain[1].

In this thesis, the bovine rhodopsin in rods cells is studied. The visual pigment rhodopsin is embedded in the thin lipid-bilayer membranes of disks as shown in figure 3.1. The disks are closed, flattened sacs about 160 Å thick, and are stacked about a thousand deep in the elongated outer segment of the rod, which has dimensions of a diameter of 1 μm and a length of 40 μm[2]. The disk membranes are separated from the plasma membrane of the outer segment and are densely packed with the photoreceptor molecules rhodopsin. The outer segment of the rod is specialized for photoreception

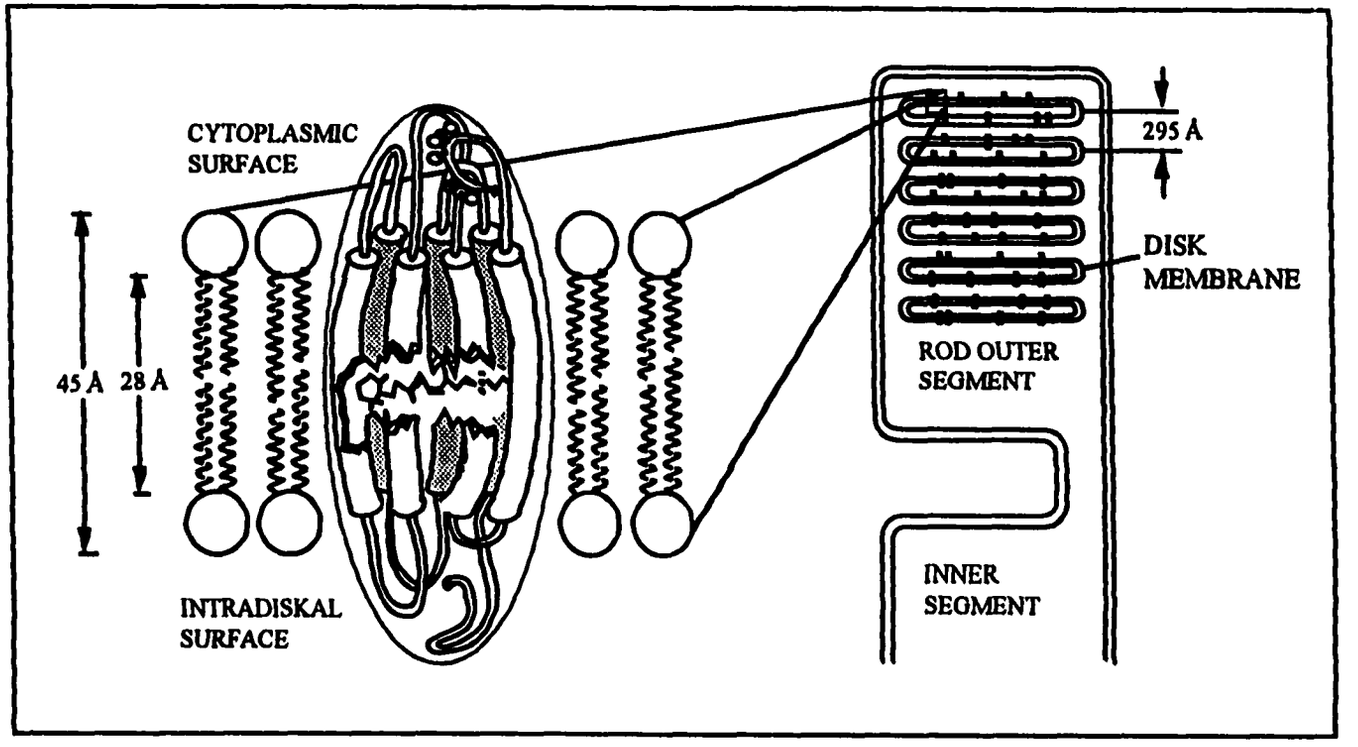


Fig. 3.1 The structure of the rod photoreceptor cells which consists of the disk membrane. The inset shows the helical transmembrane protein segments represented by cylinders located in the lipid bilayer. Retinal lies in the middle of the bilayers and inside of the protein. This drawing is based on similar representations by A. Lewis et al. Physics Today Jan. 1988.

while the inner segment generates ATP at a very rapid rate and is highly active in synthesizing proteins[2-3]. On one end the cell forms a synapse, which fires a signal to the brain after light is absorbed. Rhodopsin is an integral membrane protein containing seven transmembrane helices[1-3]. It contains a chromophore 11-*cis* retinal and a protein generally called opsin. Retinal (a vitamin A derivative) is bonded to the protein by a protonated Schiff base linkage. This 11-*cis* retinal chromophore lies in a pocket of the protein, near the center of the bilayer membrane, with its long axis nearly parallel to the plane of the membrane.

## 3.2) Photobleaching Sequence in Rhodopsin and the Visual Process

At ambient temperature and neutral pH, rhodopsin undergoes the photobleaching sequence shown in figure 3.2. Absorption of a photon by rhodopsin produces a red-shifted pigment called bathorhodopsin. The rhodopsin to bathorhodopsin phototransformation process represents the so-called "primary event". The primary event stores about 32 kcal/mol of energy[4-5]. All subsequent reactions are thermal. The observation of a photochemical equilibrium among rhodopsin (11-*cis*), bathorodopsin and isorhodopsin (9-*cis*) provided the first experimental evidence that the chromophore in bathorhodopsin has an all-*trans* conformation[6]. The spectrum of the primary photoproduct in resonance Raman experiments is consistent with a protonated all-*trans* isomer. A large body of evidence firmly established that the primary event involves an 11-*cis* to all-*trans* isomerization. This isomerization alters the geometry of the retinal as indicated in figure 3.3. The Schiff base linkage of retinal moves approximately 5 Å

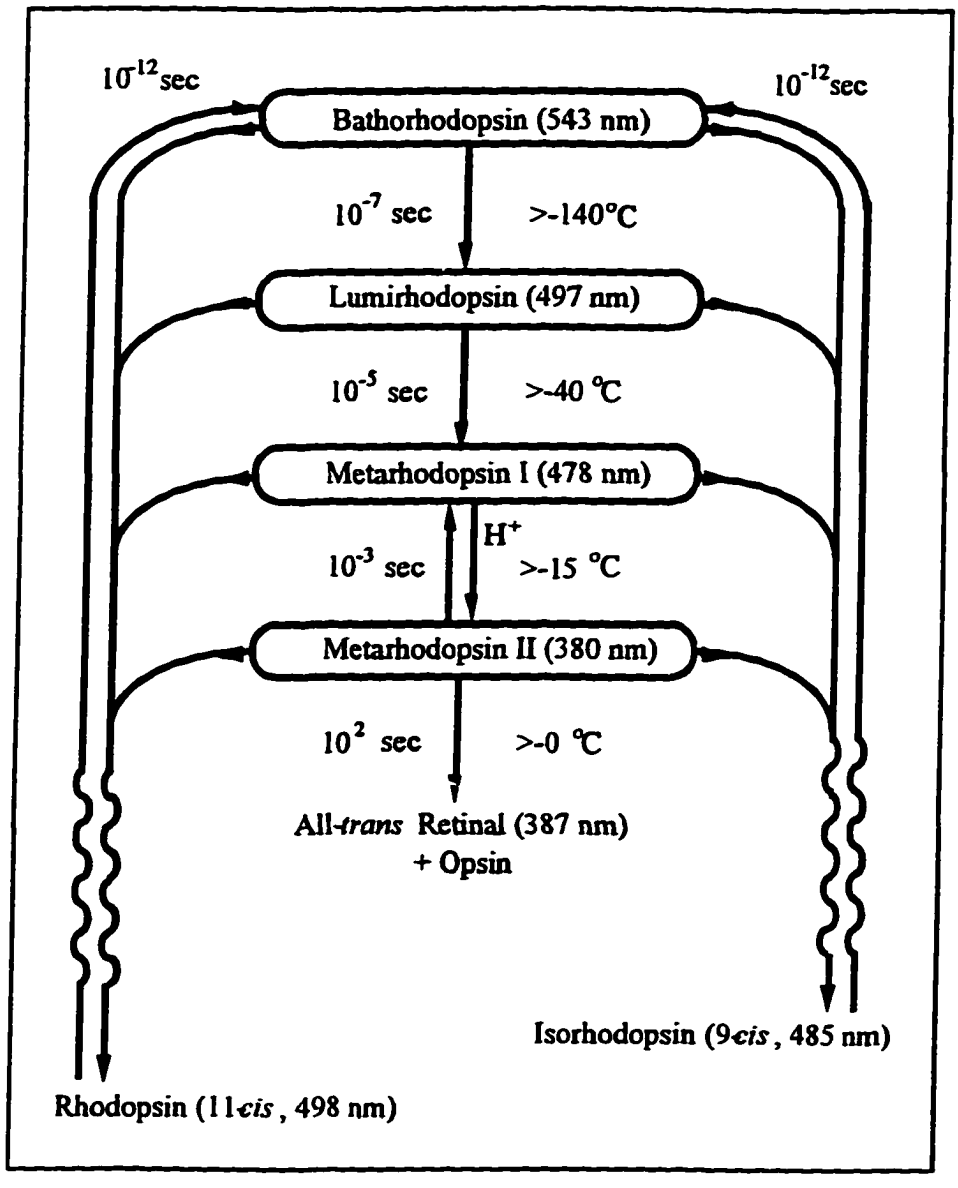


Fig. 3.2 Bleaching sequence of cattle rhodopsin. Photoreactions are denoted by wavy lines and thermal reactions by straight lines.

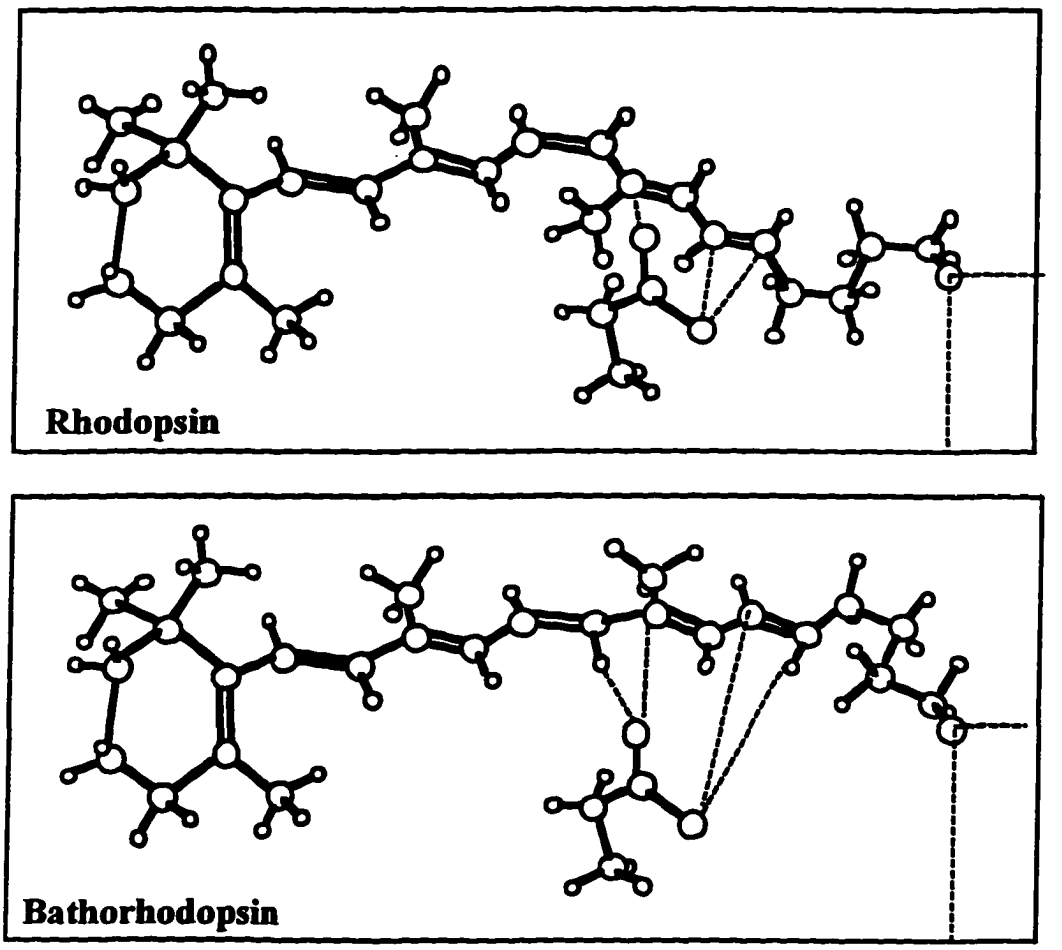


Fig. 3.3 The model of the binding site of rhodopsin (top) and the primary photochemical event that generate bathorhodopsin (bottom). From J. R. Tallent et al. J. Am. Chem. Soc. 114, 1581 (1992).

relative to the ring portion of the chromophore[3, 7-9]. Thus, photon energy absorbed by rhodopsin has been converted into atomic motion. Bathorhodopsin is thermally unstable at room temperature. Both retinal and the protein continuously change their conformations. The bleaching sequence after bathorhodopsin forms several thermal intermediates, including lumirhodopsin, metarhodopsin I and metarhodopsin II, and eventually leading to the release of retinal from the protein[3, 10-11] and visual excitation. The intermediates were first identified by their low temperature absorption spectrum, beginning with the red shifted species bathorhodopsin which was identified at 77K[10-11]. Each intermediate is stable below a transition temperature[10]. Resonance Raman and other experimental studies[3] indicate that the chromophore is protonated in rhodopsin, bathorhodopsin, lumirhodopsin and metarhodopsin I. The Schiff base linkage (figure 3.3) becomes deprotonated in the transition from metarhodopsin I to II, which takes about a millisecond at 300 K[3]. Metarhodopsin II triggers a series of enzymatic reactions that ultimately hyperpolarize the plasma membrane of the rod cells in the retina to generate a nerve pulse [12]. The sequence ends in about a minute with the detachment of the chromophore from the protein to yield an opsin and an all-*trans* retinal. The retinal diffuses away from the protein because it does not fit into the bonding site for the all-*trans* isomer. The all-*trans*-retinal is isomerized in the dark to 11-*cis*-retinal on the behalf of enzymes, which associate with opsin to generate rhodopsin[12]. As a consequence, a single photon generates a nerve impulse which hyperpolarizes membranes close to 1 mV. The trigger for these sequential conformational changes that leads to the visual excitation involves the photochemistry of the *cis-trans* isomerization of the chromophore. This primary event in visual excitation is the main focus of this thesis. Much experimental

evidence[2] shows that the primary process of vision occurs at a picosecond time scale. Therefore, picosecond or femtosecond transient measurements must be applied to understand this first step of the visual process.

## 3.3) The Primary Event of Vision

In the process of vision, light is only involved in the primary event, the transformation of rhodopsin (11-*cis*) to bathorhodopsin (all-*trans*), and plays no further role in the subsequent process. Now it is generally accepted that only the C11=C12 double bond isomerizes during the primary event. It breaks the ionic bond between the protonated Schiff base and a counter ion located in the protein, involving the conformational rearrangement of a large fraction of the retinyl polyene. The complex motions of the lysine residue accompanying the chromophore isomerization remains a subject of active experimental and theoretical studies[3]. The quantum efficiency of photoisomerization from rhodopsin to bathorhodopsin is at least two times larger than that of the 11-*cis*-retinyl protonated Schiff base (RPSB) in solution which indicates that the protein has a binding site optimized for 11-*cis* $\rightarrow$ 11-*trans* photoisomerization. The fact that the primary event stores about 32 kcal/mol, whereas the photoisomerization of the 11-*cis*-RPSB in solution generates a more stable species, provides further evidence that the protein is modifying both the ground and excited state potential surfaces. The excited state C11=C12 torsional surface is barrier-less[3]. About 60% of the absorbed photon energy is converted into chemical energy. The high value of energy storage is due to the charge separation ($\approx$ 12 kcal/mol) and conformational distortion, which includes

the intrachromophore-lysine conformational distortion (≈10 kcal/mol) and the chromophore-protein conformational distortion (≈10 kcal/mol). The conjugated polyunsaturated chain of 11-*cis*-retinal gives rhodopsin the ability to absorb light over a broad region of the visible spectrum with a peak at 500 nm, which nicely matches the solar output. The absorption coefficient of rhodopsin at 500 nm is about 40,000 $cm^{-1}M^{-1}$[11-12]. The integrated absorption strength in the visible band is very large among organic compounds. The different absorption maxima of rhodopsin in comparison with retinal in solution (380 nm) is caused by the interaction between the proteins and the chromophore. It is believed[12] that the protein affects the absorption by changing the degree of delocalization of the $\pi$ electron system of the chromophore. The observation that bathorhodopsin forms within a few picoseconds or less places rather severe constraints on the nature of the excited state dynamics. Molecular dynamics calculations on the primary event predicted a bathorhodopsin formation time of 1.3~2.3 ps with a quantum yield of 0.698[3, 9]. How this conformational change occurs and how fast the isomerization is completed is addressed in this thesis.

## References


1. S. P. Zurer *C&EN Washington* **Nov.**, 25(1983)

2. A. Lewis and L. V. Del Priore *Phys. Today* **Jan.**, 38(1988)

3. R. R. Birge *Biochimica Biophysica Acta* **1016**, 293(1990) and references therein

4. A. Cooper *Nature (Lond.)* **282**, 531-533(1979)

5. G. A. Schick, T. M. Cooper, R. A. Holloway, L. P. Murray and R. R. Birge *Biochemistry* **26**,2556-2562(1987)

6. T. Yoshizawa and G. Wald *Nature (Lond.)* **197**, 1279(1963)

7. R. R. Birge *Ann. Rev. Phys. Chem.* **41**, 683(1990)

8. R. R. Birge, C. M. Einterz, H. M. Knapp and L. P. Murray *Biophys. J.* **53**, 367(1988)

9. J. R. Tallent, E. W. Hyde, L. A. Findsen, G. L. Fox, R. R. Birge *J. Am. Chem. Soc.* **114**, 1581(1992)

10. R. H. Callender in *Biochemical events Probed by Ultrafast Laser Spectrascopy ch9* ed by R. R. Alfano, Academic Press, San Diego (1982)

11. R. M. Hochstrasser and C. K. Johnson in *Ultrafast Laser Pulses and Applications* ed. by W. Kaiser, Topics in Applied Physics **60**, Springer-Verlag, New York (1988)

12. A. Stylere *Biochemistry* 3rd Edition, John Wiley & Sons, New York(1990)

# Chapter 4

# Previous Experiments and Models of Primary Event of Vision

There has been significant interest and extensive research in the visual process ever since George Wald investigated the bleaching sequence of visual pigment rhodopsin and the interconvertability between rhodopsin, bathorhodopsin and isorhodopsin 40 years ago[1-3]. Many experiments and theoretical simulations aimed at understanding the primary event of vision. Several prominent models have been proposed in an attempt to elucidate the molecular basis of visual excitation.

In this chapter, I will describe some of the important previous experimental results and the theoretical calculations based on them.

## 4.1) Resonance Raman Measurements

Resonance Raman spectroscopy is uniquely suited to probe the *in situ* conformation of retinal. The resonance enhanced spectra are due only to vibrational modes of the chromophore, and of adjacent opsin residues which couple to the visual absorption band. Other membrane components do not significantly contribute to the observed scattering.

Low-temperature resonance Raman spectroscopy has been used to study the conformation and interactions of retinal within the opsin binding site in disk membrane vesicles. Oseroff and Callender showed that the linkage between retinal and opsin is a

protonated Schiff base[4], which can therefore account for part of the red-shifted absorption of the visual pigment. The bathochromatic shift is due to increased delocalization of the $\pi$ electrons of the polyene chain. The mechanism for this delocalization involves the interaction between retinal and opsin residues at the binding site.

Experiments[5-6] indicated that the strength of the C=N bond and the degree of protonation of the Schiff base nitrogen are the same in bathorhodopsin, rhodopsin and isorhodopsin, at both room and low temperature. These results suggest that proton transfer is at a later stage than ground state relaxation at opsin. The fact that bathorhodopsin lines are nearly identical at both temperatures implies that the retinal conformation in bathorhodopsin formed at low temperature is the same as that formed at room temperature.

Resonance Raman measurements[1-13] have provided the most compelling evidence that Wald's original proposal was correct. The primary event in the visual pigment is *cis* to *trans* isomerization. Identical results at 5.5K, 88K and ambient temperature showed that the common intermediate bathorhodopsin is formed from either rhodopsin or isorhodopsin[7] (see Fig 4.1[8]). Rhodopsin has a 11-*cis* retinal chromophore and isorhodopsin has a 9-*cis* retinal chromophore. The interconversion between rhodopsin, bathorhodopsin and isorhodopsin naturally leads to the suggestion that the chromophore of bathorhodopsin is all-*trans*. Molecular flow resonance Raman measurements of retinal isomers in solution (all-*trans*, 11-*cis*, 9-*cis*, and 13-*cis*) and bovine rhodopsin near physiological temperatures[9] found that each of them has a distinct and characteristic

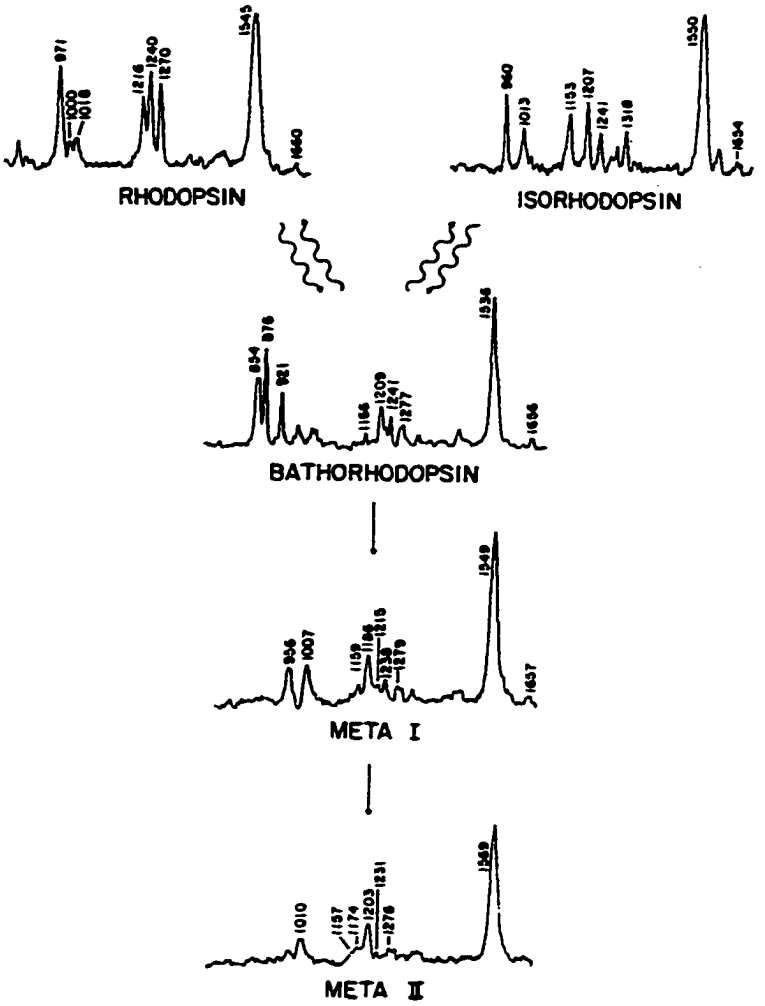


Fig. 4.1 Resonant Raman spectra of rhodopsin and its photolytic intermediates. The bathorhodopsin spectrum was obtained with a 568-nm probe beam and a 476-nm pump beam using the spinning cell technique at 77 K.

Raman spectra. The spectrum of 11-*cis*-retinal is quite similar but not identical to that of rhodopsin. The same relationship holds for 9-*cis*-retinal and isorhodopsin. The conformation of the rhodopsin chromophore is a distorted 11-*cis*, 12-s-*trans*[9-10] while that of bathorhodopsin is a distorted all-*trans*[4, 11-12]. The Raman spectrum of bathorhodopsin is significantly different from that of either parent pigment, rhodopsin and isorhodopsin. Thus the geometric change in the chromophore is an important component of the primary photochemical event of vision[6]. The bathorhodopsin spectrum is also different from the spectra of all-*trans* model compounds in that it has major bands at 856, 877, and 920 $cm^{-1}$. Resonance Raman studies of visual pigment analogues assigned these lines to isolated 14, 10, and 11 hydrogen out-of-plane(HOOP) wagging modes of the retinal chromophore.

The resonance Raman intensities have been used to analyze the excited-state structure and isomerization dynamics of the retinal chromophore in rhodopsin[13]. The excited state wavepacket is found to leave the Frank-Condon region very rapidly, in 30~35 fs, and will reach a $90^0$ torsional angle in only 100 fs, suggesting that isomerization could occur as fast as 0.2 ps.

The picosecond resonance Raman technique[14] shows that resonance Raman lines characterastic of a distorted all-*trans* retinal appear within 30 ps after photolysis of rhodopsin or isorhodopsin. This suggests that isomerization is nearly complete within picoseconds of the absorption of a photon.

Measurements and analyses of resonance Raman spectra strongly support the model that the primary event of the visual process is a *cis-trans* isomerization about the

C11=C12 double bond in the retinal chromophore of rhodopsin with a nearby single bond twisted.

## 4.2) Fluorescence Kinetic Measurements

One of the important problems in the visual process lies in understanding the nature of the interaction between the protein and chromophore. Fluorescence measurements can complement the absorption measurements as they provide information about the excited state of the chromophore in the binding site. Fluorescence from rhodopsin is difficult to observe, because the expected quantum yield is small and because the fluorescence from impurities in the samples can mask the intrinsic fluorescence from rhodopsin. Doukas *et al*[15] reported the first direct fluorescence kinetics from bovine rhodopsin and isorhodopsin using a single picosecond laser pulse at room temperature. Two emission components are generally observed as shown in figure 4.2. The "fast" component of 12 ps (resolution limited) is from the intrinsic fluorescence emission. The "slow" component with a lifetime of approximately 250 ps is from fluorescing impurities in the sample. The fluorescence quantum yield for bovine rhodopsin at room temperature is determined[16] to be $1.3(\pm 0.5)\text{x}10^{-5}$. Measurements on a nonbleachable analogue of bovine rhodopsin with a seven-member ring fixed 11-*cis* geometry(Rh7) at room temperature[17] showed a markedly different fluorescence behavior. It has a $25 \pm 12$ ps rise time and a $55 \pm 10$ ps decay time. The fluorescence quantum yield is $\sim 4\text{x}10^{-4}$, which is 40 times larger than natural rhodopsin. Therefore, the 11-*cis* to *trans* isomerization of the retinal moiety is the crucial primary event in the

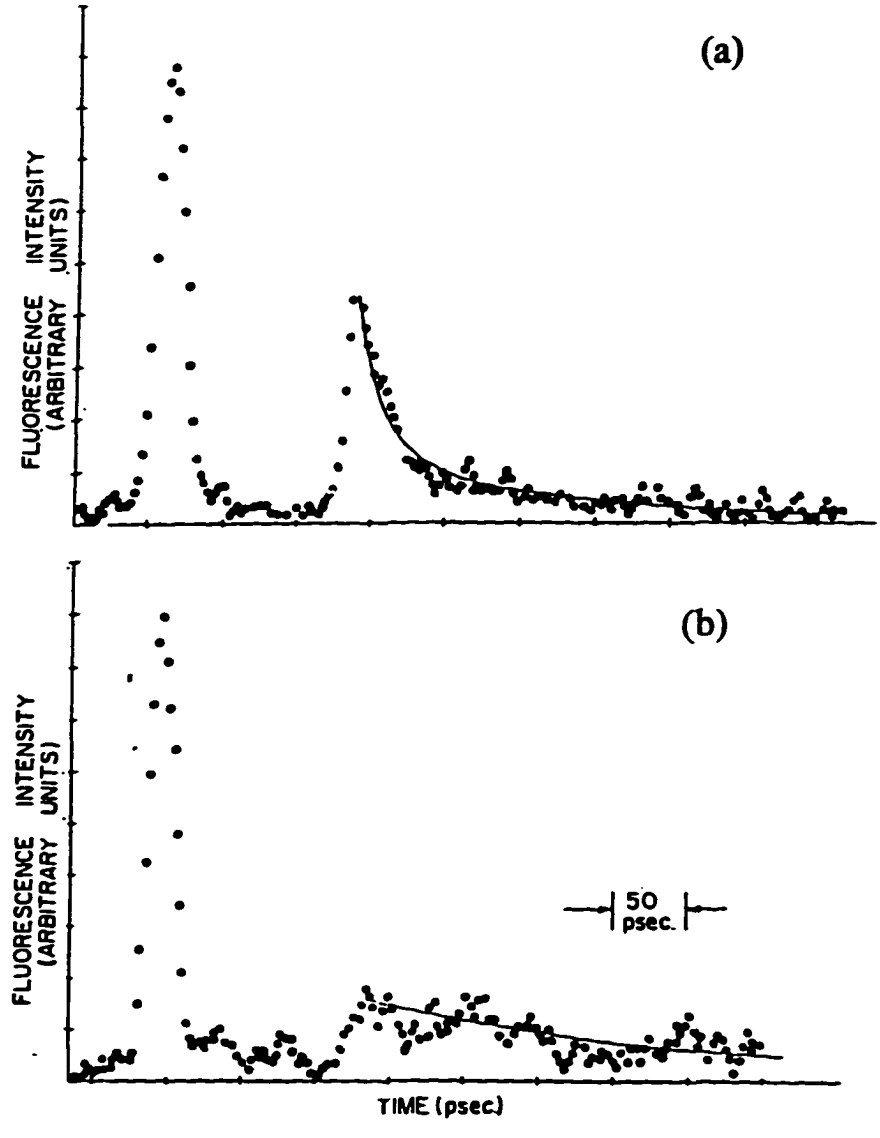


Fig. 4.2 Fluorescence kinetics integrated from 560 to 800 nm of (a) bovine rhodopsin in suspension and (b) bleached rhodopsin in the presence of hydroxylamine. Both spectra were produced by exciting with a 527-nm laser pulse. The sharp pulse on the left in either (a) or (b) is the calibration pulse. Curve (a) is fitted to a double exponential (solid line), a "fast" component of 12 ps (resolution limited) and a "slow" component of 250 ps. Curve (b) is fitted to a single exponential (solid line) of 250 ps.

photolysis of rhodopsin, and the isomerization must occur on the picosecond time scale or faster. The extremely low fluorescence quantum yield implies the existence of a rapid process competing with emission. Since the estimated radiative lifetime of rhodopsin is 5 ns[15], the rate constant of such a process should be on the order of ~0.1 ps. Given the large quantum yield for isomerization of rhodopsin's retinal chromophore(~67%), it is strongly argued that this process corresponds to motion along retinal's C11=C12 torsional coordinate that leads to *cis-trans* isomerization. The above analysis requires the existence of a barrier-less excited state potential curve along the C11=C12 torsional coordinate[16](Fig. 4.3).

The fluorescence kinetics of rhodopsin was also determined at low temperatures in the range of 5-40K[18]. The kinetics remains unresolved even at 5K due to the 12 ps equipment resolution. The fluorescence quantum yield remains unchanged within statistical variations. Deuteration does not cause any effect even at 5K. The quantum yields are identical for rhodopsin in $D_2O$ and $H_2O$. These observation are in marked contrast with the formation kinetics of bathorhodopsin at low temperatures[19]. The implication is that the process competing with fluorescence is not the proton translocation but the unusually fast barrier-less isomerization of the C11=C12 double bond of the rhodopsin chromophore[18, 20].

## 4.3) Picosecond and Femtosecond Transient Absorption Measurements

Rhodopsin($\lambda_{max}$ = 498 nm for bovine rhodopsin) and bathorhodopsin($\lambda_{max}$ = 543 nm) differ substantially in their absorption maxima(Fig. 4.4), therefore, the primary event

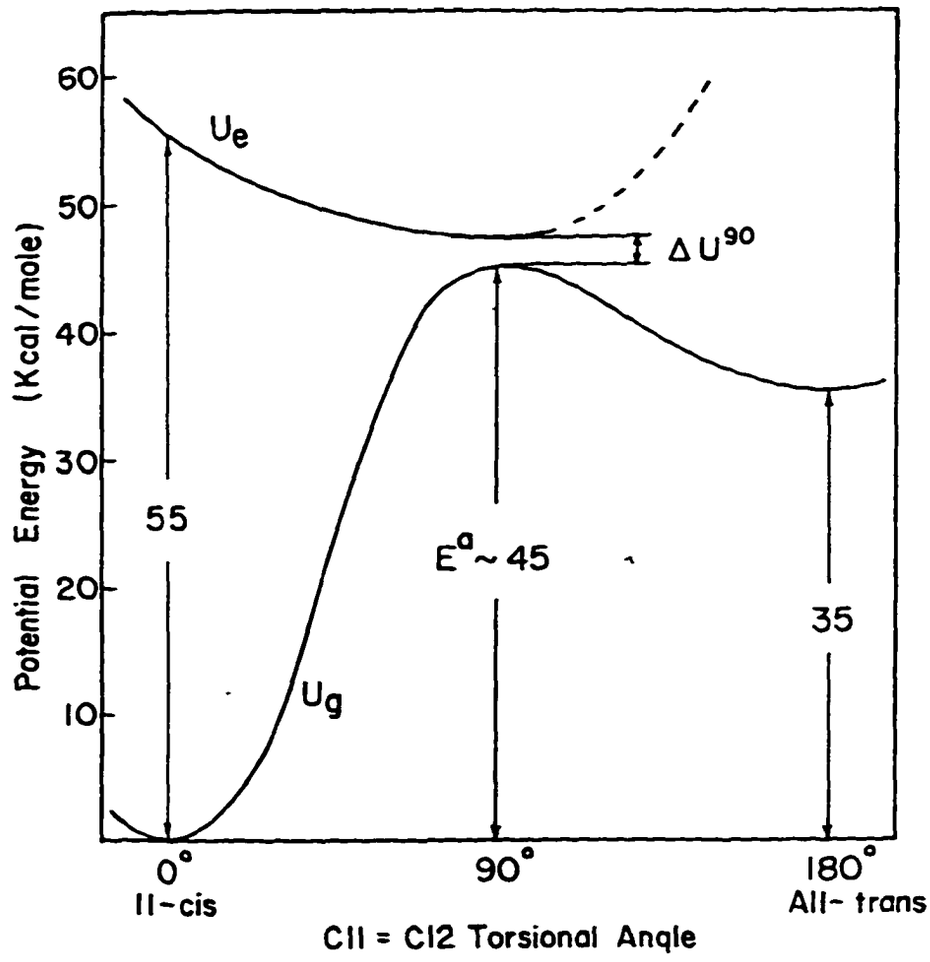


**Fig. 4.3 A scheme of the ground- and excited-state potential surfaces along the chromophore C11-C12 torsional coordinate.**

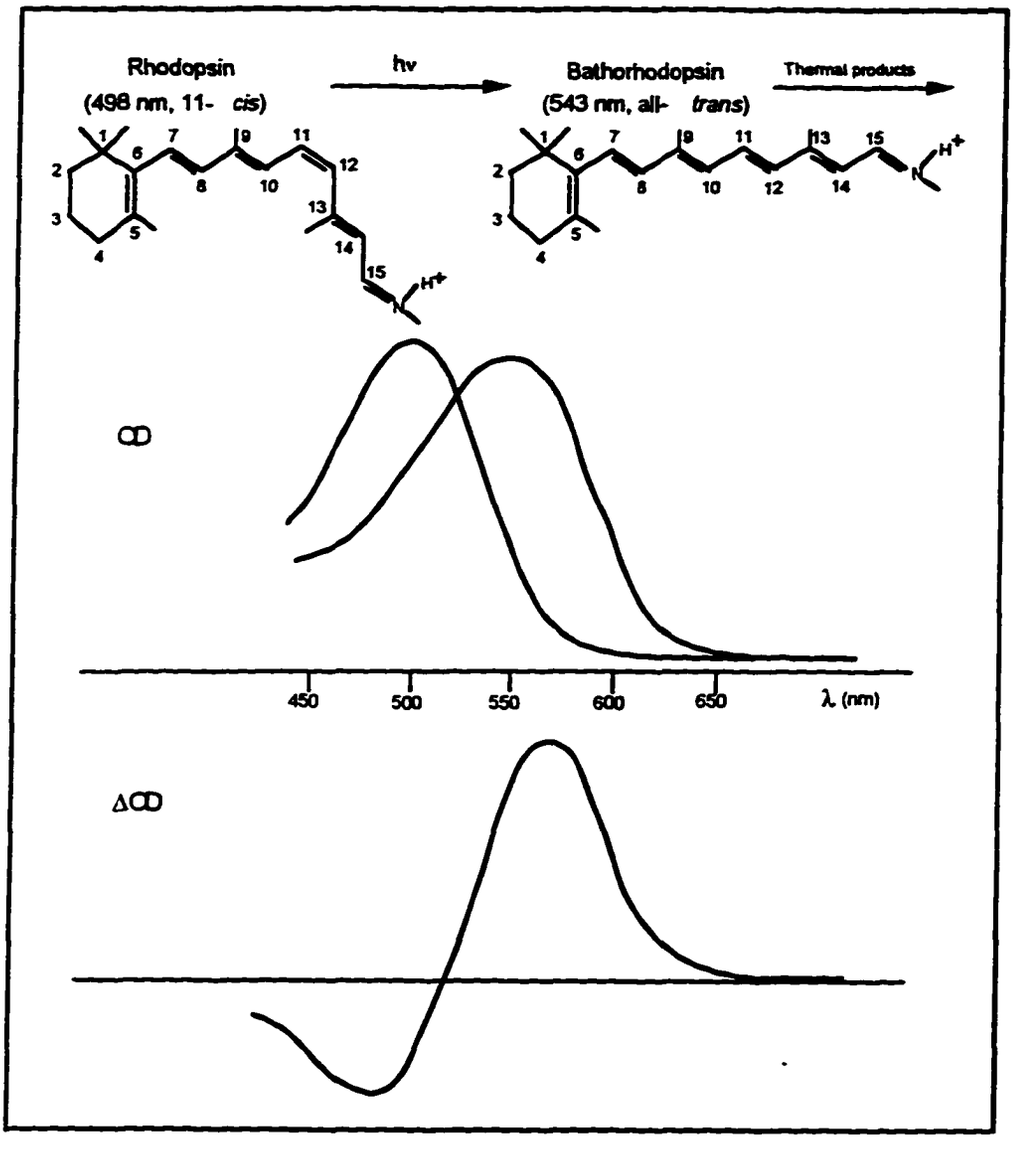


Fig. 4.4 The absorption spectra of the *11-cis* rhodopsin and *all-trans* bathorhodopsin (top), and the differential absorption spectrum between rhodopsin and bathorhodopsin (bottom). The excitation wavelength is 500 nm.

can be studied by transient absorption spectroscopy. Since the process is extremely fast, picosecond or subpicosecond laser pulses should be used.

### 4.3.1 Early transient absorption experiments

Busch *et al.*[21] performed the first picosecond absorption spectroscopy on rhodopsin. With 530 nm photoexcitation of rhodopsin, the induced absorption in the bathorhodopsin region is probed at 560 nm. They found that bathorhodopsin formation occurred faster than their instrumental resolution of 6 ps. The result was confirmed by many groups in subsequent experiments on different samples and under different conditions[19, 22-26]. Green *et al.*[22] also obtained the result that bathorhodopsin was formed in approximately 3 ps. Such a fast process prompted some speculation as to whether a major rotation about the retinal chromophore C11=C12 double bond could occur within 3 ps, as required by the 11-*cis* to *trans* isomerization model for the rhodopsin-bathorhodopsin transformation. Theoretical considerations showed that such fast rotations upon the absorption of a photon are possible[16, 27-32], even likely, for isomers of a protonated Schiff base. In addition, the artificial pigment isorhodopsin(9-*cis* chromophore) also forms bathorhodopsin within 6 ps[22]. The fact that the common bathorhodopsin was formed from two different *cis* isomers, both in less than 6 ps, argued that a very fast rotation must occur in the primary event.

Peter *et al.*[19] studied the kinetics of bathorhodopsin(formerly prelumirhodopsin) formation in deuterium-exchanged samples at low temperatures(4-50K). The formation kinetics could be resolved at very low temperatures and were markedly affected by suspending samples in $D_2O$ (see Table 4.1). A strong non-Arrhenius behavior and a large

TABLE 4.1 The formation time of bathorhodopsin at low temperatures[19-20]

| Temperature (K) | Rhodopsin in $H_2O$ (ps) | Rhodopsin in $D_2O$ (ps) |
|---|---|---|
| 50 | | <6 |
| 40 | | 17±2 |
| 30 | <6 | 51±5 |
| 20 | 9±2 | 175±13 |
| 10 | 29±2 | |
| 4 | 36±2 | 257±28 |

isotope effect($k_H/k_D \approx 7$), see Fig. 4.5, were taken as evidence for quantum mechanical tunneling of a proton along the protonated Schiff base hydrogen bond during the photoexcitation process leading to the formation of bathorhodopsin. Since the deuterated Schiff base would be expected to have no effect on a *cis-trans* isomerization, they deduced that proton translocation is a primary event of vision. However, the suggestion that the Schiff base proton translocated during bathorhodopsin formation is inconsistent with resonance Raman studies(see Section 4.1). It seems bathorhodopsin formation involves two processes at low temperature. The ordering of those two process appears to have been resolved by picosecond fluorescence studies(Section 4.2), which suggests that isomerization occurs first[20]. Indeed, recent femtosecond transient absorption spectroscopy at physiological temperature shows no deuteration effect on bathorhodopsin formation[33], indicating that *cis-trans* isomerization is the primary event of vision.

### 4.3.2 Most recent transient absorption experiments

The fastest of the transient absorption experiments described in the previous section, using instrumental resolution of ~6 ps, were unable to resolve the rhodopsin to bathorhodopsin photoconversion at room temperature. Whether the formation of bathorhodopsin would be isotope dependent at room temperature remains a question to be answered.

Recent advances in the generation of ultrafast optical pulse have made sensitive measurements on a subpicosecond time scale possible. The ultrafast transient absorption spectroscopy measurements on rhodopsin at physiological temperature using femtosecond (10 - 250 fs) pump-probe techniques have been performed by two separate

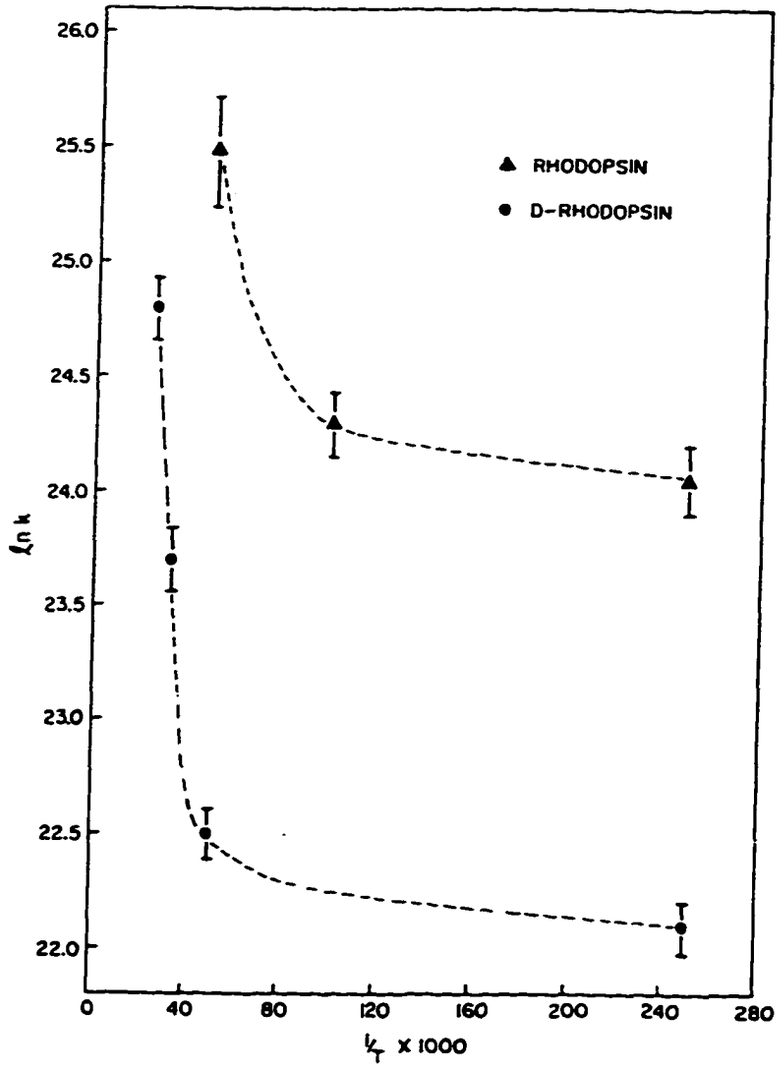


Fig. 4.5 An Arrhenius plot of formation of Bathorhodopsin (formerly prelumirhodopsin) versus 1/T (K) × $10^3$. The value *ln k* = 25.84 corresponds to a lifetime of 6 ps.

groups[33-34]. Similar experimental results were obtained(Figs. 4.6, 4.7). With ten to a hundred times better time resolution than previous experiments, the kinetics of the primary event from rhodopsin to bathorhodopsin conversion has been resolved.

Two prominent models were proposed based on each of their own group's experiments.

Model I[33, 35] is based on the experimental results shown in Fig. 4.6. When exciting rhodopsin by a pump pulse at 500 nm, bleaching with a 3 ps recovery time is observed when probing at 525 nm, this implies a species existing for at least 3 ps. When probing at 620 nm, however, an induced absorption with an unresolved rising edge and two exponential decays of 200 fs and 3 ps is observed. The time resolution of this experiment is about 300 fs. Based on the analysis of these results and theoretical calculations[28-29], the authors concluded that a Frank-Condon state and a 90° excited state are two precursors to bathorhodopsin(Fig. 4.8):

$$\text{Rh(11-}cis\text{)} \xrightarrow{h\nu} \text{Rh*(FC)} \xrightarrow{t=200\ \text{fs}} \text{Rh*(S1)} \xrightarrow{t=3\ \text{ps}} \text{Bathorhodopsin(All-}trans\text{)}$$

$$90°$$

The 200 fs decay at 620 is due to the Frank-Condon species and the 3 ps decay is due to the 90° excited state. It also explains the 3 ps bleaching recovery at 500 nm, since one third of the excited rhodopsin molecules go back to the rhodopsin ground state and two thirds form the photoproduct bathorhodopsin. Therefore, the bathorhodopsin formation time is 3 ps.

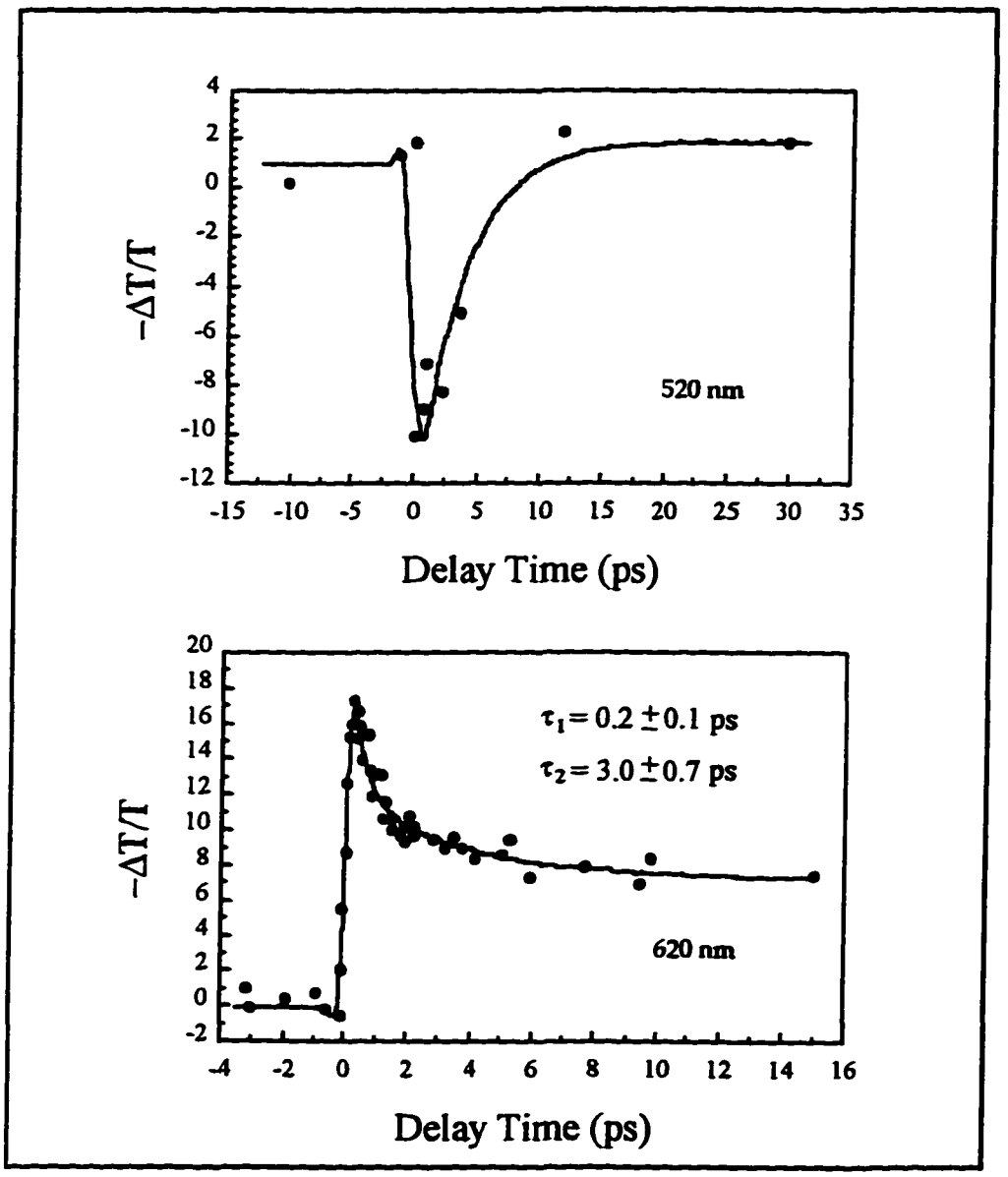


Fig. 4.6 Absorption changes at 520 nm and 620 nm induced by a 500 nm pump as a function of pump-probe delay time. The time resolution is approximately 300 fs. The dots are experimental data and the solid lines are theoretical fittings.

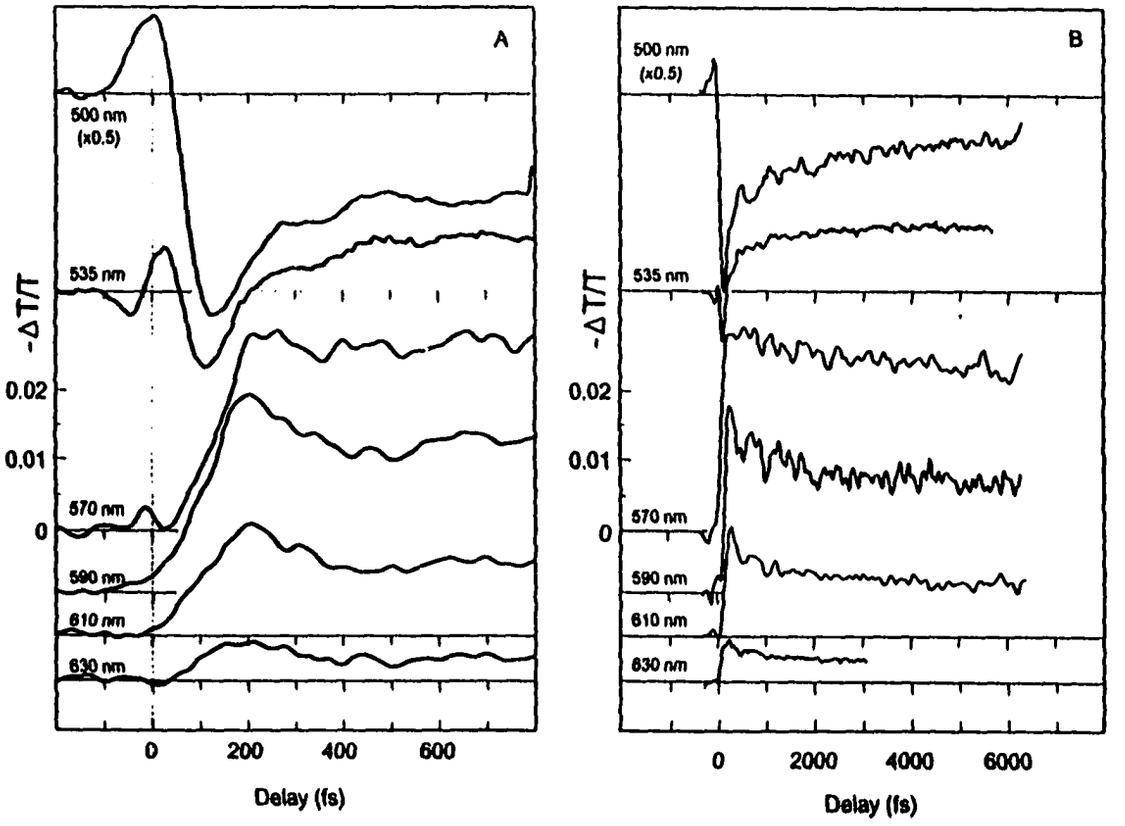


Fig. 4.7 Transient absorption measurements of rhodopsin at various probe wavelengths (10-fs probe) after excitation by a 35-fs pump pulse at 500 nm. (A) Measurements recorded from 0 to 700 fs. (B) Measurements recorded from 0 to 6 ps. The highest signal/noise measurement at 630 nm was recorded only to 3 ps. The 500-nm measurements have been divided by 2 for ease of display.

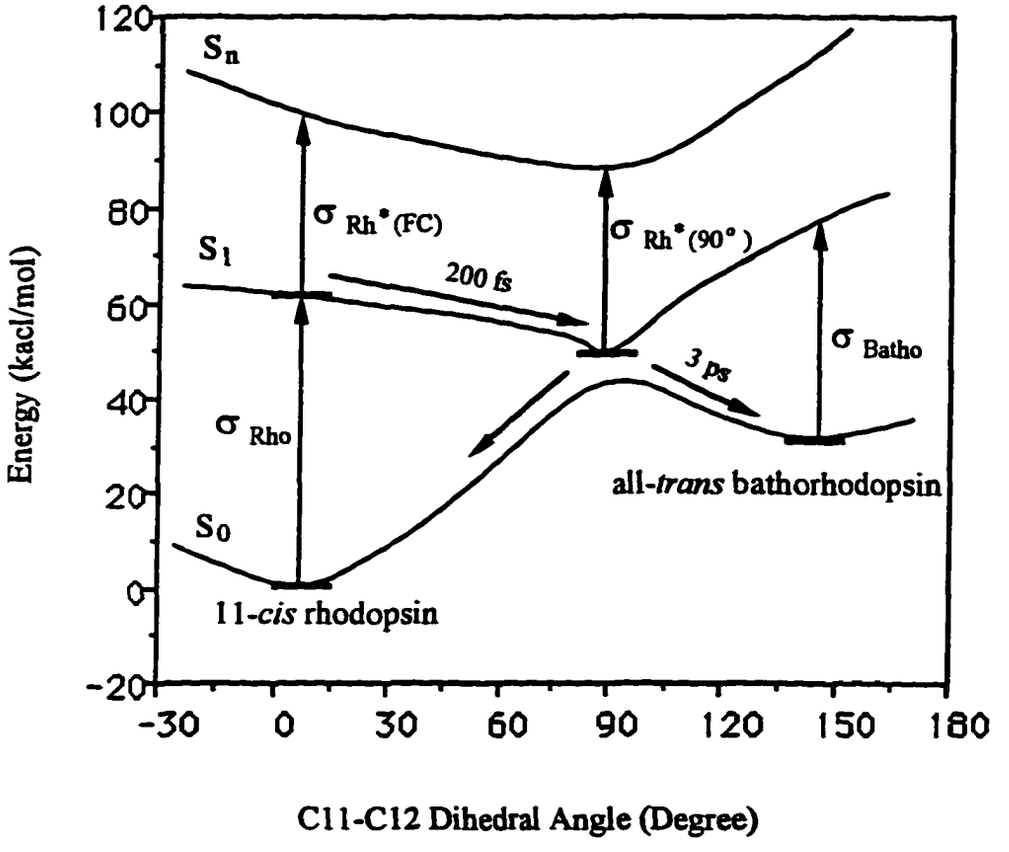


Fig. 4.8 Model I for the first step of vision described by the schematic potential surfaces for the *cis-trans* isomerization. A metastable state twisted at 90 degree forms in 200 fs and it takes 3 ps to complete the isomerization to form bathorhodopsin and repopulate the ground state of rhodopsin.

Furthermore, this experiment also provides the first direct evidence that the exchange of rhodopsin's exchangeable protons for deuterons does not affect the observed dynamics. Therefore, in a physiological environment, the primary event of vision is not photon translocation but a *cis-trans* isomerization. This conclusion is also supported by a femtosecond transient absorption experiment on the visual pigment anolog isorhodopsin[36].

Model II[34] is based on the experiment shown in Fig. 4.7. When exciting rhodopsin by a pump pulse at 500 nm, both induced absorption and bleaching were observed as time proceeds. At 500 nm, an instantaneous induced absorption increment, that is present for less than 100 fs rapidly disappears and a bleaching with a 3 ps recovery time are observed. At 570 nm, there is a rapidly developing induced absorption which reaches a maximum by 200 fs. After 200 fs, there is a longer time scale change in absorption(~3 ps). The result at 610 nm is similar to that of the experiment of Model I at 620 nm. The results for 570 nm and 620 nm show a 100 fs delay in the appearance of induced absorption. The time resolution of this experiment is less than 40 fs. The authors thus provide a paradigm (Fig. 4.9):

$$\text{Rh(11-}cis\text{)} \xrightarrow{h\nu} \text{Rh*(FC)} \xrightarrow{t=200\ \text{fs and curve crossing}} \text{All-}trans \text{ Photo- or Batho- rhodopsin}$$

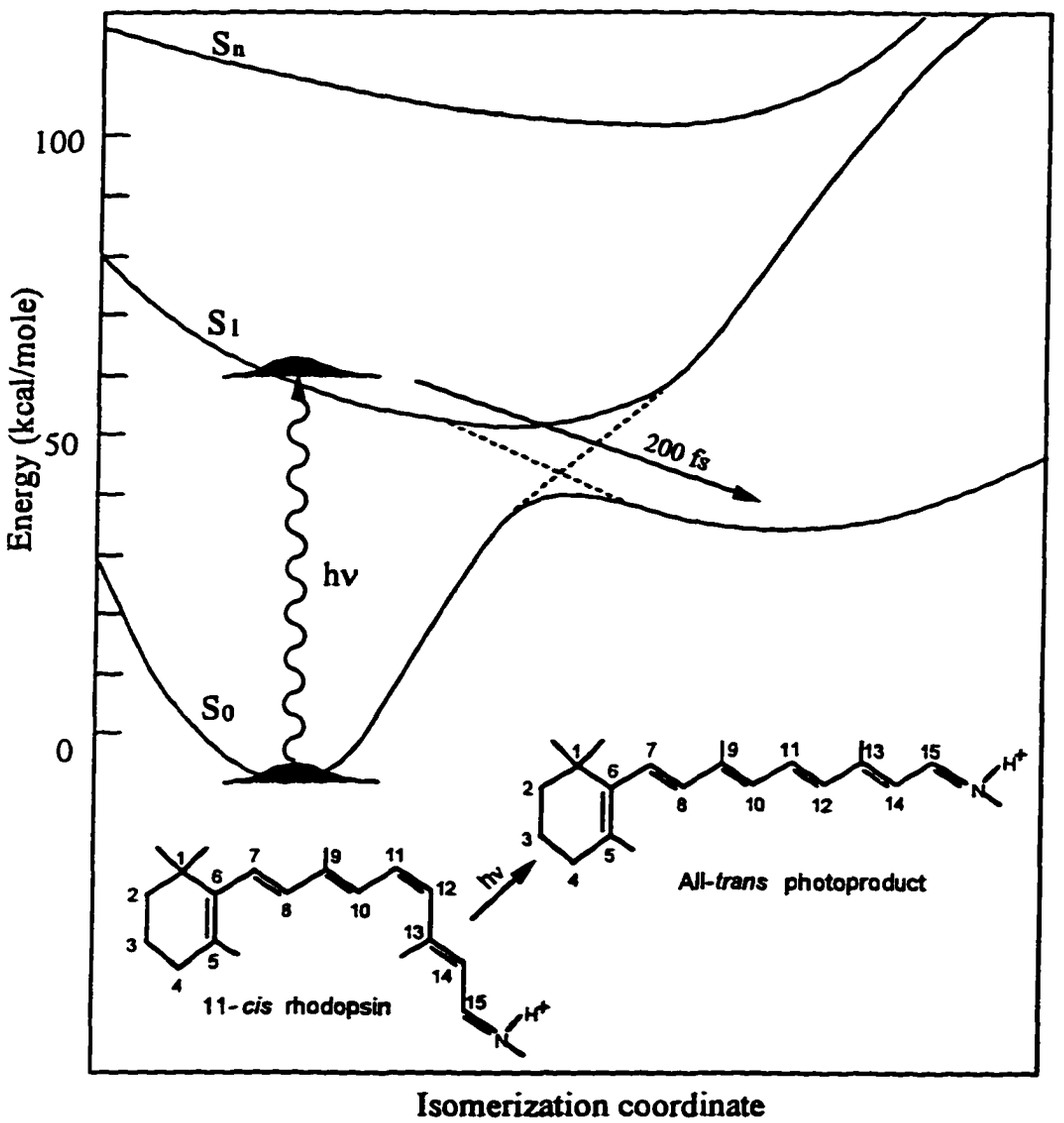


Fig. 4.9 Model II for the schematic ground-state and excited-state potential energy surfaces for the 11-*cis* to all-*trans* isomerization in rhodopsin. The reaction path of the photoisomerization is indicated by the nonadiabatic surfaces (dashed lines). From R. W. Schoelein et al. Science 254, 412(1991).

Because of the short time appearance of induced absorption at 500 nm and the 100 fs delay of induced absorption at longer wavelengths of 570 nm and 610 nm, the authors interpreted that the excited rhodopsin wave packet rolls out of the Frank-Condon region very rapidly, in less than 100 fs. Since the induced absorption reaches a maximum for the photoproduct peak at 570 nm in 200 fs, the excited rhodopsin isomerizes to an all-*trans* ground state product in a total time of 200 fs. The all-*trans* photoproduct was first assigned to photorhodopsin[34] with a maximum change of absorption at 570 nm, which decays to bathorhodopsin in about ~40 ps. Later, it was reassigned to bathorhodopsin[37]. The ~3 ps bleaching recovery at 500 nm and ~3 ps decay of induced absorption at longer wavelengths(e.g. 570 nm and 610 nm) are interpreted as vibrational cooling of the reactant and the photoproduct.

A picosecond transient absorption experiment[38] by a separate group shows a single 5 ± 1 ps time constant up to a 500 ps time delay with 5 ps time resolution at 623 nm and 595 nm. Thus the all-*trans* photoproduct in Model II should be bathorhodopsin.

In this thesis, I will discuss the results of a novel three beam pump-probe experiment using a new 11-*cis* to all-*trans* isomerization scheme, which resolved the controversies between the above two models.

## 4.4) Theoretical Models and Simulations

Various models have been proposed and many simulations have been performed for the primary event of vision[27-32, 39-44]. Birge *et al.* have performed a series of theoretical investigations of the primary event of the visual process using a semiempirical molecular

dynamics formalism[28-32]. The ground-state and excited-state surfaces connecting rhodopsin and bathorhodopsin along the C11=C12 dihedral reaction path were partially mapped on the basis of a revised model of the protein binding site with a counterion interacting with the C13 ~ C15 region of the chromophore. The ground-state surface was generated by using MINDO/AMI procedures, and the excited-state surface was generated by using INDO-PSDCI procedures including both single- and double-configuration interactions. The first excited state exhibits a barrierless reaction path for the C11=C12 dihedral torsion with a local minimum(activated complex) centered at $90^0$ as shown in Fig. 4.10. Semiempirical molecular dynamics procedures are used to simulate the forward and reverse photochemistry. The activated complex is reached in 375 fs following excitation(Figs. 4.11 and 4.12). The quantum yields($\Phi$) and product formation time($\tau$) are calculated on the basis of semiclassical coupling models. Best results are obtained by including both dynamic and phased nonadiabatic coupling(experimental value): $\Phi_{R\rightarrow B}$=0.698(0.67); $\tau_{R\rightarrow B}$=1.36(~3)ps; $\Phi_{B\rightarrow R}$=0.521(0.53); $\tau_{R\rightarrow B}$=1.628(~3)ps.

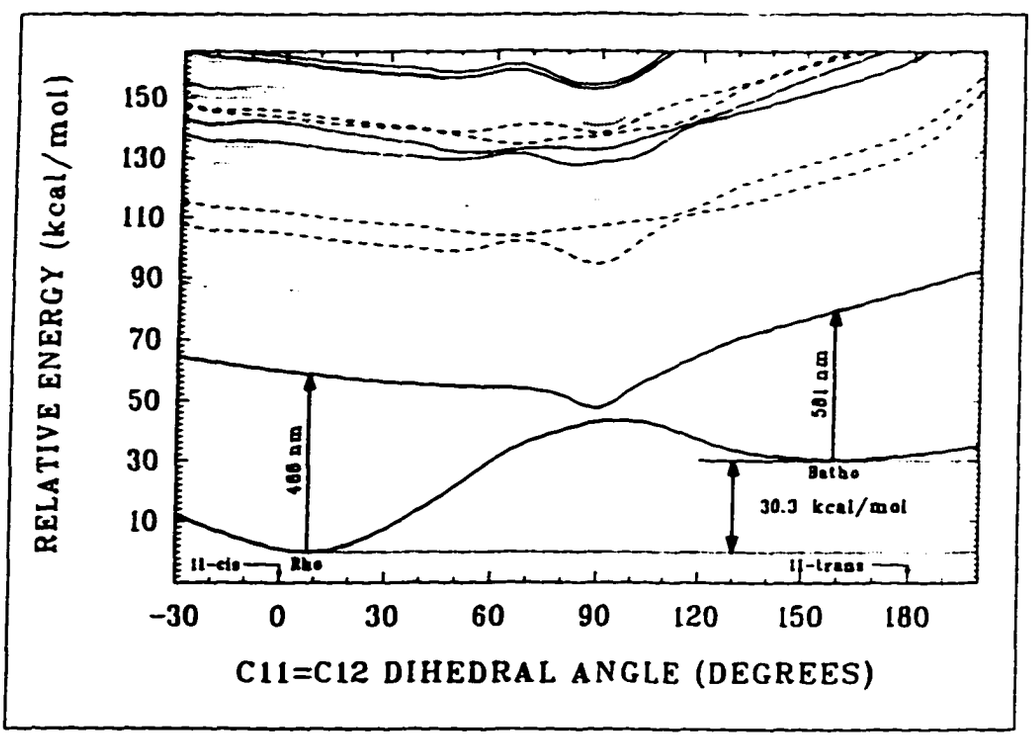


**Fig. 4.10 Ground and lowest seventeen excited singlet state potential surfaces as a function of the C11=C12 dihedral angle. The dotted line represents the oscillator strengths of $S_n$<-$S_1$ less than 0.1, and the dashed line for oscillator strengths greater than 0.1.**

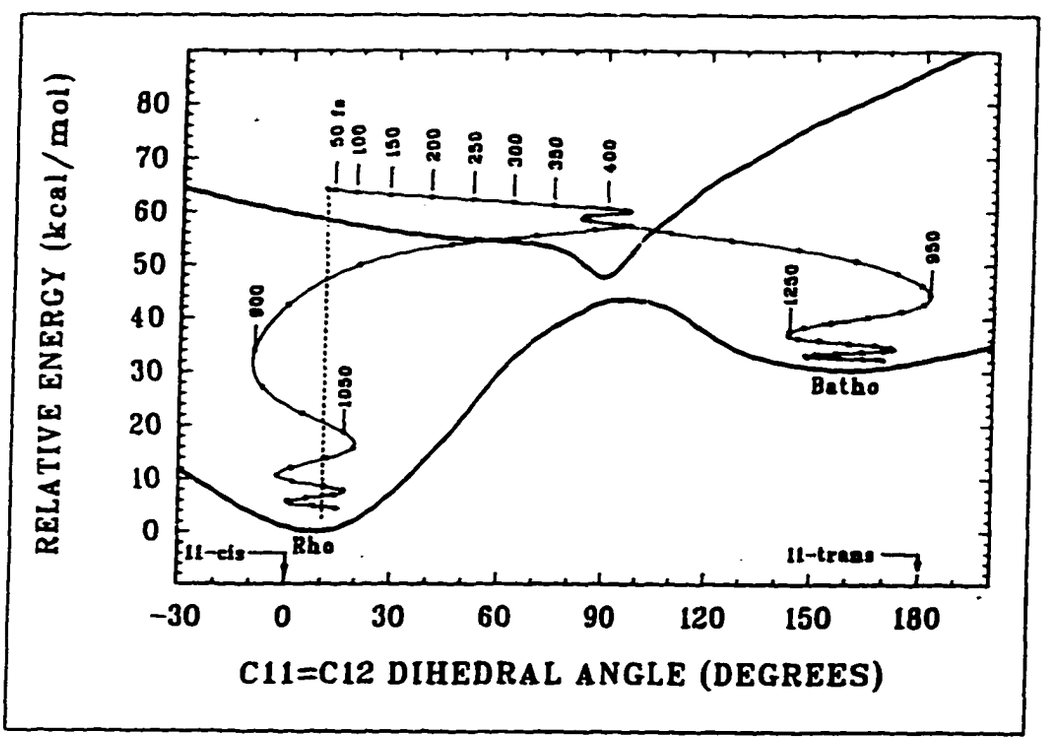


Fig. 4.11 Molecular dynamics of the rhodopsin(Rho)->bathorhodopsin(Batho) photochemical transformation based on the ground and first excited singlet state potential energy surfaces. Each dot represents a time interval of 50 fs, and selected time increments relative to the initial excitation are labeled. The excited state species enters the activated complex (the excited-state potential well with a minimum energy near 90°) in ~375 fs.

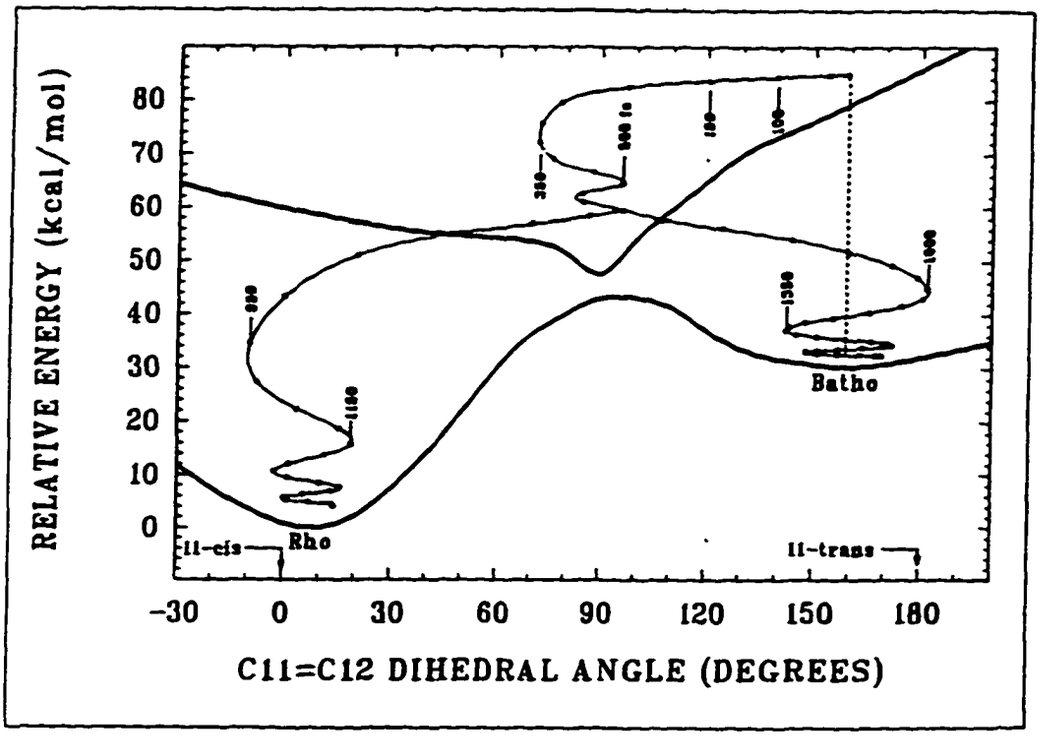


Fig. 4.12 Molecular dynamics of the bathorhodopsin(Batho)->rhodopsin(Rho) photochemical transformation based on the ground and first excited singlet state potential energy surfaces. Each dot represents a time interval of 50 fs, and selected time increments relative to the initial excitation are labeled. The excited state species enters the activated complex (the excited-state potential well with a minimum energy near 90°) in ~210 fs.

## References


1. Toru Yoshizawa and George Wald *Nature* **197**, 1279(1963)

2. George Wald *Nature* **219**, 800(1968)

3. George Wald *Science* **162**, 230(1968)

4. A. R. Oseroff and R. H. Callender *Biochemistry* **13**, 4243(1974)

5. G.Eyring and R. Mathies *Proc. Natl. Acad. Sci. (USA)* **76**, 33(1979)

6. B. Aton, A. G. Doukas, D. Narva, R. H. Callender, U. Dinur and B. Honig *Biophys. J.* **29**, 79(1980)

7. B. Aton, R. H. Callender and B. Honig *Nature* **273**, 784(1978)

8. R. A. Mathies, S. O. Smith and I. Palings in *Biological Applications Of Raman Spectroscopy ch2* ed. by T. G. Spiro, John Wiley & Sons, Inc., New York(1987)

9. R. H. Callender, A. Doukas, R. Crouch, and K. Nakanishi *Biochemistry* **15**, 1621(1976)

10. I. Paling, J. A. Pardoen, E. van den Berg, C. Winkel, J. Lugtenberg and R. Mathies *Biochemistry* **26**, 2545(1987)

11. G. Eyring, B. Curry, R. Mathies, R. Fransen, I. Paling and J. Lugtenberg *Biochemistry* **19**, 2410(1980)

12. G. Eyring, B. Curry, A. Broek, J. Lugtenberg and R. Mathies *Biochemistry* **21**, 384(1982)

13. G. R. Loppnow and R. A. Matehies *Biophys. J.* **54**, 35(1988)

14. G. Hayward, W. Carlsen, A. Siegman and L. Stryer *Science* **211**, 942(1981)

15. A. G. Doukas, P. Y. Lu and R. R. Alfano *Biophys. J.* **35**, 547(1981)

16. A. G. Doukas, M. R. Junnarkar, R. R. Alfano, R. H. Callender, T. Kakitani and B. Honig *Proc. Natl. Acad. Sci. (USA)* **81**, 4790(1984)

17. J. Buchert, V. Stefancic, A. G. Doukas, R. R. Alfano, R. H. Callender, J. Pande, H. Akita, V. Balogh-Nair and K. Nakanishi *Biophys. J.* **43**, 279(1983)

18. A. G. Doukas, M. R. Junnarkar, R. R. Alfano, R. H. Callender and V. Balogh-Nair *Biophys. J.* **47**, 795(1985)

19. K. Peters, M. L. Applebury and P. M. Rentzepis *Proc. Natl. Acad. Sci. (USA)* **74**, 3119(1977)

20. A. G. Doukas, R. H. Callender and R. R. Alfano *Applications of Fluorescence in the Biomedical Sciences*, pages 69-89, Alan R. Liss, Inc.(1986)

21. G. E. Busch, M. L. Applebury, A. A. Lamola and P. M. Rentsepis *Proc. Natl. Acad. Sci. (USA)* **69**, 2802(1972)

22. B. H. Green, T. G. Monger, R. R. Alfano, B. Aton and R. H. Callender *Nature(london)* **269**, 179(1977)

23. T. G. Monger, R. R. Alfano and R. H. Callender *Biophys. J.* **27**, 105(1979)

24. A. G. Doukas, V. Stefancic, T. Suzuki, R. H. Callender and R. R. Alfano *Photobiochem. Photobiophys.* **1**, 305(1980)

25. Y. Shichida, S. Matuoka and T. Yoshizawa *Photobiochem. Photobiophys.* **7**, 221(1984)

26. H. Kandori, S. Matuoka, Y. Shichida and T. Yoshizawa *Photochem. Photobiol.* **49**, 181(1989)

27. A. Warshel *Nature* **260**, 679(1976)

28. R. R. Birge and L. M. Hubbard *J. Am. Chem. Soc.* **102**, 2195(1980)

29. R. R. Birge and L. M. Hubbard *Biophys. J.* **34**, 517(1981)

30. R. R. Birge, C. M. Einterz, H. M. Knapp and L. P. Murry *Biophys. J.* **53**, 367(1988)

31. R. R. Birge *Biochim. Biophys. Acta.* **1016**, 293(1990)

32. J. R. Tallent, E. W. Hyde, L. A. Findsen, G. C. Fox and R. R. Birge *J. Am. Chem. Soc.* **114**, 1581(1992)

33. M. Yan, D. Manor, G. Weng, H. Chao, L. Rothberg, T. M. Jedju, R. R. Alfano and R. H. Callender *Proc. Natl. Acad. Sci. (USA)* **88**, 9809(1991)

34. R. W. Schoenlein, L. A. Peteanu, R. A. Mathies and C. V. Shank *Science* **254**, 412(1991)

35. M. Yan, D. Manor, R. R. Alfano, R. H. Callender and L. Rothberg *Proc. Of the International Conference on Lasers '92, Dec. 7-10,* (1992)

36. R. W. Schoenlein, L. A. Peteanu, Q. Wang, R. A. Mathies and C. V. Shank *J. Phys. Chem.* **97**, 12087(1993)

37. Q. Wang, R. W. Schoenlein, L. A. Peteanu, R. A. Mathies and C. V. Shank *Science* **266**, 422(1994)

38. A. Popp, L. Ujj and G. H. Atkinson *J. Phys. Chem.* **99**, 10043(1995)

39. A. Warshel *Proc. Natl. Acad. Sci. (USA)* **75**, 2558(1978)

40. R. M. Weiss and A. Warshel *J. Am. Chem. Soc.* **101**, 6131(1979)

41. T. Rosenfeld, B. Honig and M. Ottolenghi *Pure & Appl. Chem.* **49**, 341(1977)

42. K van der Meer, J. J. C. Mulder and J. Lugtenberg *Photochem. And Photobio.* **24**, 363(1976)

43. A. Lewis *Proc. Natl. Acad. Sci. (USA)* **75**, 549(1978)

44. J. Favrot, J. M. Leclercq, R. Roberge, C. Sandorfy and D. Vocelle *Photochem. And Photobio.* **29**, 99(1979)

# Chapter 5

# Research on Primary Events in Vision

Resonance Raman, fluorescence kinetics and transient absorption spectroscopy as well as theoretical studies have firmly established that the primary event in the visual process is the rapid isomerization of the 11-*cis* chromophore of rhodopsin to the all-*trans* configuration of bathorhodopsin. Many important questions remain open in describing this process. Comparing Model I and Model II in the previous chapter, one may notice the following disagreements: First, whether the bathorhodopsin formation time is 3 ps or 200 fs; Second, whether the 3 ps bleaching recovery of rhodopsin at 500 nm is due to the 3 ps lifetime of the 90° excited state or due to the vibrational relaxation of the unrelaxed ground state rhodopsin after curve crossing; Third, whether the 3 ps component of the photoinduced absorption observed in the spectral region near where bathorhodopsin absorbs is due to hot ground state bathorhodopsin cooling or excited state absorption.

To address these controversial issues of how the conformational change from rhodopsin(11-*cis*) to bathorhodopsin(All-*trans*) occurs and how fast it is, a modified pump-probe transient measurement was performed, which resolves the above controversies and provides a complete picture of the primary process in vision chemistry.

## 5.1) Sample Preparation

The rhodopsin sample was prepared from commercially available dark-adapted frozen bovine retinas(purchased from Lawson). The rod outer segments were isolated by the sucrose gradient method. Samples were washed with 10 mM HEPES in water and then solubilized in 20 mM n-dodecylmatoside, 0.1 M hydroxylamine, 10 mM HEPES, buffered to pH 7.0. The sample was kept in the dark and circulated from an ice-chilled reservoir through a 2mm pathlength cuvette by a peristaltic pump at a flow rate fast enough to replenish the excitation region between laser pulses. The sample had an optical density (OD) of about 3 at 500 nm.

## 5.2) Experiment Design

The low temperature experiments show that bathorhodopsin can be isomerized to reform rhodopsin with a significant quantum yield($\phi \sim 0.5$). Thus, if the bathorhodopsin is formed by photoexcitation of rhodopsin at physiological temperature, a delayed second pump pulse with its wavelength at the bathorhodopsin absorption band would drive some of the bathorhodopsin back to rhodopsin. A subsequent probe beam could measure how much bathorhodopsin had been depleted by the second pump as a function of delay between the two pumps. This would address: First, how quickly bathorhodopsin is actually formed, since one would be able to deplete it as soon as it is formed; Second, whether the absorption is all due to bathorhodopsin; presumably, excited state absorption as suggested by model I would have little effect on the net amount of bathorhodopsin produced.

The experimental setup and timing are described in section 2.5.2. The first pump with a 500 nm wavelength is used to excite rhodopsin to initialize the photochemical reaction. The second pump of wavelength 620 nm which is in the absorption band of bathorhodopsin could be time delayed with respect to the first pump pulse and is used to drive a portion of bathorhodopsin back to rhodopsin. Both pumps have an excitation intensity in the order of $0.5x10^{15}$ photons/cm$^2$, which is within the range of the linear intensity dependence of photon induced absorption. The third pulse of wavelength 590 nm and a fixed longer time delay (5 ps or more) with respect to the first pump is to probe the bathorhodopsin formation yield change. If the second pump pulse is delayed longer than the bathorhodopsin formation time, the bathorhodopsin would be re-excited into its excited state(S1) by the second pump pulse. Presumably, the common excited state would relax into bathorhodopsin and the rhodopsin ground state. Therefore, the formation yield of bathorhodopsin would be changed via the second excitation pulse and could be probed by a third pulse. On the other hand, if the second pulse exciting the sample precedes the formation of bathorhodopsin, the rhodopsin molecules in the excited state (e.g. $90^o$ state) would be excited into higher levels and relax back into the common excited state of rhodopsin, which would not change the formation yield of bathorhodopsin.

## 5.3) Results and Discussion

The experimental results are shown in Fig 5.1. The three-beam data is represented as a thick line. The time delay shown in the figure is the second pump relative to the first pump. Since there is no absorption at 620 nm for rhodopsin, there is no effect of the 620

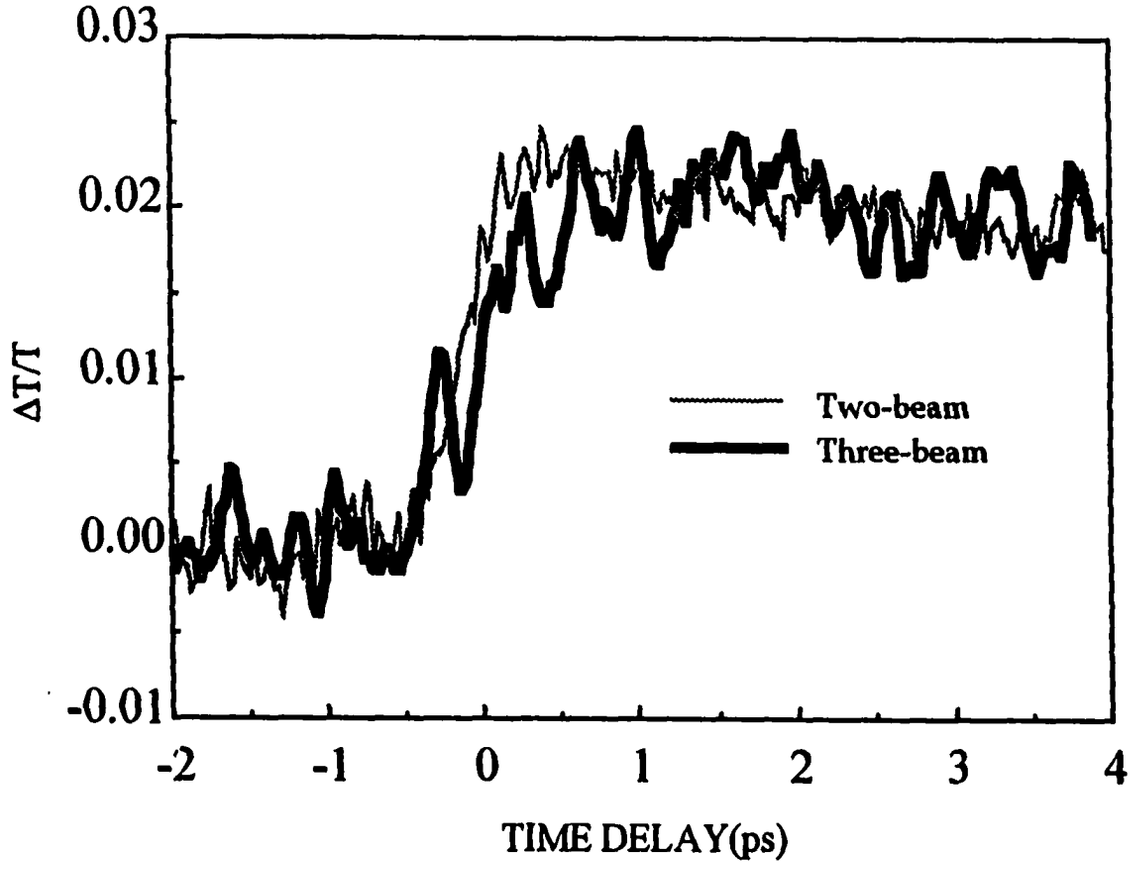


Fig. 5.1 The thick line is the transmission change of the rhodopsin sample at a probe wavelength of 590 nm in the three-beam experiment. The first pump is at 500 nm and the second pump is at 620 nm. The time delay is the second pump relative to the first pump. The probe is fixed at 5 ps relative to the first pump. The thin line is the induced absorption change from the two-beam conventional pump-probe experiment of rhodopsin.

nm pump at negative delay times. However, at positive delays we would expect an increment of transmission because part of the bathorhodopsin, which has greater absorption at 590 than rhodopsin, was driven back to rhodopsin by the 620 nm pump. The thin line in Fig 5.1 is the convolution of two pulses on the sample(500 nm pump with 590 nm probe) to show the systems time resolution.

From the above three-beam results we find: (1) Bathorhodopsin can be isomerized even at physiological temperature. To our knowledge, this is the first time it has been demonstrated. (2) Bathorhodopsin formation is very prompt as described by Model II. The convolution of pump and probe laser pulses is about 400 fs while the three-beam experiment gives rise time of about 600 fs. The fast rise time (~ 600 fs) of our three-beam measurement indicates that ground state formation is on the order of 200 fs. This conclusion is based on the argument that the bathorhodopsin population must already have formed on this time scale since it can be depleted by the second pump. This rules out the 3 ps delay in bathorhodopsin formation suggested by model I. (3) The 3 ps component presented in the two-beam measurement(Fig. 5.2, 500 nm pump, 620 nm probe) is absent in the three-beam experiment. Therefore it is strongly suggested that the 3 ps component is not due to bathorhodopsin but to the excited state, probably the 90° state as proposed in Model I. The presence of such an excited state would also explain the 3 ps bleaching recovery of the rhodopsin ground state, since one third of the excited rhodopsins would relax to the ground state rhodopsin in ~3 ps. Thus, the 3 ps component in absorption and bleaching recovery comes from the same origin, namely, of the excited state as described in Model I, which is difficult to rationalize in the picture of Model II.

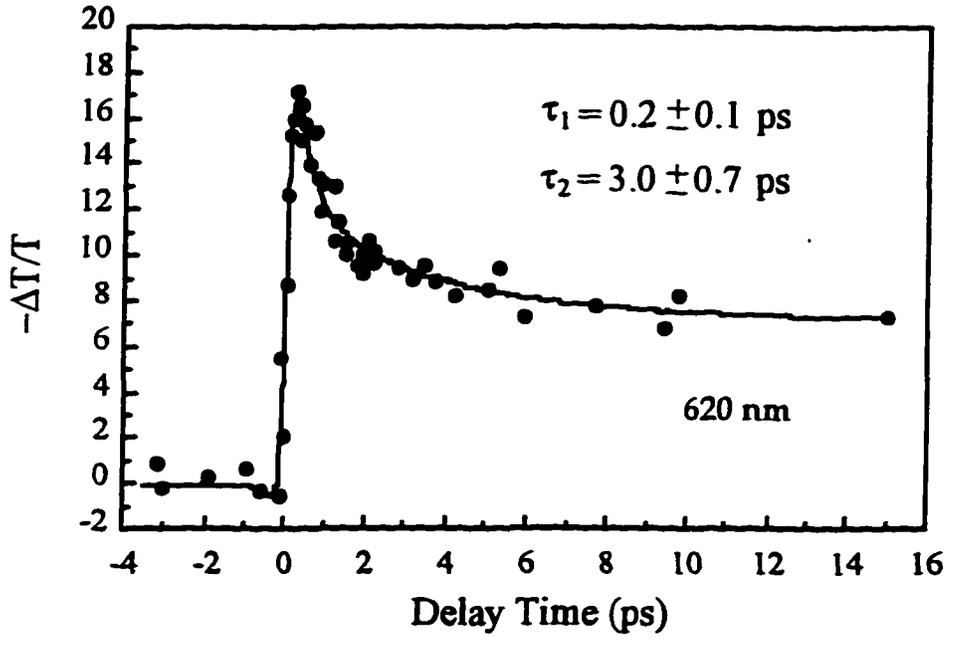


**Fig. 5.2 Absorption changes at 620 nm induced by a 500 nm pump pulse as a function of pump-probe delay time. The time resolution is approximately 300 fs. The dots are experimental data and the solid lines are theoretical fittings.**

A similar experiment performed at Bell labs[1] by our collaborators is in agreement with the results here (Fig. 5.3). In Bell lab's version of the experiment, The first pump, second pump and the probe are at 500 nm, 605 nm and 570 nm, respectively, with the probe pulse set at ~ 1 ns.

The molecular simulations of the primary event in rhodopsin[2-5] yield the results that the first excited state minimum is at the ~90° torsional coordinate and the bathorhodopsin is formed in about 1 ps.

Based on this experiment and the one done in Bell Labs, the coherent wavepacket calculations by Tallent *et al*[2], and the latest experimental observation of the vibrationally coherent photochemistry of the primary event of vision[6], Rothberg[1] proposed a refined model(Fig 5.4) which takes into account the merit of Model I and Model II. Two thirds of the excited state rhodopsin molecules isomerize promptly via a curve crossing to form bathorhodopsin in ~ 200 fs and retains coherence in its final state. One third, which missed the curve crossing, will remain in the excited state and never isomerize. This excited state, probably the one with the equilibrium position twisted 90° around the 11-*cis* retinal double bond, relaxes in ~3 ps to reform the rhodopsin ground state, explaining the delayed recovery of the bleaching signal and the difference between the two-beam and three-beam transient absorption experiments.

In conclusion, this 3-beam experiment has resolved the controversial issues of how the conformational change from rhodopsin(11-*cis*) to bathorhodopsin(All-*trans*) occurs and how fast it is by directly measuring the ground state species formation dynamics. It provides a complete picture of the primary event in vision. The *cis* - *trans*

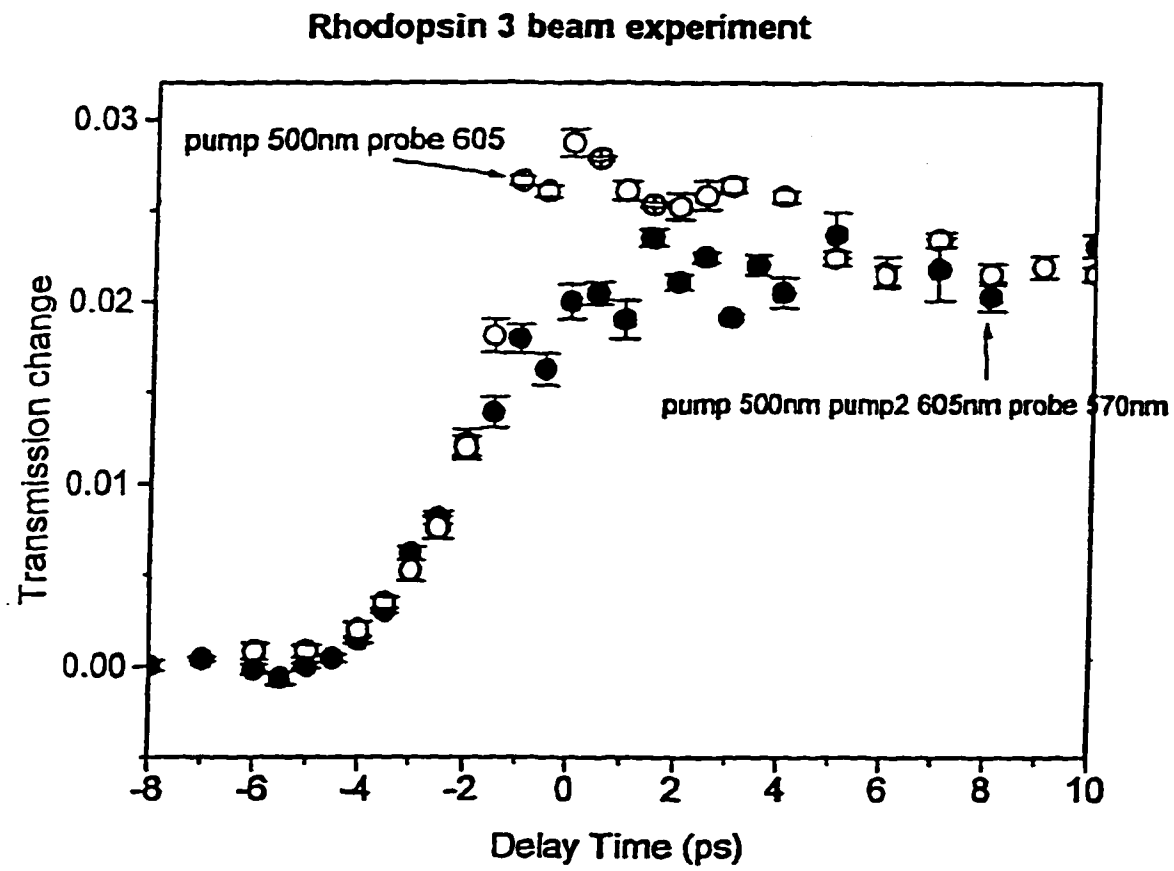


Fig. 5.3 Bell Lab's experimental data. The first pump, second pump and the probe are at 500, 605 and 570 nm, respectively, with the probe pulse set at ~ 1 ns.

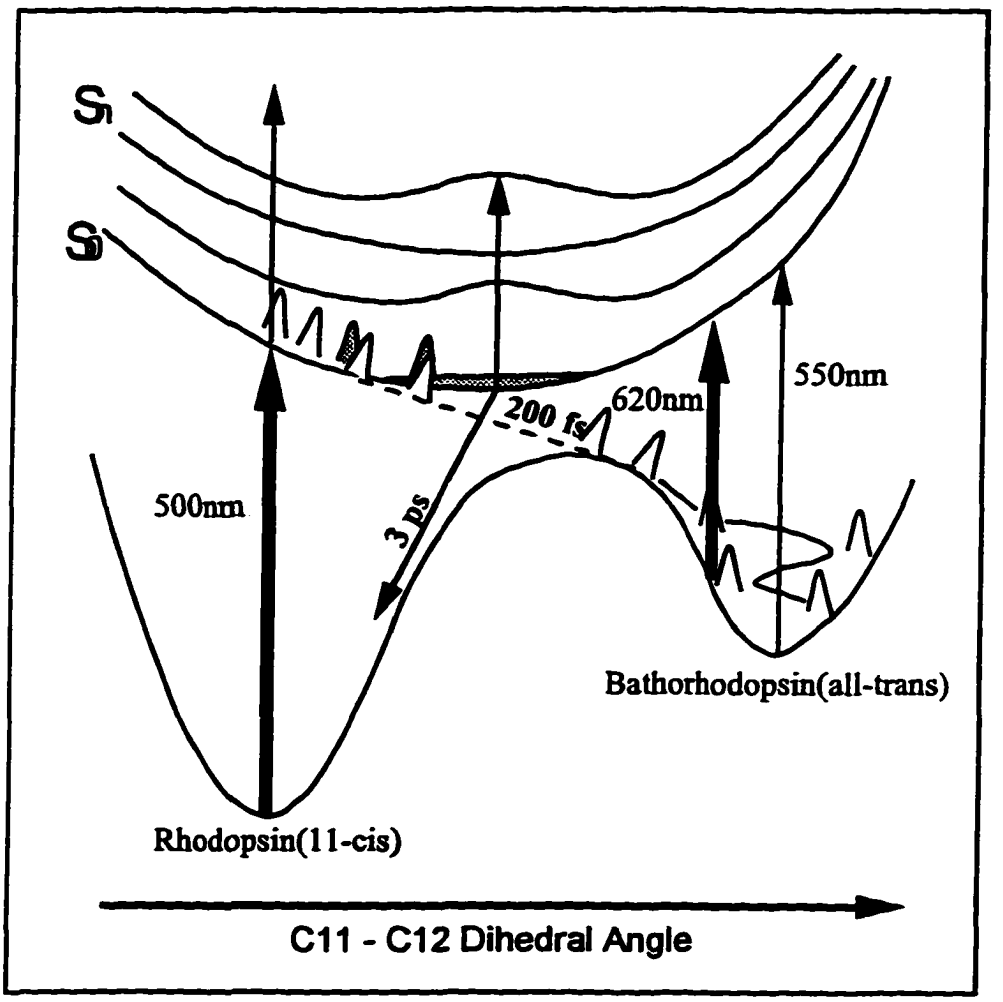


Fig. 5.4 The model of the primary event of vision which takes into account of the results of the two-beam experiments and the most recent three-beam experiments.

isomerization of the visual pigment rhodopsin is very fast and the bathorhodopsin is formed in only ~200 fs after photoexcitation of rhodopsin at physiological temperature. However, it takes about 3 ps for the unisomerized excited rhodopsin to relax to the ground state rhodopsin. The three-beam pump-probe measurement is a very important technical advance in the characterization of transient species in the initial step of vision. Within our experiment, we could drive the bathorhodopsin back into rhodopsin with a second photoexcitation. We believe this is the first experimental evidence of the *trans* to *cis* formation of rhodopsin at physiological temperature.

## References


1. M. Yan and L. Rothberg *Private communication*

2. J. R. Tallent, E. W. Hyde, L. A. Findsen, G. C. Fox and R. R. Birge *J. Am. Chem. Soc.* **114**, 1581(1992)

3. R. R. Birge *Annu. Rev. Phys. Chem.* **41**, 683(1990)

4. R. R. Birge and L. M. Hubbard *Biophys. J.* **34**, 517(1981)

5. R. R. Birge and L. M. Hubbard *J. Am. Chem. Soc.* **102**, 2195(1980)

6. Q. Wang, R. W. Schoenlein, L. A. Peteanu, R. A. Mathies and C. V. Shank *Science* **266**, 422(1994)

# Chapter 6

# Persistent Hole Burning Optical Storage

This chapter presents the basic concepts of persistent hole burning. It describes two approaches of optical storage using persistent hole burning: the frequency- and time-domain optical storage. It also explains the hole burning mechanism of OEP/PS used in this thesis research.

## 6.1) Persistent Hole Burning

Persistent hole burning(PHB) was discovered in 1974 by two soviet research groups [1-2]. It relies on some fundamental properties of zero-phonon lines in the optical spectrum of atoms and molecules introduced as impurities in solid matrices. For an individual impurity, the absorption spectrum consists of a zero-phonon line(pure electronic transition) and a phonon side-band(Fig. 6.1a). In a perfect lattice, impurity molecules are in identical environments and therefore have an identical transition frequency and only homogeneous broadening($\Gamma_H$) occurs in the absorption spectrum(Fig. 6.1b). This homogeneous broadening is caused by the dynamic influence of lattice thermal fluctuations on the impurity molecules. In contrast to the situation in the perfect lattice above, for guest molecules in a structural disordered system with defects and strains like polymer matrices, each of them will have a slightly different surroundings and thus the different transition frequencies which lead to the inhomogeneous broadening($\Gamma_I$)

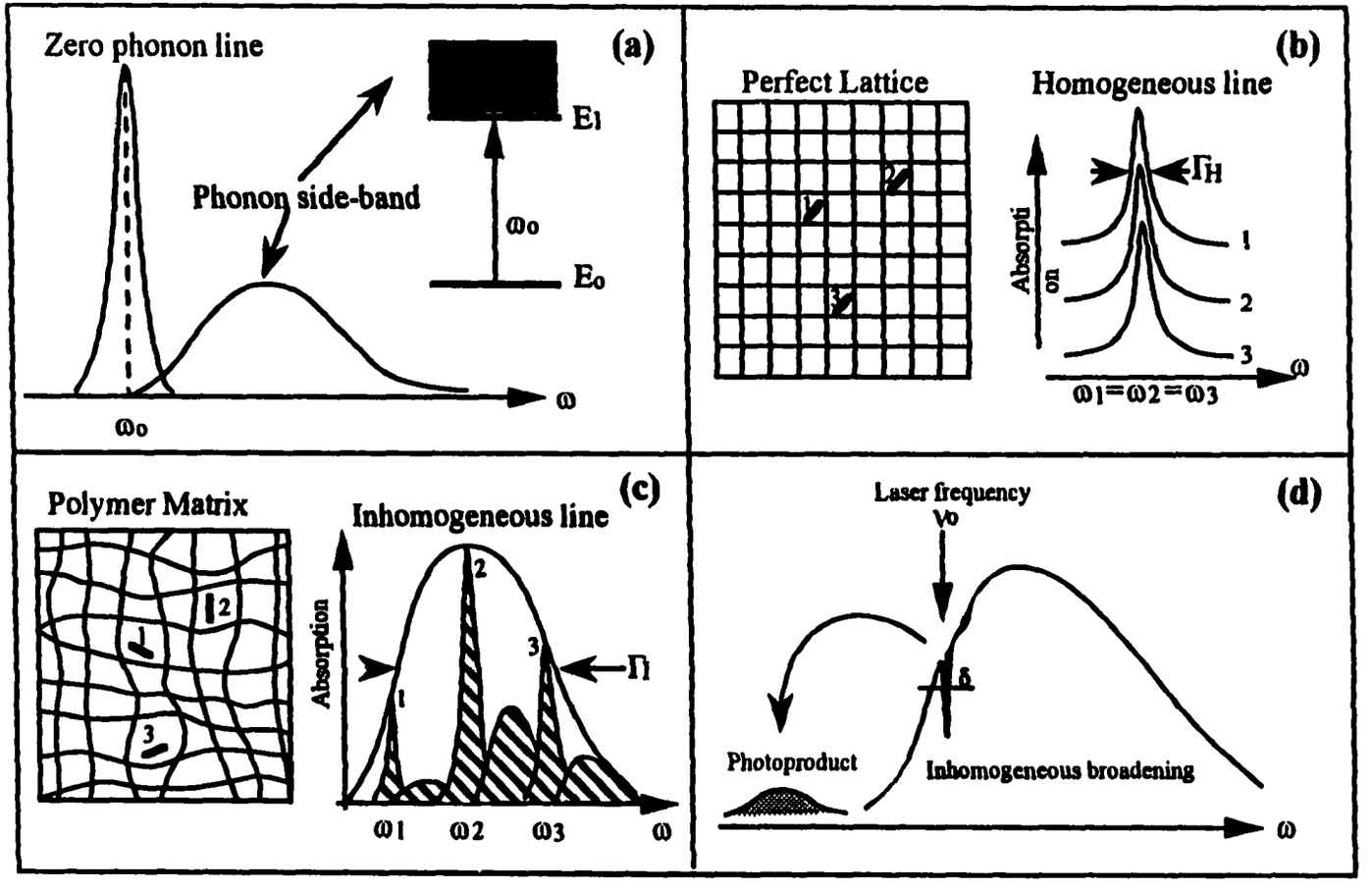


Fig. 6.1 (a) Individual impurity absorption spectrum consists of zero-phonon line and phonon side band. (b) Impurity absorption spectra in perfect lattice, only having the homogeneous broadening. (c) Inhomogeneous broadening for the impurities in polymer matrix. (d) Spectral hole burning phenomena.

as shown in Fig. 6.1c. A spectral line shape is determined by both homogeneous broadening and inhomogeneous broadening. At low temperatures the impurity absorption band is dominated by inhomogeneous broadening consisting of fractional homogeneous spectra. For impurities in a polymer matrix at liquid helium temperature, the inhomogeneous width is $\Gamma_I = 100 - 500\ cm^{-1}$ and the homogeneous width is $\Gamma_H = 10^{-3} - 10^{-1}\ cm^{-1}$. When such a sample is irradiated with the monochromatic light frequency $\nu_0$ within an absorption band, only a small fraction $\approx \Gamma_H / \Gamma_I$ of the impurities in the narrow spectral region $\nu_0 \pm \Gamma_H$ is excited. These molecules can undergo phototransformations(e.g. a transition to another electronic state or a photochemical reaction) such that the photoproduct absorbs at a different frequency $\nu \neq \nu_0$. A narrow spectral hole with width $\delta \approx 2\ \Gamma_H$ is created in the original absorption band(Fig. 6.1d). The hole lifetime is determined by the lifetime of the photoproduct and in many cases at low temperatures it becomes hours, days and even practically infinite. Such a process is called persistent hole burning(PHB).

There is a well defined relationship between the homogeneous line width $\Gamma_H$ and the optical dephasing time $T_2$. The physical picture is that if the line width is broader, the phonon scattering is stronger, which leads to a shorter depasing time. The optical dephasing time $T_2$ includes two parts:

$$1/T_2 = 1/T_1 + 2/T_2^* \qquad (6.1)$$

where $T_1$ is the life time of the excited state and $T_2^*$ is the pure dephasing time. This additional decay of $T_2^*$ is caused by the thermal motion(phonon scattering) of the host. If the whole ensemble of molecules is excited with a coherent light source, the molecules

will oscillate in phase with each other and with the external light source. In this way, a macroscopic polarization **P** is induced which can be expressed as a vector sum of all the molecular transition dipole moments

$$\mathbf{P} = \mathbf{P}_0 \exp\{i[E_1 - E_0]/h]t\}; \qquad \mathbf{P} = \langle \mu_{10}(t) \rangle \tag{6.2}$$

Equation (6.2) describes a complex vector rotating with the laser frequency

$$\omega_L = [E_1 - E_0]/h \tag{6.3}$$

If an individual molecule of the large ensemble is considered, thermal motion in its neighborhood will change its energy from $E_0$ to $E_0 + \Delta E_0$ and from $E_1$ to $E_1 + \Delta E_1$. As a consequence, the characteristic frequency of the transition moment is shifted by the amount $\varepsilon = (\Delta E_0 - \Delta E_1)/h$. This "detuning" leads to a phase loss of the molecule. Since the thermal motions of the host surroundings have a stochastic nature, $\varepsilon$ is also stochastic and thus leads, within the time interval $T_2^*$ to a stochastic distribution. During this time the various transition moments become out-of-phase and the macroscopic polarization drops to **P**/e.

Knowing $T_1$ and $T_2$, one can calculate the optical line width $\Gamma_H$ of a two level system

$$\Gamma_H = \frac{1}{T_2}\sqrt{1+\omega_1^2 T_1 T_2} \tag{6.4},$$

where $\omega_1$ is the Rabi frequency, proportional to the amplitude of the electric field vector of the light wave

$$\omega_1 = \mu_{10} E_0 / \hbar \tag{6.5}.$$

When the experiment is performed at low light intensity, then the following condition holds

$$\omega_1^2 \ll \frac{1}{T_1 \cdot T_2} \qquad (6.6).$$

Therefore

$$\Gamma_H = \frac{1}{T_2} \qquad (6.7).$$

$T_2$ is a key parameter in optical storage physics. It describes the interaction between the guest molecules and the host. $T_2$ is equivalent to the homogeneous line width of $\Gamma_H$ under condition (6.6). The inverse of the dephasing time $T_2^{-1}$ corresponds to a basic storage spectral element: bit. $T_2$ can be measured directly by two-pulse photon echo experiment(see Section 2.4). When the temperature T = 0 K, $T_2^* = \infty$ and $T_2 = T_1$.

## 6.2) Optical Storage

The PHB media[3-4] have been proposed for ultrahigh-density optical data storage because of their high spectral selectivity and long storage times. Two basic approaches have been proposed for writing and reading a stream of data bits: the frequency-domain[5-6] and time domain[7-8] optical storage.

### 6.2.1 Frequency-domain optical storage

In the frequency domain approach, a highly monochromatic light is employed to write and read data sequentially into frequency channels(Fig. 6.2) within the inhomogeneously broadened spectra. The upper limit for readout speed of a data bit is determined by the minimum width of a frequency channel or the homogeneous

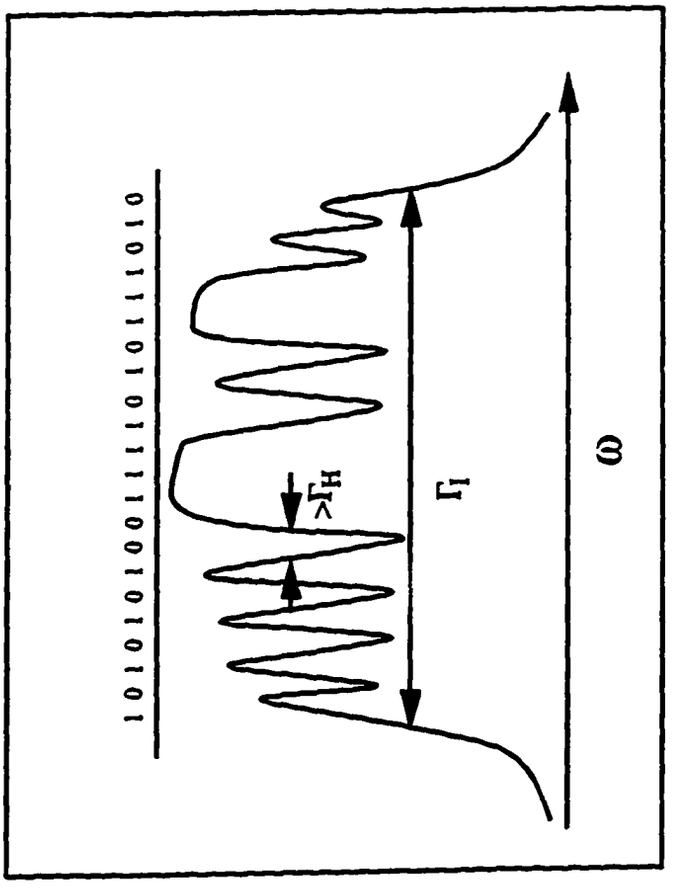


Fig. 6.2 Principle of frequency-domain optical storage on PHB materials.

linewidth(FWHM) $\Gamma_H$( laser line width $\Delta\nu < \Gamma_H$), typically 1 kHz to 1 GHz at liquid helium temperature.

### 6.2.2 Time-domain optical storage

The time-domain PHB optical storage is based on a special kind of photon echo called photon echo by accumulated grating described in Section 2.4. It utilizes the temporal interference between a reference pulse and a data pulse where information is encoded. These pulses modify the ground state population and their interference pattern is stored, like regular hole-burning, as a population grating in the frequency domain. To recall the data a read-out pulse must be applied, within the lifetime of the photoproduct. This pulse diffracts from the stored grating and reproduces the data in the form of a photon echo signal[9](Fig. 6.3). In time domain storage the frequency dimension is accessed in parallel by recording the Fourier spectrum of the data pulse. All the data bits are written and recalled in parallel by a spectrally broad laser pulse. In this case the readout speed is much higher than that in the frequency domain and is limited by the width of the inhomogeneous absorption band $\Gamma_I$ of the storage material, typically 10 GHz to 10 THz. Utilization of the highest possible speed requires femtosecond optical pulses. Ultimate recording density may be realized only for a very high speed of data pulse modulation $\Gamma_I^{-1}$ to cover the whole inhomogeneously broadened absorption band. The data pulse length must be less than the dephasing time $T_2 = \Gamma_H^{-1}$ to allow interference with the reference pulse.

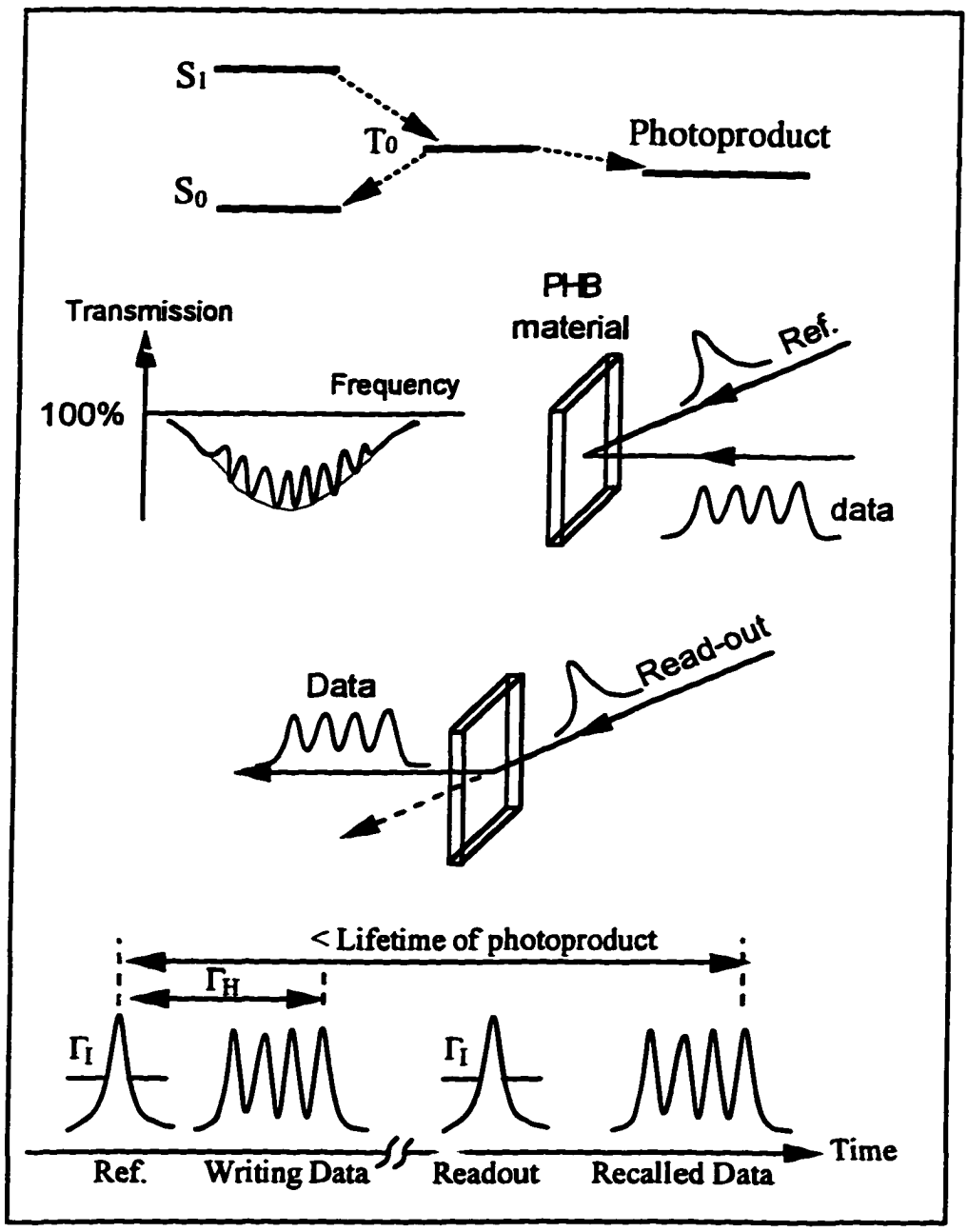


Fig. 6.3 Principle of time-domain PHB optical storage.

## 6.3) Persistent Hole Burning on OEP/PS

PHB material free-base octaethylporphine doped polystyrene(OEP/PS) was used in this thesis research(Fig. 6.4). Owing to the ring-like conjugated structure, an OEP molecule is fairly rigid and weakly interacts with host vibrations. Thus it has essentially a zero-phonon part in the $S_0$ -> $S_1$ absorption band, which make OEP/PS a good PHB material. The maximum of the pure electronic absorption band at low temperature appears at 619 nm, which ensures good overlap with the spectrum of the CPM laser and the amplifier( Fig. 6.5). The central hydrogens of OEP play a key role in the persistent spectral hole burning. In the stable molecular conformation they are bound to opposite nitrogen atoms but may jump from one pair to another(the so-called NH-tautomerism) in a two-well potential(Fig. 6.6) by photoexcitation. The barrier in the ground state is high enough(about 3500 $cm^{-1}$)[10] to ensure the stability of each tautomer at liquid helium temperature. Both tautomers have different orientations, but identical structures and identical spectra in free space or in a symmetrical environment. However, in a polystyrene host they have different local surroundings and, therefore, different spectra(inhomogeneous broadening, see Fig. 6.1c). When a monochromatic light is selectively absorbed by one tautomer, there is a finite probability of proton migration and transformation into the other tautomer.[11] As a result, absorption at the exciting wavelength will decrease and a spectral hole will be created(Fig. 6.1d). The path of the photoreaction described above is through the vibrational relaxation that follows the intersystem crossing (Fig. 6.7)[12]. The efficiency of such system is about 0.001. For OEP/PS $\Gamma_I / \Gamma_H \approx 10^3$. In summary, the OEP/PS system has a fairly high storage density, a

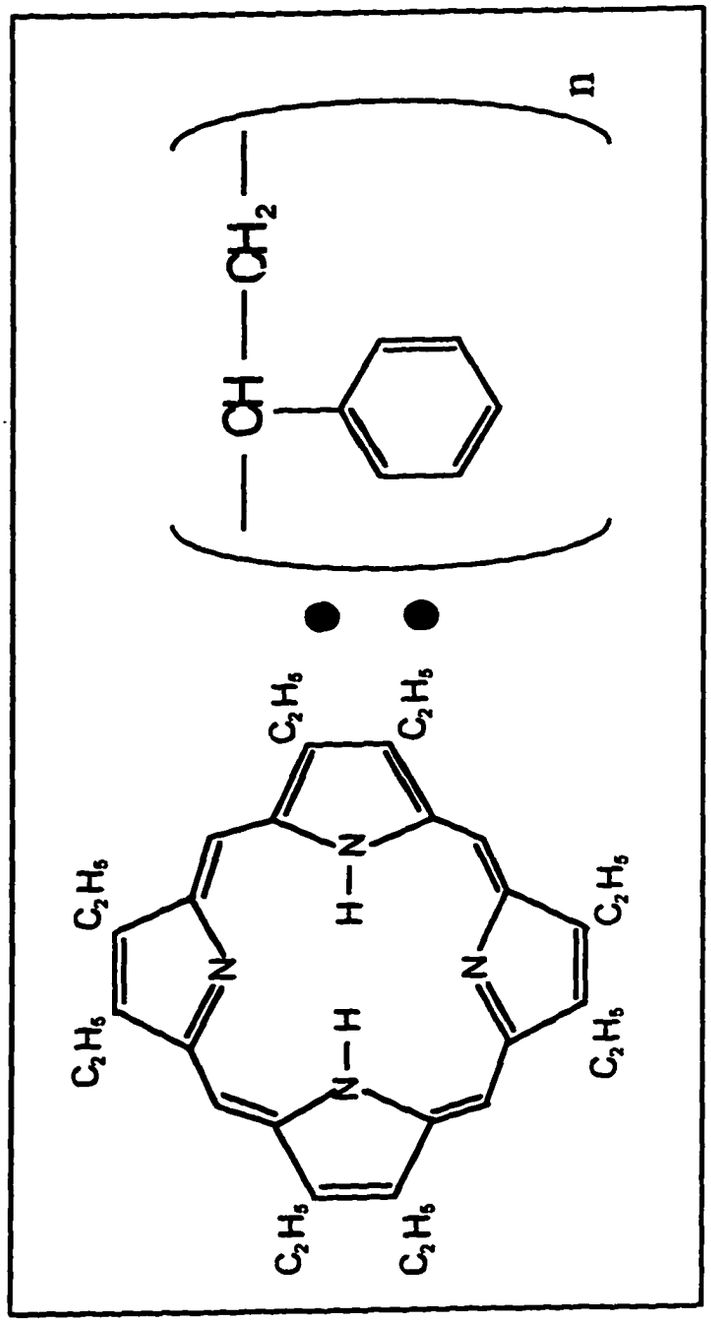


Fig. 6.4 Structure of free base octaethylporphine(OEP)-doped polystyrene.

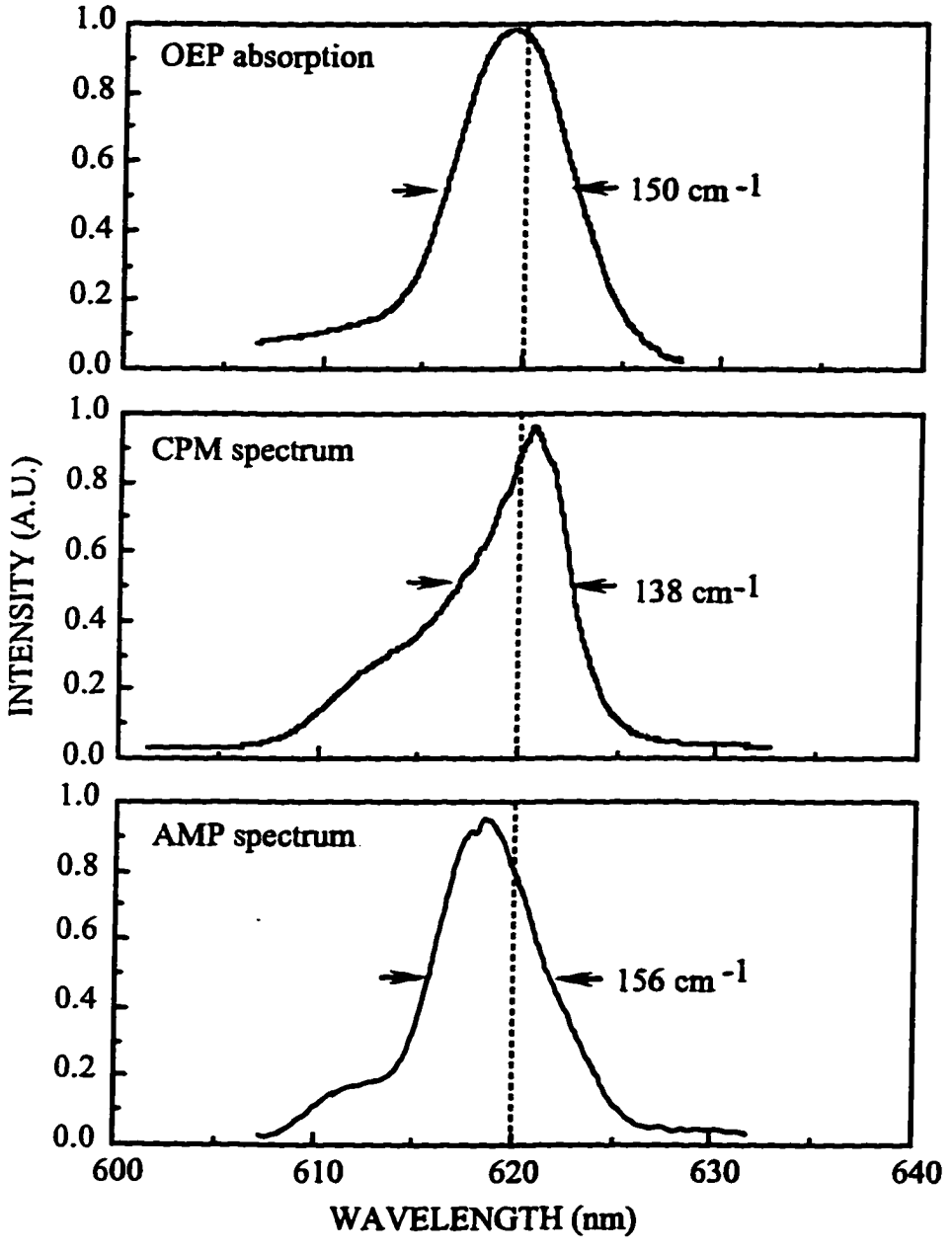


Fig. 6.5 OEP absorption, CPM and amplifier laser spectra.

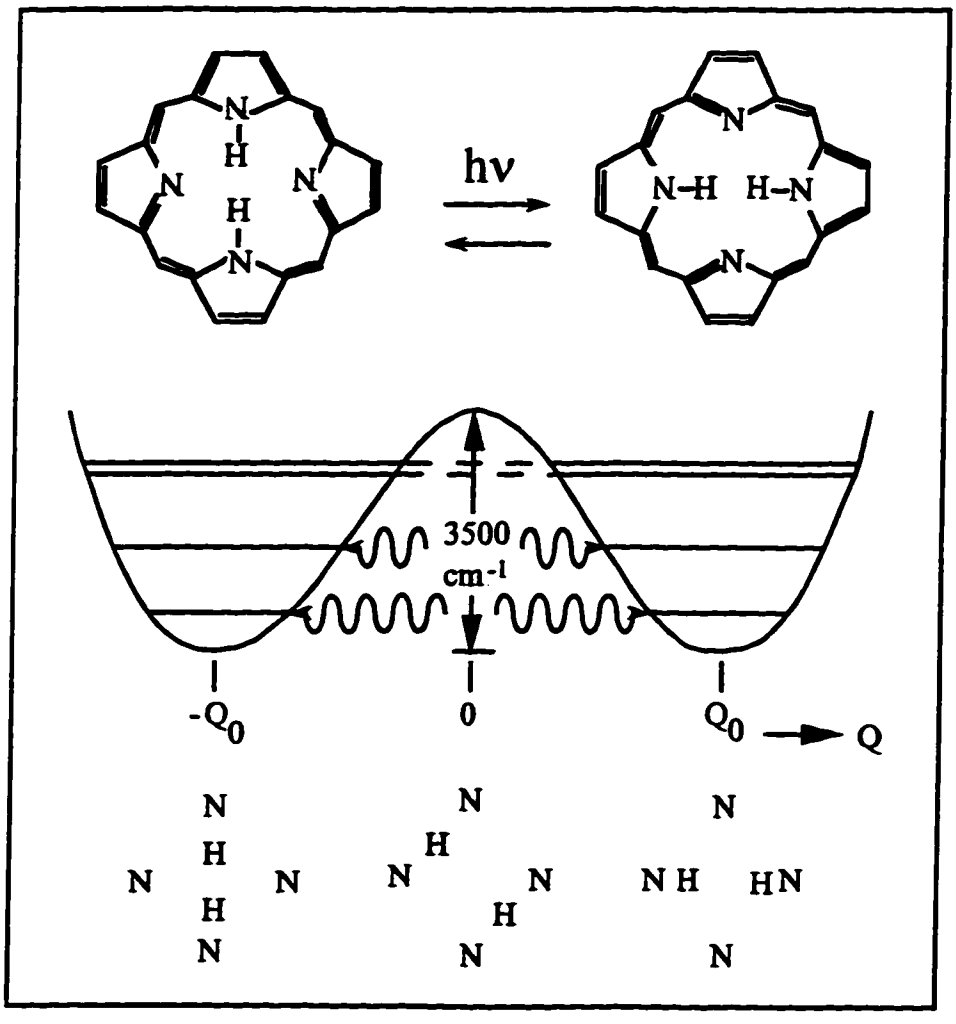


Fig. 6.6 The two-well potential of free-base porphyrin.

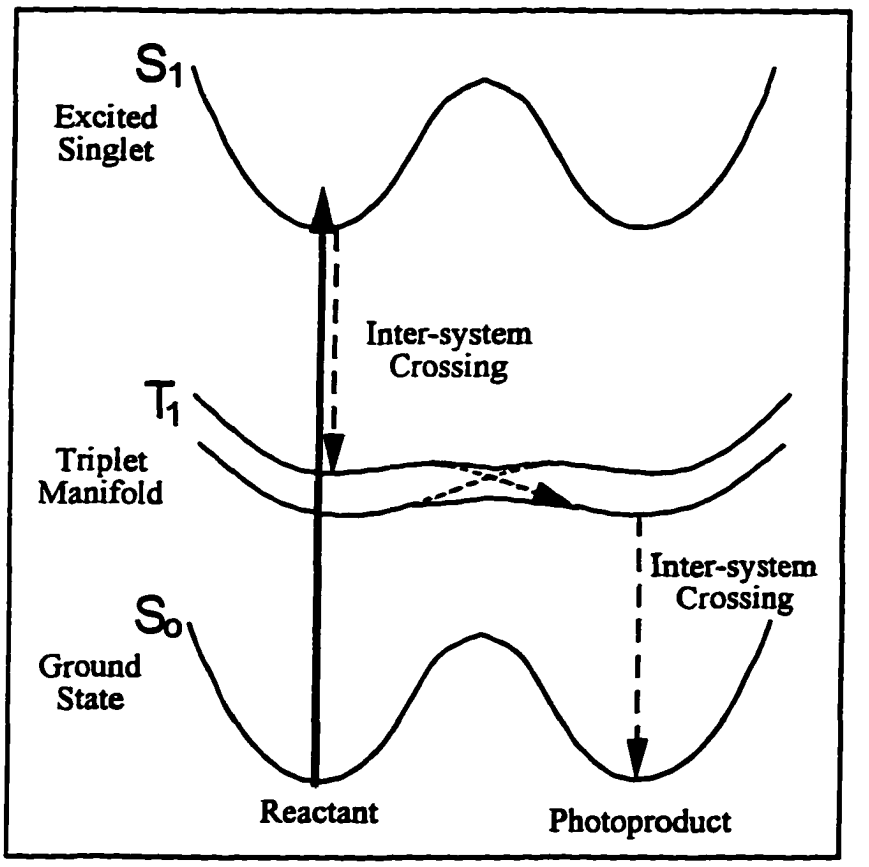


**Fig. 6.7 A possible pathway of OEP photoreaction. The solid arrow indicates the photoexcitation and the dashed arrows indicate the radiationless relaxation.**

very long storage time, a significant zero-phonon line and good overlapping with the CPM laser. The OEP/PS sample used in our experiment is a 0.7-mm-thick plate with a concentration of about $10^{-3}$ - $10^{-4}$ mol/*l*, which gives the optical density 0.96.

## References


1. A. A Gorokhovsky, R. K Kaarli, L. A. Rebane *JEPT Lett.* **20**, 216(1974)

2. B. M. Kharlamov, R.I. Personov, L. A. Bykovskaya *Opt. Commun.* **12**, 191(1974)

3. L. A. Rebane, A. A. Gorokhovsky and J. V. Kikas *Appl. Phys.* **B29**, 235(1982)

4. See *Spectral Hole-Burning and Related Spectroscopies,* **15** of 1994 *OSA Technical Digest Series, Optical Society of America,* Washington D. C. (1994)

5. A. Szabo, U.S. patent 3,896,420(July 22, 1975)

6. G. Castro, D. Haarer, R. M. Macfarlane and H. P. Trommsdroff, U.S. patent 4,101,976(July 18, 1978)

7. T. W. Mossberg *Opt. Lett.* **7**, 77(1982)

8. P. Saari, R. Kaarli and A. Rebane *Opt. Spektrosk* **56**, 387(1984)

9. A. Rebane, J. Aaviksoo and J. Kuhl *Appl. Phys. Lett.* **54**, 93(1989)

10. R. J. Abraham, G. E. Hawkes and K. M. Smith *Tetrahedron Leet.* **16**, 1483(1974)

11 K. N. Solov'ev, I. E. Zalesski, V. N. Kotlo, S. F. Shkirman *JETP Lett.* **17**, 332(1973)

12. S. Volker, J. H. van der Waals *Molecular Physics* **34**, No. 6, 1703(1976)

# Chapter 7

# Basic Properties of OEP/PS

This chapter describes my preliminary studies of the characteristics of OEP/PS related to the PHB processes, which includes the dephasing time, the saturation effect, the threshold for maximum number of readings and the temperature dependence.

## 7.1) Optical Dephasing Time $T_2$

The optical dephasing time $T_2$ of OEP/PS measured several years ago by time-domain two-pulse and accumulated echo experiments[1] at 1.9 K gave $1300 \pm 300$ ps and $600 \pm 80$ ps, respectively. The difference in temporal behavior is attributed to spectral diffusion, which is due to the long time scale energy fluctuations in the two-level system of the host. However in these experiments a 25 ps 5 Hz laser was used, and the bandwidth is only about 20 $cm^{-1}$ compared to the ~150 $cm^{-1}$ of the OEP/PS zero phonon line inhomogeneous broadening band. The behavior of $T_2$ for an ultrafast femtosecond pulse with a bandwidth which covers the whole inhomogeneous band of OEP/PS has not been determined. This is a very important situation in optical storage, since one wants to use a pulse as short as possible to achieve the highest storage density(the maximum length of data stream) and the highest access speed, within the optical dephasing time $T_2$. The shortest pulse allowed is the pulse with the bandwidth equal to the whole inhomogeneous band. Thus, we have performed the experiment to determine $T_2$ using a 125 MHz CPM

laser with the pulse duration of ~100 fs and the spectral width of ~140 $cm^{-1}$, which is the shortest possible pulse for OEP/PS in time-domain optical storage.

The OEP/PS sample is kept at a temperature of 1.4K. The time domain hologram were recorded in a spot of 0.8-mm-diameter with two CPM beams of total exposure ~ 1J/$cm^2$. The spectra of the CPM multi-shot and the amplifier single-shot echo signal are shown in Fig. 7.1. The integrated area gives the echo intensity:

$$I_{echo} = C \exp(-4t_{12}/T_2) \qquad (7.1),$$

where $t_{12}$ is the delay time between the signal and the reference pulses, and C is a constant. By measuring the echo intensities at different time delays $t_{12}$, the dephasing time $T_2$ was determined, as shown in Fig. 7.2. Since the echo decay time constant $\tau = 50 \pm 15$ ps, the dephasing time $T_2 = 4\tau = 200 \pm 45$ ps, which is smaller than $600 \pm 80$ ps measured by a 25 ps laser in a similar accumulated photon echo experiment. The difference is probably due to the different bandwidths of the lasers. The spectrum of the femtosecond laser used here covers the whole inhomogeneous broadening absorption band. Since the value of homogeneous line width $\Gamma_H$ is not the same over the entire inhomogeneous band[2], the photon echo measurement of $T_2$ reflects a weighted average of the homogeneous line width $\Gamma_H$ over the inhomogeneous line width $\Gamma_I$. It is conceivable that the different spectral band width of the lasers used in the two experiments results in different $T_2$ values. The $\Gamma_H$ determined by a spectral hole buring measurement[3] is ~ 300 ps in good agreement with the result here. The high power of the femtosecond laser may also contribute to the shorter $T_2$. Since the experimental condition is optimal in the laser spectral overlapping with the OEP/PS zero-phonon absorption band, the $T_2$ determined in

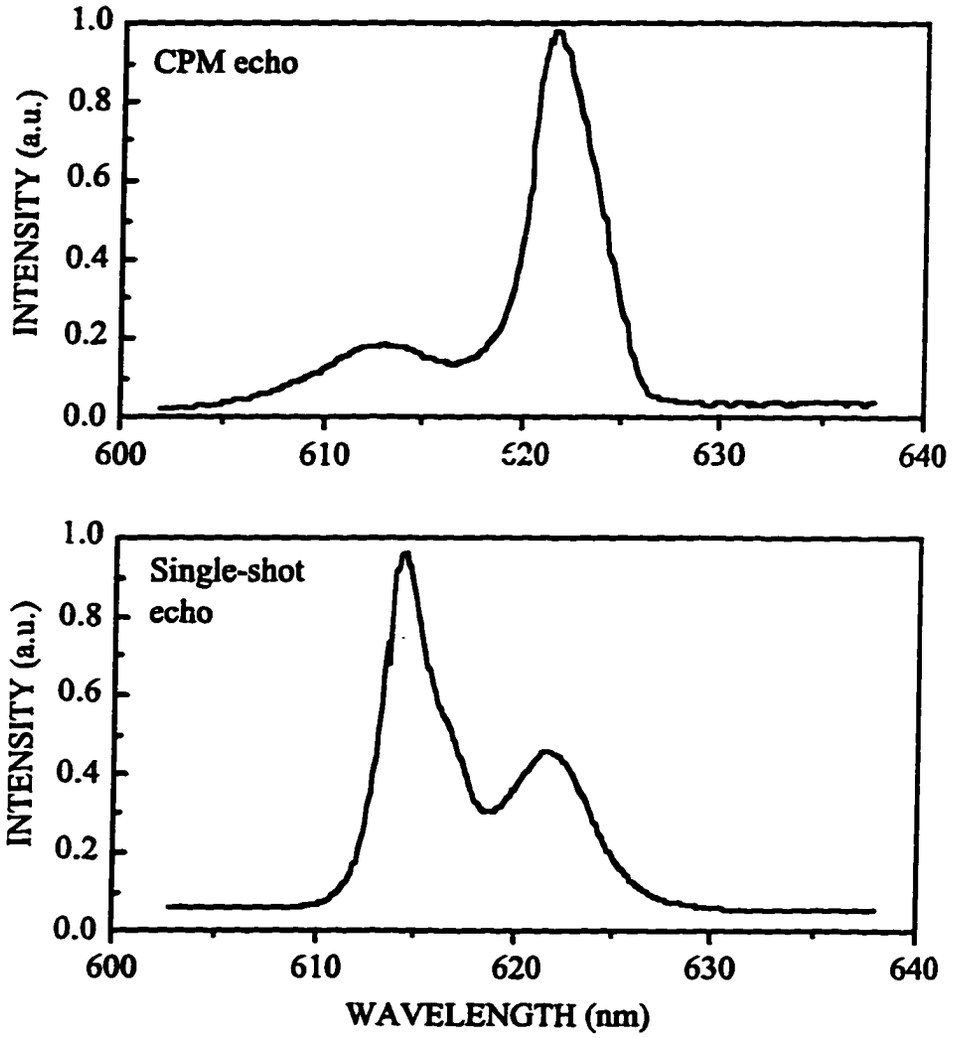


Fig. 7.1 The CPM multi-shot and amplifier single-shot echo spectra.

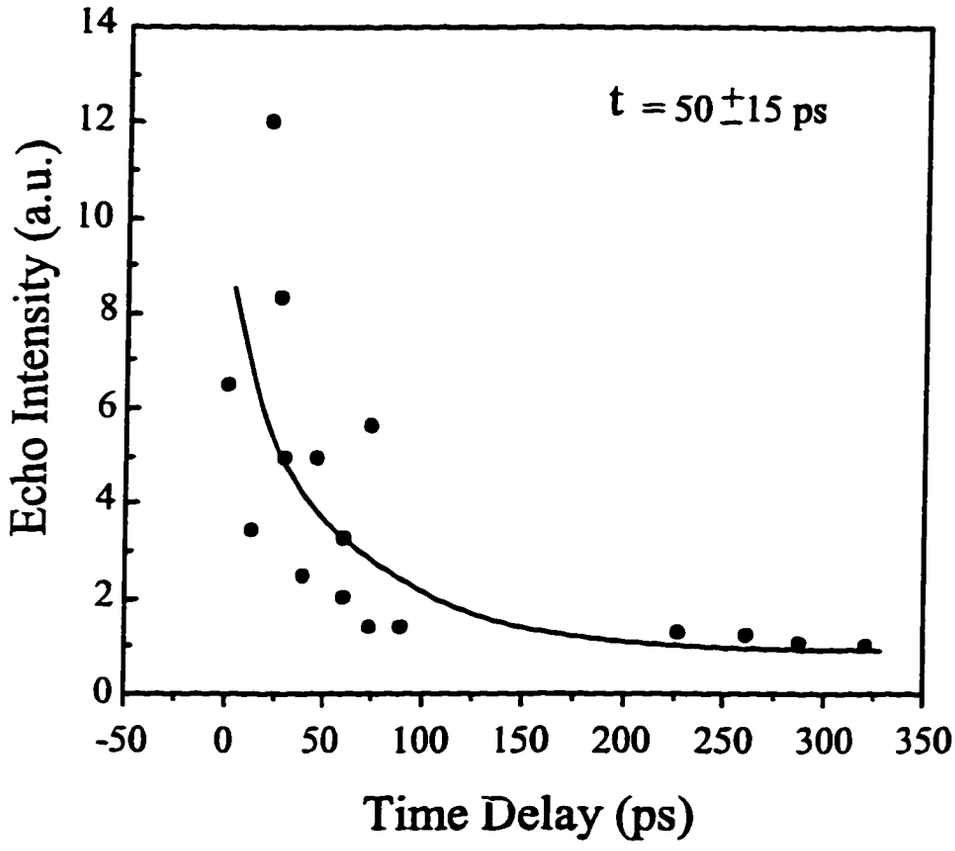


**Fig. 7.2 The dephasing time of OEP/PS is about 200 ps, corresponding to 50 ps decay constant.**

our experiment gives the upper limit of data length for OEP/PS optical storage applications. For example, using 100 fs pulses, one is able to store a maximum of 1000 bits of information in a single data stream. In photon echoes, the pure dephasing time $T_2^*$ plays a more important role than the excited state lifetime $T_1$, which has little effect in the optical dephasing process $T_2$ according to equation(6.1) and the fact that $T_1 = 17.5 \pm 1$ ns.[3]

## 7.2) The Saturation Effect

When writing information on a PHB material, one should optimize the dose of exposure. If the exposure is too small, there will not be enough modulation depth of the population grating. This results in a very weak echo data signal and a smaller number of readouts allowed(see readout experiment next). However, when a PHB material is over exposed, with the increasing irradiation of dose $I \cdot \tau$, photochemical reactions at the center of the line gradually come to a halt because most photoactive molecules have already converted. Consequently, photochemical reactions shift increasingly to the wings of the line leading to a line broadening, termed photochemical saturation broadening. In the range of the pseudo-phonon hole, however, the photochemical reactions still progress. This is because many more molecules absorb in the area of the broad pseudo-phonon wing compared to the narrow range of the zero-phonon hole. Therefore saturation must be avoided since it will decrease $T_2$. The saturation of the echo signal occurs at the dose of $6 J/cm^2$ for the OEP/PS sample at 1.4K, as shown in Fig. 7.3. The cause of the saturation effect can be explained by the following simplified picture. We assume that the

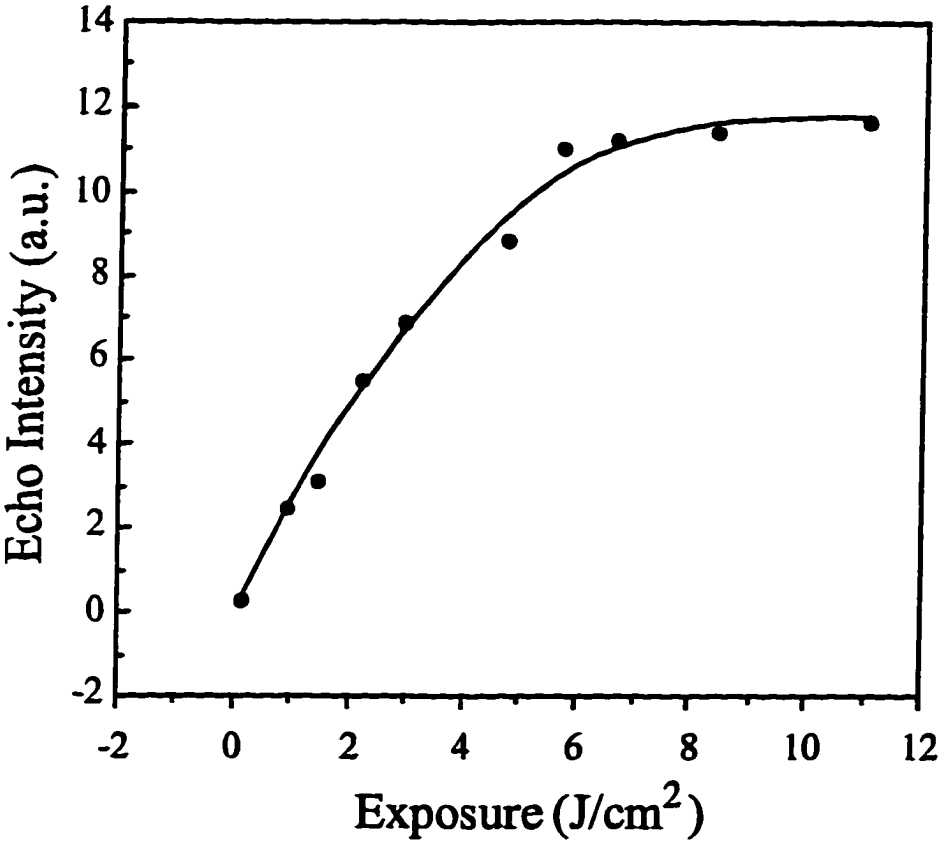


**Fig. 7.3 The echo intensity as a function of exposure. The saturation dose is about 6 J/cm.$^2$**

two-well potentials are randomly distributed within the inhomogeneous linewidth with equal forward and backward conversion probabilities, and omit the phonon side-band effect (Fig. 7.4). The rate equations for the reactant occupation numbers are:

$$dn_1/dt = -\frac{1}{2}\alpha n_1 I_1 + \frac{1}{2}\alpha I_2 n_2 \qquad (7.2),$$

$$dn_2/dt = -\frac{1}{2}\alpha n_2 I_2 + \frac{1}{2}\alpha I_1 n_1 \qquad (7.3)$$

and

$$n_1 + n_2 = N_0 \qquad (7.4),$$

where $n_1$ is the number of molecules in the reactant well, $n_2$ is the number of molecules in the photoproduct well, $N_0$ is the total number of OEP molecules, $\alpha$ is the absorption coefficient, $I_1$ and $I_2$ are the intensities of light at maxima and minima on the spectral domain, respectively. The solution is:

$$n_1(t) = \frac{1}{2}\,(N_0/(I_1 + I_2))\{(I_1 - I_2)\exp(-\frac{1}{2}\alpha(I_1 + I_2)t) + 2I_2\} \qquad (7.5).$$

Thus the saturation condition is:

$$n_1(t = +\infty) = N_0 I_2/(I_1 + I_2) \qquad (7.6),$$

which is due to the equilibrium of the transitions between the reactant and the photoproduct. When the spectral modulation is strong, the difference between $I_1$ and $I_2$ is large, the molecules in the reactant well will be effectively depleted. On the other hand, if the spectral modulation is weak, then $I_1 \sim I_2$, the number of molecules in the two potential well are almost equal. The optimal dose of exposure for OEP/PS at 1.4 K is ~ 5 J/cm$^2$.

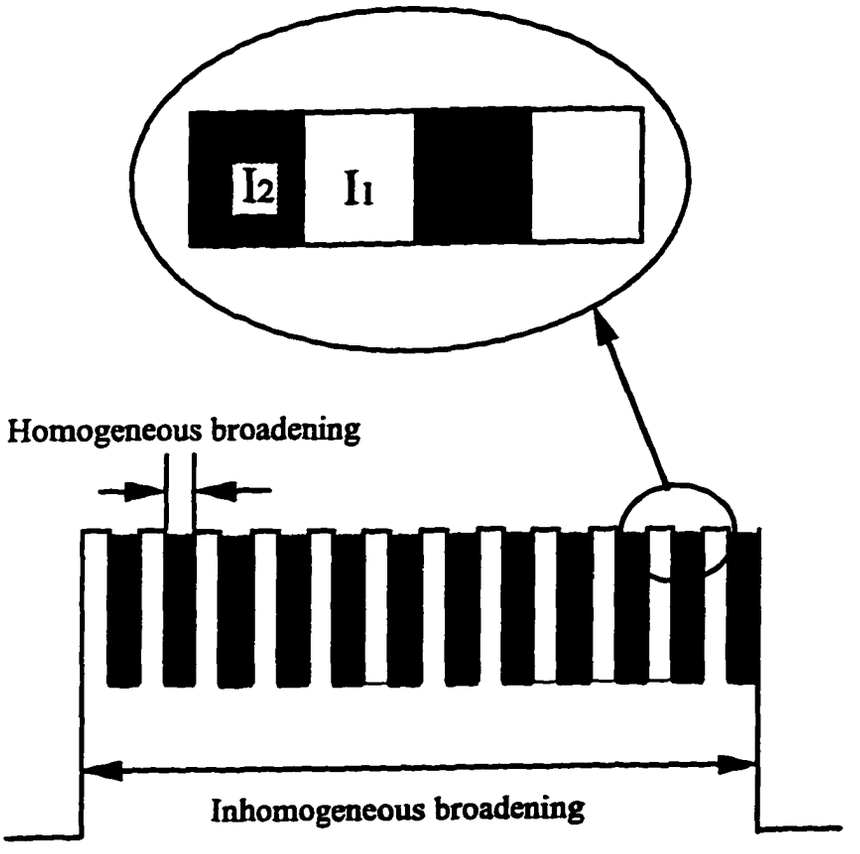


**Fig. 7.4 Simplified picture to account for the saturation effect.**

## 7.3) The Maximum Number of Readings

When readout is being performed from the OEP/PS optical memory, the data signal will be gradually degrading. The reason is that the reading pulse has a different power spectrum from that of the two writing pulses, and thus destroys the population grating. The readout dose of irradiation that the population grating could tolerate determines the maximum number of times one can retrieve the stored information from the optical memory. According to the two-well potential with the inhomogeneous broadening model of OEP/PS, the irradiation only makes the molecules flip between the two potential wells. Therefore, we expect the same amount of energy will be needed to destroy the population grating as that of writing. Fig. 7.5 shows that with 0.65 ~ 0.7 μJ/pulse single shot readout, one can read about $10^4$ times without any significant degradation of the echo signal, which corresponds to a total of 7 mJ of energy. The intensity of the single shot readout on the 0.8 ~ 1 mm diameter spot is about $5x10^8$ $W/cm^2$. The echo signal falls to half of its initial amplitude when the readout is $5x10^4$ times, corresponding to 35 mJ of total energy. When we write the hologram to produce the population grating in OEP/PS, the signal beam is 0.55 mW and the reference beam is 0.37 mW, respectively. The writing time is 50 sec. Therefore the total irradiation energy on a OEP/PS sample is about 46 mJ, corresponding to ~5 $J/cm^2$ of dose. Since this value is close to the writing saturation dose, one cannot increase the maximum number of allowed readings by increasing the writing dose further. Thus, the writing dose determines the maximum reading dose, which in turn gives the maximum number of allowed readings. However, the upper limit is set by the saturation dose.

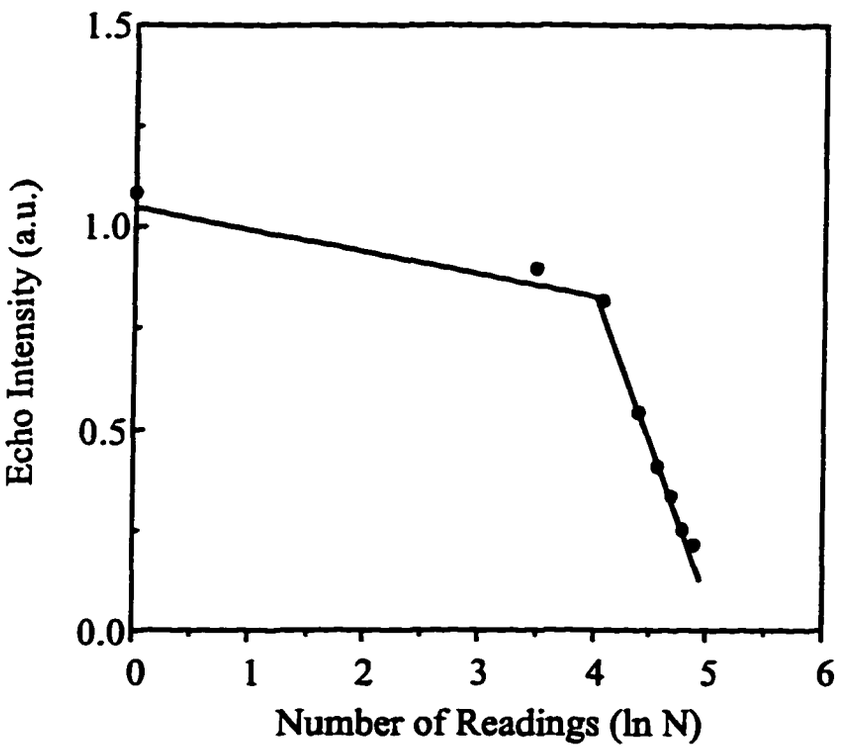


**Fig. 7.5 Echo intensity versus the number of readings.**

## 7.4) The Temperature Dependence

The above experiments were done at 1.4 K. As the temperature increases, the echo signal decreases due to the stronger phonon scattering which reduces $T_2$. Fig. 7.6 depicts the dependence of the multi-shot echo intensity on the temperature of the OEP/PS sample. The time delay is set at 6 ps. The linear fitting

$$\frac{I_{echo}(T)}{I_{echo}(T_0)} = [1 - \beta(T - T_0)] \qquad (7.7)$$

gives the decrement coefficient $\beta$ ~4% per Kelvin for $T_0$ ~1.4 K,. The echo signal will fall to zero at ~25 K from an extrapolation. Based on equations (7.1) and (7.7) one can estimate the $T_2$ dependence on temperature T:

$$\frac{1}{T_2(T)} = \frac{1}{T_2(T_0)} - \frac{1}{4t_{12}} \ln[1 - \beta(T - T_0)] \qquad (7.8)$$

where $\beta$ ~4% per Kelvin for $T_0$ ~1.4 K and $t_{12}$ = 6 ps. $T_2$ reduces to 100 ps at 4.2 K compared to 200 ps at 1.4 K. To maintain the population grating, get good reproduction of data signal and keep the high data capacity, the OEP/PS sample must be kept at a very low temperature. This is a severe restriction on OEP/PS application for optical memory.

In summary, the optical dephasing time $T_2$ for a laser bandwidth covering the whole inhomogeneous zero-phonon absorption band is determined to be $200 \pm 50$ ps, which is shorter than the one measured by the much narrower band laser. The reason is attributed to the different homogeneous linewidths over the inhomogeneously broadened zero-phonon absorption band. The high power of the femtosecond laser might also be a

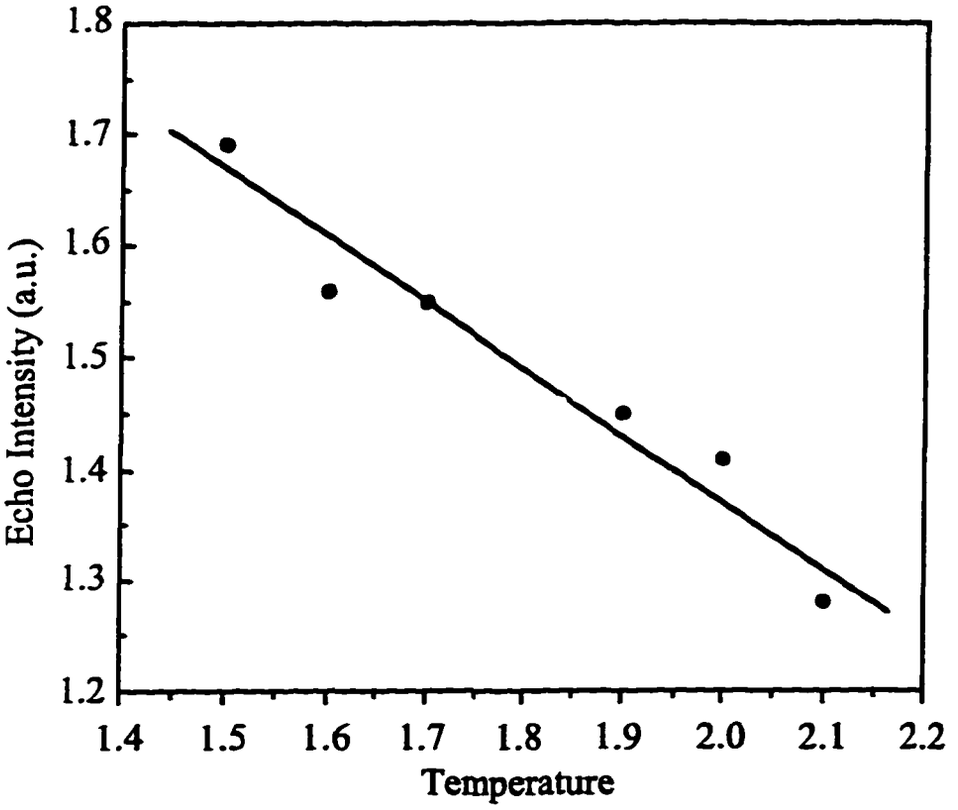


**Fig. 7.6 Temperature dependence on the multishot echo intensity.**

factor. The writing saturation occurs for an irradiation dose above 6 J/cm$^2$, which is due to the equilibrium of the transitions between reactant and photoproduct. The maximum number of allowed readings is determined by the amount of energy of writing. The optimal writing dose is about 5 J/cm$^2$. $T_2$ reduces significantly as the sample temperature increases. It is only 100 ps when the temperature increases to 4.2 K, compared to the value of 200 ps at 1.4 K. This temperature dependence indicates that OEP/PS must operate at a very low temperature.

## References

1. A. Rebane and D. Haarer, *Optics Communication* **70**, 478(1989)

2. K. K. Rebane and A. A. Gorokhovsky *Journal of* Luminescence **36**, 237(1987)

3. A. A. Gorokhovsky, V. Kh. Korrovits, V. V. Palm and M. A. Trummal *Laser Optics of Condensed Matter* ed. by J. L. Birman *et al*, Plenum Press, New York and London (1988)

# Chapter 8

# Research on OEP/PS Persistent Hole Burning Optical Storage

This chapter describes my thesis research on the persistent hole burning optical storage using femtosecond spectroscopy and accumulated photon echo in OEP/PS. The objectives are achieving ultrafast information retrieval and realizing fast recording of data.

## 8.1) Ultrafast Information Retrieval on OEP/PS

The experiment is to achieve, for the first time, the femtosecond ultrafast single-shot information retrieval on OEP/PS: 27 terabits/sec.

Recently, femtosecond PHB holography was used with a standard multishot second harmonic-generation method and a mechanically variable time delay for the detection of echo pulses[1]. This kind of detection technique is not fit to time-domain PHB optical storage. First, the second harmonic method requires high intensity while the data signal is usually very weak for the following reasons. (1) As described in the readout experiment in Chapter 7, one wants to be able to read the stored information as many times as possible. However, the upper limit of readout dose is set by the writing saturation dose, consequently, one has to use a weak readout pulse to increase the number of allowed readings. (2) The retrieved data information is in the form of a photon echo signal diffracted from a population grating, which is usually much weaker than the

readout pulse(0.1~1%). (3) The energy diffracted from the readout pulse has to be distributed over the whole data bit stream in the time period of $T_2$ in order to get a high density of storage, which makes each data bit pulse very weak. Second, the multi-shot and mechanically variable time delay cannot obtain high speed information retrieval. In order to achieve the high data density, fast retrieval, a large number of readings and small distortion of echo data signals, an ultrafast single-shot method for the detection of accumulated photon echoes on the femtosecond time scale was developed. It is based on the interferometric cross-correlation technique described in Sections 2.3 and 2.4 of Chapter 2. This ultrafast information retrieval technique converts a data pulse stream into a corresponding two-dimensional interference pattern that permits the simultaneous registration of all data bits by a CCD detector. Using this new technique, 150 fs single-shot detection of a 4-bit pulse packet that provides a data readout speed in PHB media as fast as 27 Tbits/sec has been achieved.

The readout speed for this method is $n\Gamma_I$, where n is the number of bits in the data train. Since the maximum value of n is $\Gamma_I/\Gamma_H$, a readout speed as high as $\Gamma_I^2/\Gamma_H$ can be achieved. For the OEP/PS sample, the FWHM of the absorption band is 150 $cm^{-1}$, $\Gamma_I/\Gamma_H$ = 500 ~ 1000. The ultimate readout speed of ~$10^{15}$ bits/sec can be obtained at a low temperature of 1.4 K.

The basic principle of the single-shot interferometric cross correlator is shown in Fig. 8.1. A plane-wave cross-reference pulse is incident along the normal of the diffraction grating and a plane-wave signal pulse is incident at an angle $\alpha$ relative to the normal. Both beams are combined at the diffraction grating. The first diffraction order

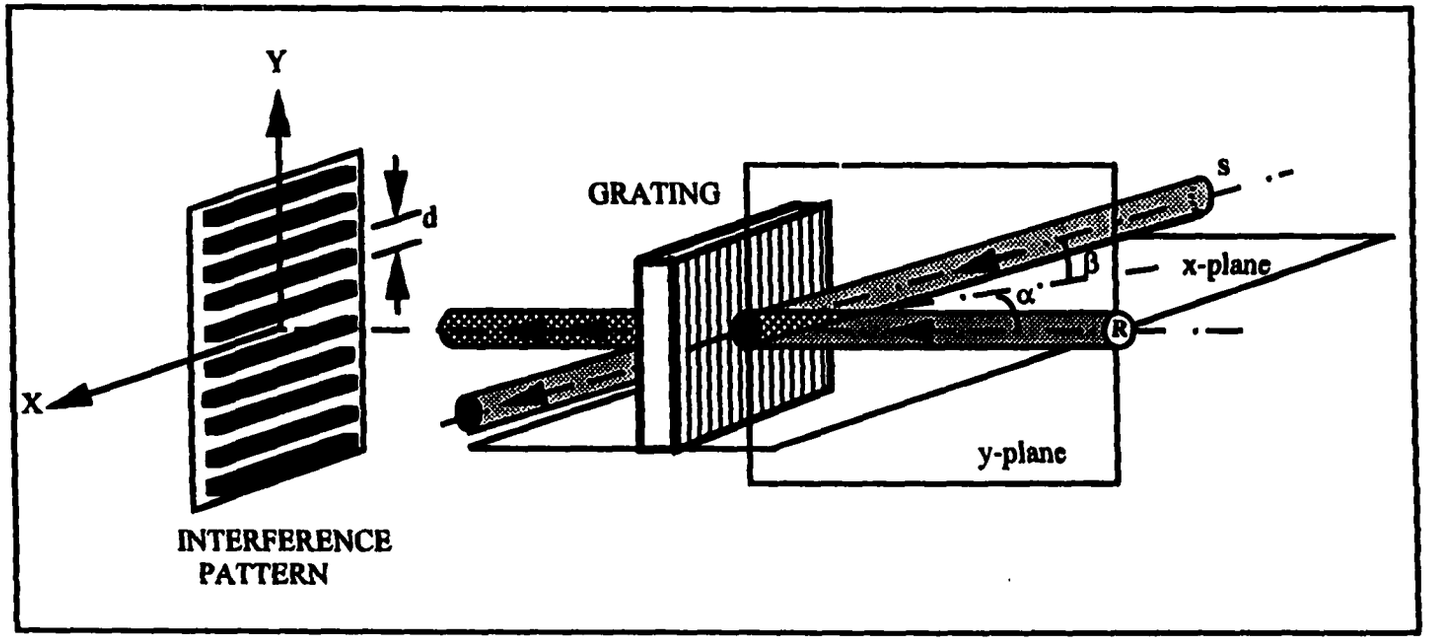


Fig. 8.1 Interferometric single-shot cross correlator. Signal (S) and cross-reference (R) beams interfere after the diffraction grating, which introduces a continuous optical delay between them.

from the signal beam propagates in the direction of the cross-reference beam ($p \sin \alpha = \lambda$; $p$ is the spacing between grooves). The grating plane is optically conjugated with a CCD detector by a lens. The interference fringes are tuned in the direction of the grating dispersion (x axis). One of the beams is oriented at a slightly different angle to the plane of incidence to produce the desired fringe pattern in the vertical (y axis) direction.

The diffraction grating introduces a continuous optical delay along a given interference fringe. The path difference is

$$\Delta = c\tau = \lambda x/p, \tag{8.1}$$

where $\lambda$ is the wavelength, x is the linear coordinate, and $\tau$ is the time delay between the beams.

Consider the electric fields $E_d(t)$ and $E_r(t)$ from the echo and cross-reference pulses traveling in the two arms of the cross correlator. According to equations (2.16) to (2.21) of Chapter 2, the fringe visibility is given by

$$K(\tau) = [I_{max}(\tau) - I_{min}(\tau)] / [I_{max}(\tau) + I_{min}(\tau)] \tag{8.2}$$

and

$$K(\tau) = B|E_d(\tau)|. \tag{8.3}$$

Equation (8.3) is used to find $|E_d(\tau)|$.

A schematic of the experimental arrangement is shown in Fig. 2.19 of Chapter 2. The 620 nm pulses of duration 100 fs and bandwidth ~140 $cm^{-1}$ are generated by a colliding-pulse mode-locked (CPM) dye laser with a repetition rate of 125 MHz and 6 mW average power. The amplifier system is pumped by a $Q$-switched Nd:YAG laser at a

20 Hz repetition rate and produces amplified pulses with 1 μJ energy per pulse (3-stage amplification).

Two CPM laser beams, the signal and the reference, are superimposed in a 4-mm-diameter spot on the OEP/PS sample. The signal is stored in the sample after 2 - 3 minutes of exposure ($2J/cm^2$). The stored information is retrieved by applying an amplified single-shot readout pulse (30 nJ/pulse) on the sample. The retrieved echo pulses propagate in the direction of the original signal and are directed into a first-order interferometric cross correlator. The echo signal is incident on a volume holographic diffraction grating at an angle $\alpha$ of ~ 30° and is combined with the cross-reference beam at the grating to generate the interference fringes. A grating of period $p = 0.001$ mm and diffraction efficiency of ~ 80% is used. This grating gives the maximum optical delay length $x_{max} = 40$ mm, corresponding to the 80 ps time-delay window of the cross correlator.

The two-dimensional image of interference fringes is recorded by a CCD image sensor (Photometrics Ltd., Model CH250). The intensities $I_{min}(\tau)$ and $I_{max}(\tau)$ are measured along the dark and bright fringes, respectively. The fringe visibility that represents the cross correlation is determined according to Equation (8.2) as a function of continuous time delay, averaged over five fringes.

Figure 8.2a depicts a CCD image of the interference pattern between the readout and cross-reference pulses. The exposure time of the shutter was shorter than 50 ms, permiting the selection of a single pulse from the 20 Hz readout pulse train. Figure 8.2b shows the digitized profile of visibility that corresponds to the cross-correlation curve.

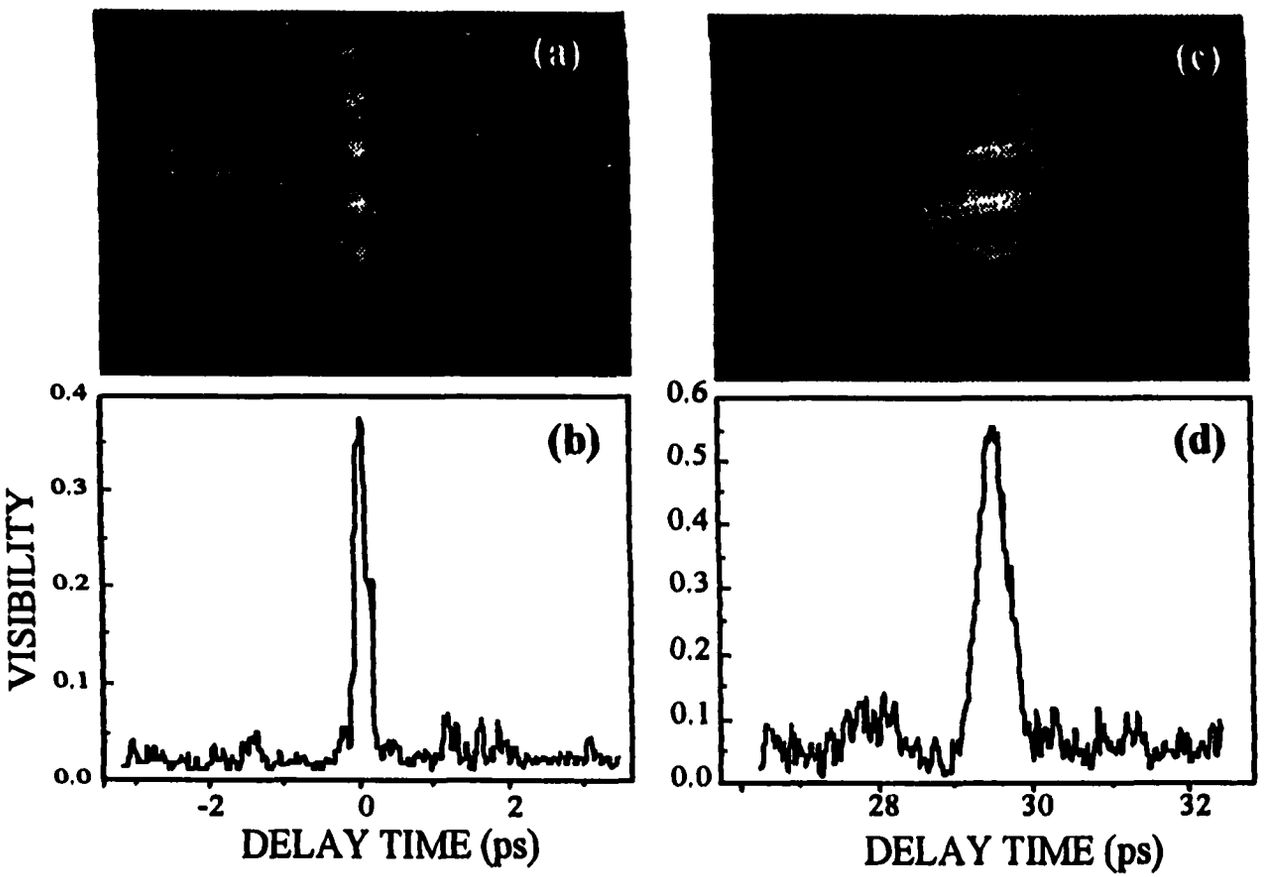


Fig. 8.2 a) Single-shot CCD image of the two-dimensional interference pattern between readout and cross-reference pulses; b) The corresponding cross-correlation digitized trace of image a at zero delay. c) Image of the interference pattern between echo and cross-reference pulses; d) The corresponding cross-correlation digitized trace at 30 ps delay relative to the readout pulse.

The amplitude correlation time is ~ 150 fs. A CCD image of the single-shot interference pattern between the echo (with a delay of 30 ps relative to the readout pulses) and cross-reference pulses is displayed in Fig. 8.2c. The corresponding digitized cross-correlation curve with a FWHM of 340 fs is shown in Figure 8.2d. Comparing the original signal (Fig. 8.2b) with the recalled echo signal (Fig. 8.2d), the latter exhibits an approximately twofold broadening. The diffraction efficiency of single-shot echo pulses is 0.1 ~ 1%.

Figure 8.3 demonstrates cross-correlation detection of the four-pulse echo packet on a single-shot basis. The four-pulse packet is produced by a multistep glass plate that is inserted into the input signal beam as shown in Fig. 2.19 of Chapter 2. This four-pulse packet information is stored in the OEP/PS sample. The echo pulse packet is recalled by an amplified pulse. A CCD image of the single-shot interference pattern between the recalled four-pulse echo packet and a cross-reference pulse is displayed in Fig. 8.3a, and the corresponding digitized cross-correlation trace is shown in Fig. 8.3b. The echo pulses are separated by 1.7 ps. The interference pattern and the cross correlation of the echo signals demonstrate the good single-shot reproduction of the temporal profile of the initial pulse packet and provides 4 bits of information/150 fs, which corresponds to a data readout speed of 27 Tbits/sec.

One may speculate on at least two reasons for echo pulse broadening. The first is imperfect overlapping of the spectra of the OEP sample absorption band, the CPM writing pulses, and the amplified readout pulse. The second is the saturation of optical absorption in PHB material by the readout pulse, which causes bleaching and thus leads to the distortion of the echo signal. At our registration conditions, the readout pulse intensity of $4 \times 10^{24}$ photons/sec cm$^2$ exceeds the saturation level for the full absorption

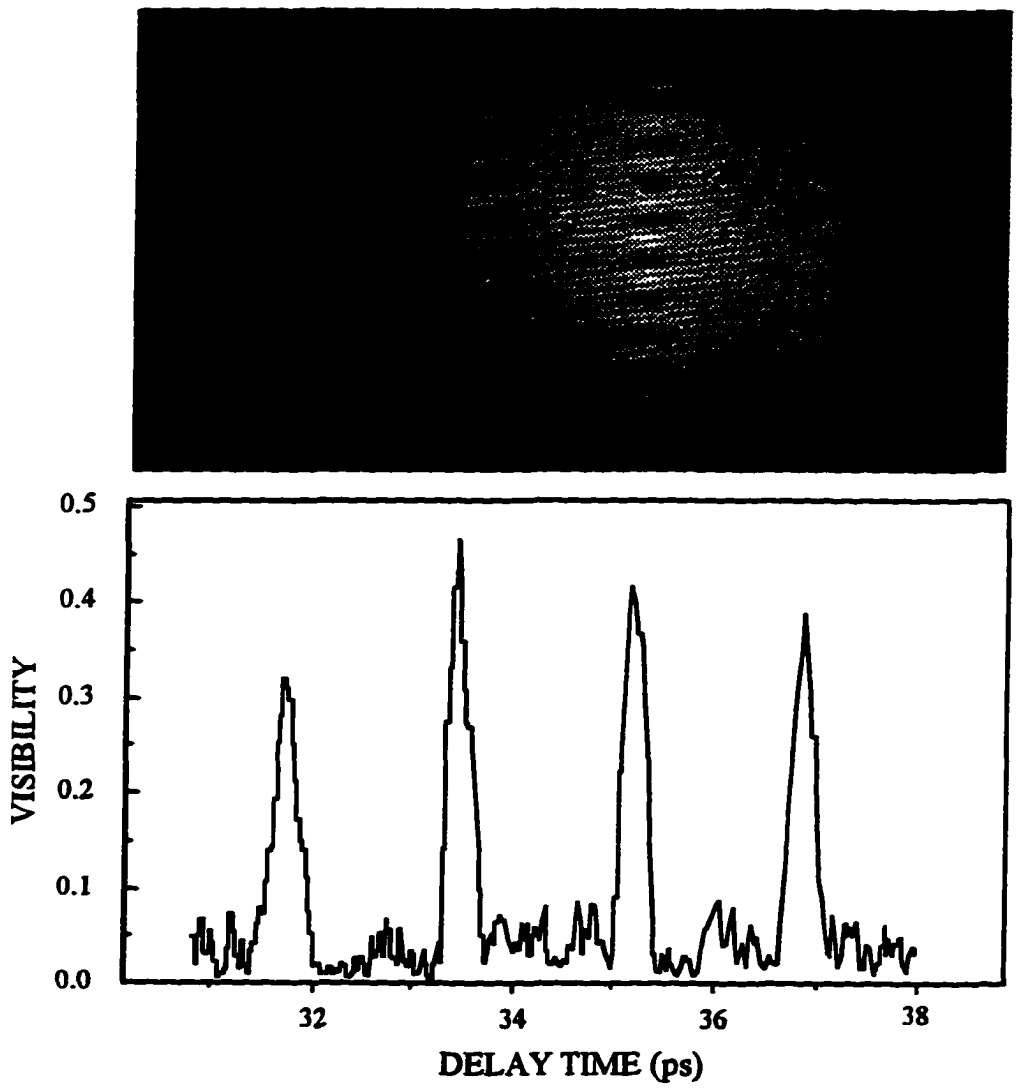


Fig. 8.3 a) Single-shot CCD image of the two-dimentional interference pattern between the retrieval echo four-pulse packet and a cross-reference pulse; b) The corresponding cross- correlation digitized trace of the retrieval echo packet at 30 ps delay relative to a readout pulse.

band of OEP sample by approximately an order of magnitude. Despite such a level of saturation, an echo signal of reasonable fidelity is observed(Fig. 8.3).

In the above ultrafast retrieval implementation, a 150 fs single-shot detection of a 4-bit packet stored in an OEP/PS sample, which corresponds to a data readout speed of 27 Tbits/sec, has been demonstrated for the first time by a novel low-intensity interferometric cross-correlation technique. OEP/PS is a good PHB material for optical storage for it has high data density(~1000), long storage time, good overlapping with a CPM laser and it can achieve very fast information retrieval. The disadvantage is that the writing is relatively slow and has to operate at very low temperature. The former may be overcome in the experiments discussed in next section.

## 8.2) Improving Hole Burning Efficiency on OEP/PS for Faster writing

In the previous section, we have demonstrated that the persistent hole burning optical storage material OEP/PS can perform very fast information retrieval operation. However, one problem for this material is that the writing(hole burning) time is relative long, usually a few seconds or more with a dose of 5 J/cm$^2$. Such a slow burning is due to the triplet bottleneck. Upon photoexcitation, an OEP molecule jumps from one potential well to the other[2], i.e. reorientation of its central hydrogens. The molecule has to go through the vibrational relaxation that follows the intersystem crossing from $S_1$ into a triplet manifold(Fig. 8.4, slow transition path)[3]. When photoexciting OEP molecules to their first excited singlet state $S_1$, ~5% of them will go back to the ground state $S_0$ through radiative relaxation, ~95% of them go through a radiationless process to the first triplet $T_1$

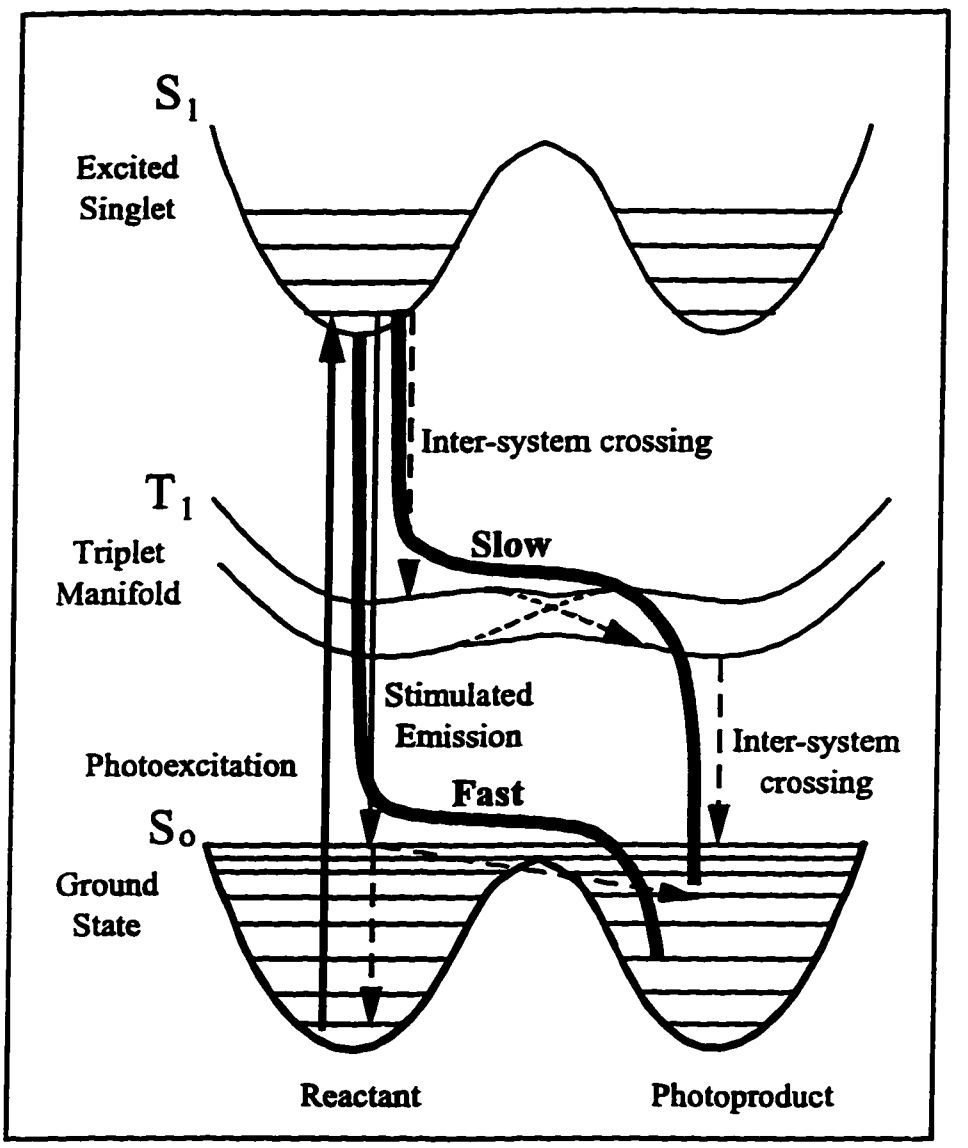


Fig. 8.4 A new pathway of OEP photoreaction through stimulated emission to improve the hole burning efficiency by avoiding the involvement of the triplet state. Dashed arrows indicate the radiationless relaxation.

and then relax to $S_0$ of either reactant or photoproduct[4]. Only 0.1~1% of the excited molecules go to the photoproduct[3, 5], which makes the efficiency only about 0.001. The probabilities of non-radiative relaxation from $S_1$ to $S_0$ and radiative relaxation from $T_1$ to $S_0$ are very small($T_1$->$S_0$ radiative quantum yield < $10^{-5}$, fluorescence yield $\Phi_f$ + triplet yield $\Phi_t \sim 1$) for free base prophyrin[6-7]. The lifetime of the first singlet excited state $S_1$ is ~18 ns[8] while that of the lowest triplet state $T_1$ is ~ 1 ms at 1.4 K[9]. Thus the key point for fast writing on OEP/PS is to overcome such $T_1$->$S_0$ triplet bottleneck.

In order to achieve this goal, an experiment was performed using stimulated emission to bring the molecules in $S_1$ directly down to the higher vibrational levels of $S_0$ without the involvement of the triplet state $T_1$, which alters the natural photoexcitation pathway of OEP/PS and thus improves the hole burning efficiency.

The experiment is based on the following promises: 1) one could bring the excited OEP molecules in $S_1$ down to $S_0$ within the lifetime of $S_1$ by stimulated emission; 2) The probability for a molecule at a high vibrational level of $S_0$ goes from reactant well to photoproduct well is comparable to the vibrational cooling process. If one photoexcites OEP molecules to $S_1$ by a strong pump in the zero-phonon line absorption band, then uses a second pulse to bring them down to high vibrational levels of $S_0$ by stimulated emission, we could expect an increment of molecules to go to the photoproduct according to the second premise above[10-11]. The quantum yield for an OEP molecule to go to the photoproduct through this new pathway should be larger than that of the natural photoexcitation pathway. Thus by altering $S_1$->$T_1$->$S_0$(photoproduct) transition to $S_1$-

$>S_0$(photoproduct) transition, the $T_1$->$S_0$ triplet bottleneck problem could be avoided and fast writing could be achieved(Fig. 8.4, fast transition path).

The experimental setup is described in section 2.6 of Chapter 2. OEP/PS material has a $S_0$->$S_1$ absorption peak at 619 nm at liquid helium temperature[8]. At liquid nitrogen temperature, absorption and fluorescence peaks are at 620 nm and 683 nm, respectively[6]. The experiment is done at liquid nitrogen temperature. It consists of 3 laser beams shown in Fig. 2.23 of Chapter 2. The 620 nm amplified CPM laser pulse is used as the burning beam. The 680 nm pulse amplified from the supercontinuum is used as the stimulating light and set at a time delay relative to the burning pulse within the lifetime of the first excited singlet $S_1$. The third monitoring beam is used to measure the sample transmission after different exposures of 620 nm burning pulses. The efficiency could be compared with or without the 680 nm stimulated pulse.

Two sets of detection setups were employed. One of the setups uses a Boxcar averager with photodiodes and the wavelength of the monitoring pulse is also 620 nm. The other setup uses a spectrograph coupled with a CCD camera, the monitoring pulse is a white light continuum. The boxcar setup can continuously monitor the absorption change as a function of burning exposure with a better signal to noise level. The CCD setup can monitor absorption changes at different wavelengths at the same time, thus it is easier to obtain the spectroscopic feature of the writing process. The two detection methods complement each other.

The experimental result from the boxcar averager with photodiodes system is shown in Fig. 8.5. The ordinate is the sample transmission and the abscissa is the exposure time of the burning pulses (except for curve a, see below). The three curves are

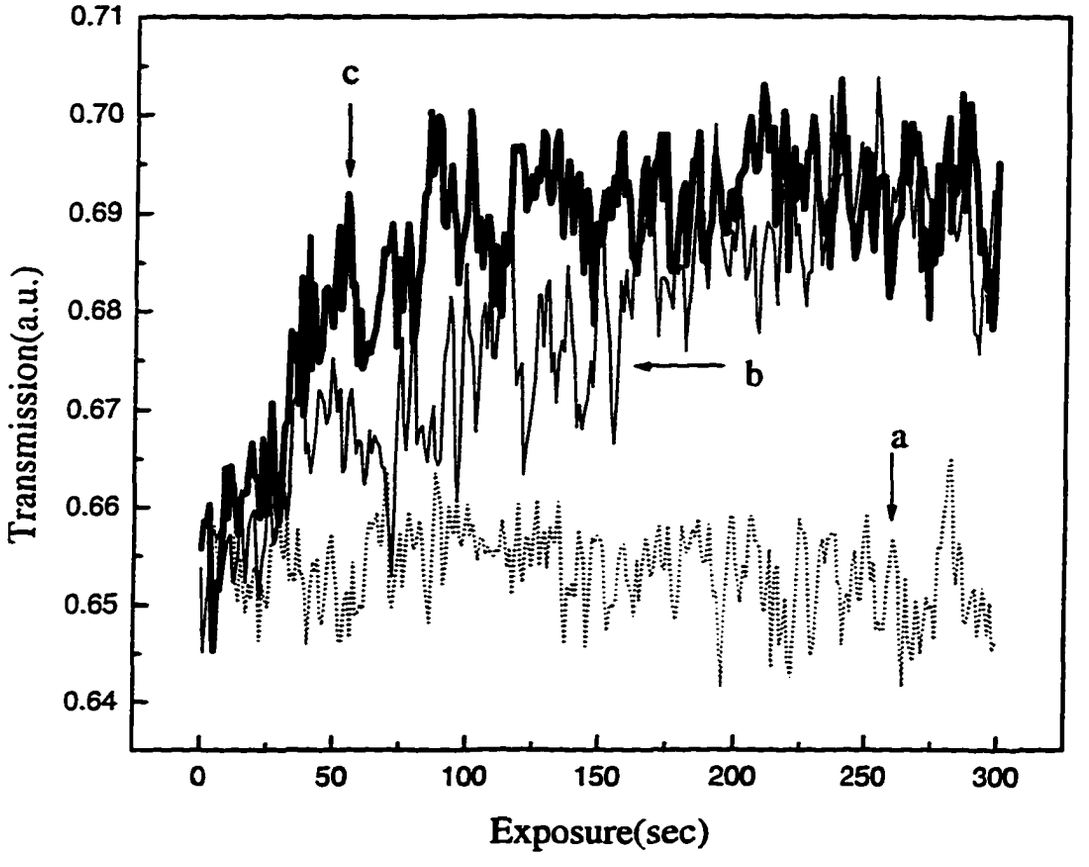


Fig. 8.5 OEP/PS transmission at 620 nm as function of burning exposure. Curve a is probe only indicating the background. Curve b is the transmission without stimulated emission. Curve c is the transmission with the 680 nm stimulated emission.

monitored at 620 nm with a band width about ~8 nm under different conditions. Curve a is the monitoring beam only, neither the burning beam nor the stimulating beam is present. In this case the abscissa is simply the exposure time of the weak monitoring beam. Thus curve a indicates the background noise. Curve b is the transmission change of the OEP/PS sample in the presence of the 620 nm burning beam. As the burning exposure time increases, the transmission of the OEP/PS sample at 620 nm increases, indicating more molecules are transferred from the reactant well to the photoproduct well. When the burning time reaches 220 seconds, the transmission becomes stable and saturation occurs. Curve c is the transmission change of the OEP/PS sample when both the 620 nm burning pulse and the 680 nm stimulating pulse are present. It is apparent that in this case the saturation happens at ~75 seconds. Since both curve b and curve c were obtained for the same intensity of burning pulse, it suggests that the presence of the 680 nm stimulating pulse could effectively enhance the hole burning efficiency at least twice as much as without the 680 nm stimulating pulse (curve b). It proves the experimental design was correct. In the writing process on the optical storage material OEP/PS, we can use an additional pulse to alter the natural photoreaction pathway by stimulated emission to improve the writing efficiency. The physics was stated previously in this section: due to the triplet bottleneck, the writing efficiency of OEP/PS through the natural pathway is low. However, when we first use a 620 nm pulse to pump the OEP molecules to the $S_1$ state, and then use a second pulse of 680 nm within the life time of $S_1$ to induce the stimulated emission, the molecules in $S_1$ will go down to the high vabrational levels of $S_0$ and by-pass the triplet $T_1$ state. In Fig. 8.5 the sample transmission change saturates at least two times faster in the presence of the 680 nm stimulated emission(curve c) than the

one without(curve b), showing that the molecules in the reactant well deplete much faster in the presence of stimulated emission. These results suggest that vibrational relaxation from the high vibrational levels of the reactant well to the ground state of the photoproduct is more efficient than the $T_1$->$S_0$(photoproduct) triplet-singlet inter-system crossing for OEP molecules.

The OEP/PS absorption changes as a function of exposure, without and with the stimulating emission beam measured with a spectrograph and a CCD camera are given in Fig. 8.6 and Fig. 8.7. In each figure two typical exposure curves are shown, one is the absorption before the exposure to the burning pulse and the other is the absorption after 600 seconds of exposure. After the exposure to the burning pulse, the absorption band is shifted to the shorter wavelength. This shift can come from the reactant to photoproduct conversion. The most salient feature is an increment of sample absorption at 610 nm after the exposure to the burning pulses in each figure. This rise of absorption is outside the burning pulse spectrum(Fig. 8.8). We ascribe it to the formation of a photoproduct since it increases as the burning dose increases till it reaches the saturation level. Compared with the boxcar measurement above, the depletion of reactant around 620 nm must correspond to the formation of a photoproduct at 610 nm. Therefore by examining the photoproduct formation as a function of the burning pulse exposure, one could estimate the effect of stimulated emission on hole burning efficiency. Fig. 8.9 shows the absorption changes at 610 nm as a function of exposure dose in cases with and without stimulated emission. The data were extracted from the CCD spectral measurements at 610 nm. In the presence of the stimulated emission beam, the photoproduct reaches the saturation level at the exposure dose of 3 J/cm$^2$. In the absence of the stimulated emission

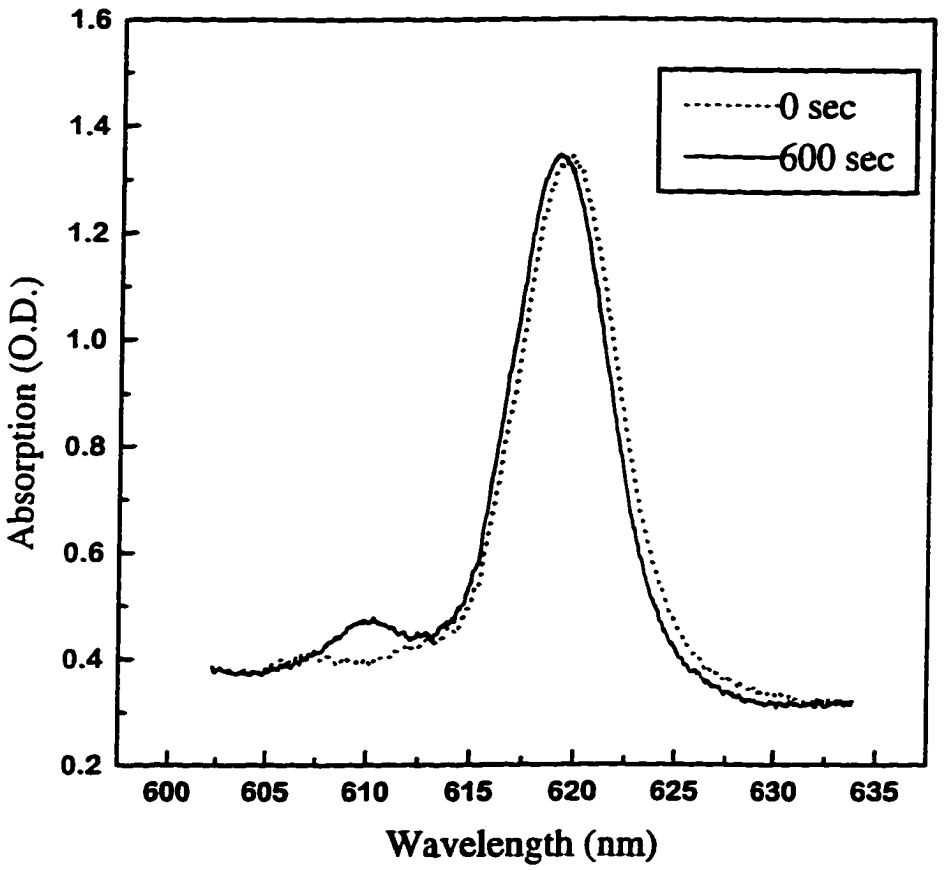


Fig. 8.6 OEP/PS absorption spectra without 680 nm stimulated emission. The dotted curve is before hole burning. The solid curve is after 600 sec exposure of burning beam.

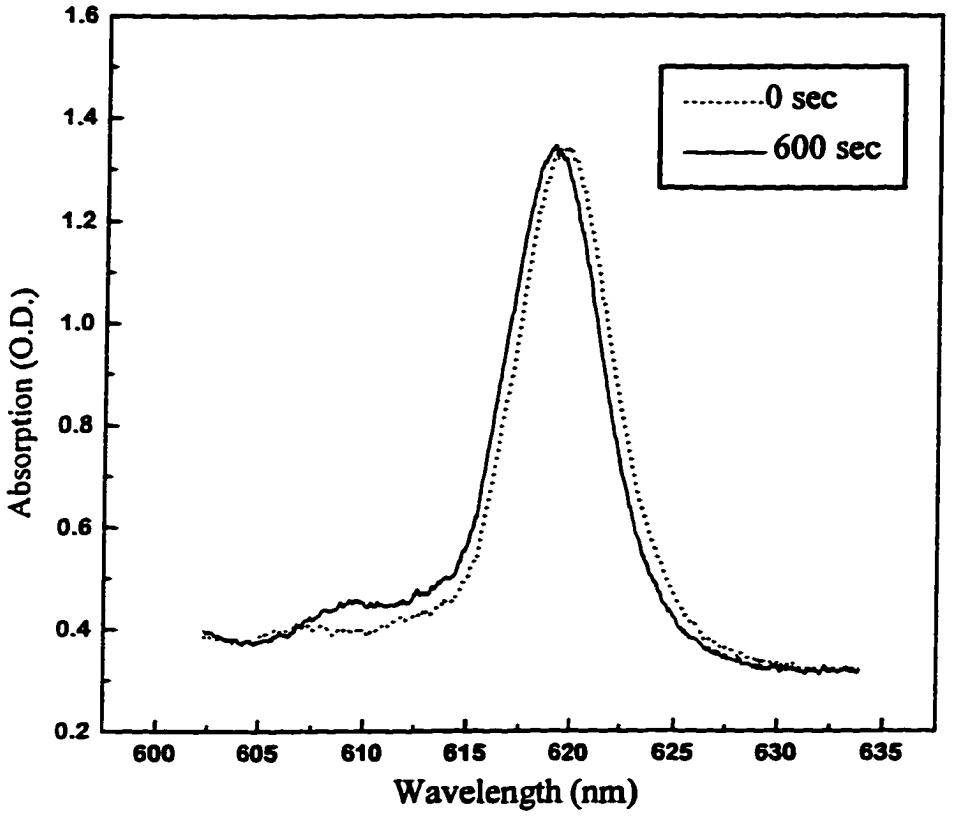


Fig. 8.7 OEP/PS absorption spectra with 680 nm stimulated emission. The dotted curve is before hole burning. The solid curve is after 600 sec exposure of burning beam.

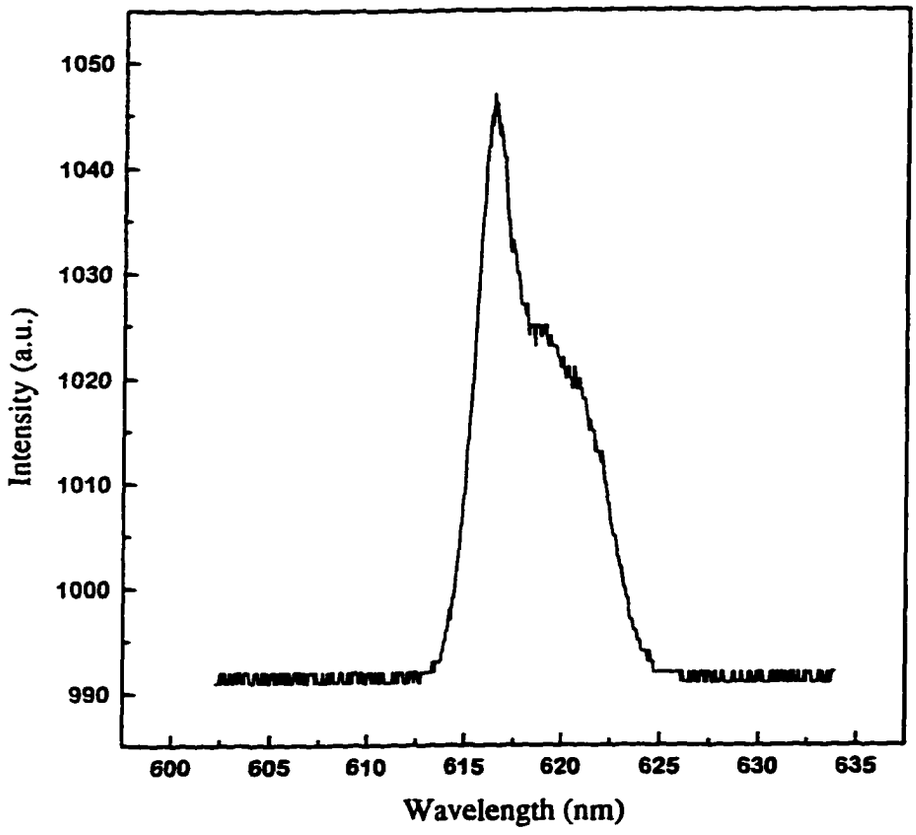


Fig. 8.8 CPM amplifier spectrum in 3-beam stimulated emission hole burning experiment.

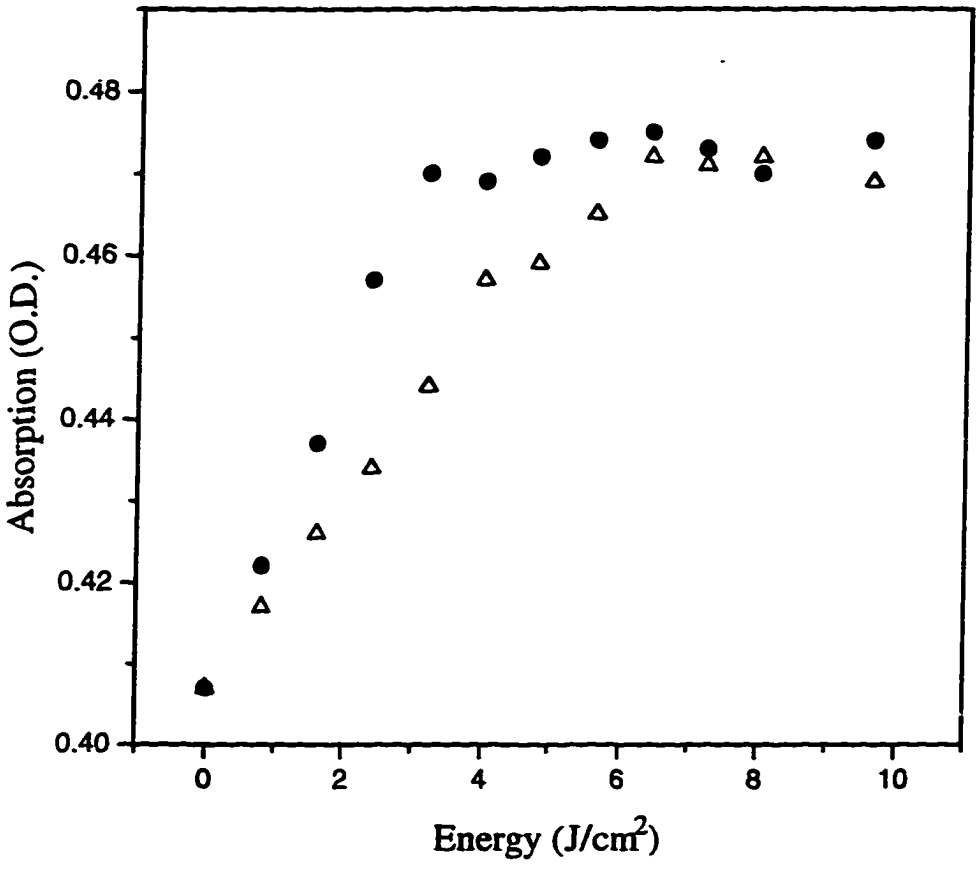


Fig. 8.9 OEP/PS absorption at 610 nm as function of burning beam doses. The triangles are without 680 nm stimulated emission. The dots are with 680 nm stimulated emission.

beam, the saturation dose is 6 J/cm$^2$. These results show that the presence of the stimulating beam would increase the hole burning efficiency at least twice, which agrees with the result in the boxcar measurement.

In conclusion, through the above two sets of experiments we found that for OEP molecules the photoreaction pathway $S_1$(reactant excited singlet state) -> $S_0^{hv}$(high vibrational level of reactant ground state) -> $S_0$(photoproduct ground state) created by stimulated emission and vibrational relaxation is more efficient than the natural pathway of $S_1$(reactant excited singlet state) -> $T_1$(first triplet manifold) -> $S_0$(photoproduct ground state) through inter-system crossing. Therefore, for optical storage material OEP or similar molecules which suffer the triplet bottleneck problem, one may achieve fast writing by using an additional beam to initiate stimulated emission, which changes the natural photoexcitation pathway and improves the hole burning efficiency, as we successfully demonstrated here.

## References


1. R. M. Macfarlane and R. M. Shelby, *Journal of Luminescence* **36**, 179(1987)

2. K. N. Solov'ev, I. E. Zalesski, V. N. Kotlo, S. F. Shkirman *JETP Lett.* **17**, 332(1973)

3. S. Volker, J. H. van der Waals *Molecular Physics* **34**, 1703(1976)

4. W. G. van Drop, S. H. Schoemaker, M. Soma and J. H. van der Waals *Molecular Physics* **30**, 1701(1975)

5. K. K. Rebane and A. A. Gorokhovsky *Journal of* Luminescence **36**, 237(1987)

6. M. Gouterman and G. Khalil *Journal of Molecular Spectroscopy* **53**, 88(1974)

7. A. T. Gradyushko and M. P. Tsvirko *Optical Spectroscopy* **31**, 291(1971)

8. A. A. Gorokhovsky, V. Kh. Korrovits, V. V. Palm and M. A. Trummal *Laser Optics of Condensed Matter* ed. by J. L. Birman *et al*, Plenum Press, New York and London(1988)

9. M. Gouterman *Optical Spectra and Electronic Structure*, The Porphyrins Vol. III, Academic Press Inc., New York(1978)

10. A private discussion with Dr. L. Rothberg

11. Grant proposal for optical storage by R. R. Alfano and A. A. Gorokhovsky

# Chapter 9

# Future Experiments

Picosecond Resonance Raman spectroscopy described in Chapter 5 successfully established the bathorhodopsin Raman modes and yields the result that bathorhodopsin is formed within 30 ps[1]. The intrinsic disadvantage of using a single laser pulse for both photolysis and Raman scattering makes it difficult to describe the time development of the structural change in detail. In contrast, time-resolved Raman techniques with one pump and one probe pulse has great flexibility in both the spectral range and time resolution. This advantage makes it a powerful tool to provide detailed direct structural information about the rhodopsin to bathorhodopsin transformation. Picosecond time-resolved resonance Raman spectroscopy has been performed in the investigation of similar retinal-containing pigment bacteriorhodopsin's J, K, and KL intermediates[2]. Similarly, by studying the "fingerprint" Raman spectral region, time-resolved Raman measurements should be able to monitor the formation of the Raman mode of bathorhodopsin and possibly the $90^0$ excited intermediate by delaying the excitation pulse with respect to the Raman scattering probe pulse. The proposed experimental strategy is as follows. An excitation pulse excites rhodopsin near its absorption peak at 500 nm to initiate the photochemical reaction. Then a time delayed second pulse is used to probe those excited vibrational modes by measuring their Raman scattering signal. The wavelength of the probe pulse can be in the absorption region of bathorhodopsin (such as

580 - 620 nm) or in the $90^0$ excited state absorption region(absorption wavelength similar to bathorhdopsin) to enhance the bathorhodopsin Raman mode. By measuring those Raman frequencies produced by both the excitation and probe pulses as a function of delay time between the two pulses, the formation detail of bathorhodopsin and the $90^0$ excited state intermediate can be obtained.

For the persistent hole burning optical storage material OEP/PS, we have successfully demonstrated ultrafast information retrieval at a working temperature(liquid helium), and performed experiments to improve writing efficiency by stimulated emission at liquid nitrogen temperature. The next step would be to perform the same experiment at a working temperature(liquid helium) and to make a direct test from a photon echo experiment. To further improve writing efficiency, a high repetition rate laser will be used. Since the triplet lifetime is ~ 1ms, this triplet bottleneck imposes the restrictions on the laser repetition rate, which must be less than 1KHz. With the stimulated emission technique provided here, this restriction no longer exists and the repetition rate is only limited by the dephasing time $T_2$. Lasers operating at 1~100 MHz can be used. We would expect several orders of magnitude improvement on writing efficiency.

## References

1. G. Hayward, W. Carlsen, A. Siegman and L. Stryer *Science* **211**, 942(1981)

2. S. J. Doig, P. J. Reid and R. A. Mathies *J. Phys. Chem.* **95**, 6372(1991)

# Appendix

## Two Pulse Photon Echo

The two pulse photon echo is the basic and simplest form of photon echo. Consider the simplest model of an atomic system, the two-level system, which is assumed to be nearly resonant with an electromagnetic field ($\omega_L \approx \omega_{21}$). The density matrix equations are[1]

$$\frac{\partial \rho_{12}}{\partial t} + (i\omega_{12} + \frac{1}{\tau_{12}})\rho_{12} = \frac{i}{\hbar}\vec{\mu}_{12}(\rho_{22} - \rho_{11})\vec{E}, \tag{A1}$$

$$\frac{\partial \rho_{22}}{\partial t} + k_{21}\rho_{22} = -\frac{i}{\hbar}(\vec{\mu}_{12}\rho_{21} - \vec{\mu}_{21}\rho_{12})\vec{E}, \tag{A2}$$

and

$$\rho_{11} + \rho_{22} = 1, \qquad \rho_{21} = \rho_{12}^{*}. \tag{A3}$$

The polarization is

$$\vec{P} = N\,\mathrm{Tr}(\rho\vec{\mu}) = \vec{P}^{NL} + \vec{P}^{LR} = N(\rho_{12}\vec{\mu}_{21} + \rho_{21}\vec{\mu}_{12}). \tag{A4}$$

After splitting off rapidly varying factors according to

$$\vec{E} = \tfrac{1}{2}A_L\vec{e}_L e^{i(\omega_L t - k_L z)} + C.C., \quad \rho_{12} = \tilde{\rho}_{12}e^{i(\omega_L t - k_L z)} \tag{A5}$$

and neglecting fast oscillating terms which do not make any essential contribution in the equation of motion, we obtain for $\tilde{\rho}_{12}$

$$\frac{\partial \tilde{\rho}_{12}}{\partial t} + [\frac{1}{\tau_{21}} + i(\omega_L - \omega_{21})]\tilde{\rho}_{12} = \frac{i}{2\hbar}\vec{\mu}_{12}\vec{e}_L(\rho_{22} - \rho_{11})A_L, \tag{A6}$$

which in the zero field case ($A_L = 0$) yields the solution

$$\tilde{\rho}_{12}(t) = \tilde{\rho}_{12}(t_0)e^{-[\frac{1}{T_2}+i(\omega_L-\omega_{21})](t-t_0)}, \tag{A7}$$

where

$$\tilde{\rho}_{12}(t_0 = 0) = -\frac{i}{2}\mu_{12}. \tag{A8}$$

For the difference of the diagonal elements of the density matrix, $\Delta\rho(t) \equiv 0$ holds after the action of the ($\pi$/2)-pulse, which produced $\Delta\rho(0) = 0$. Hence the polarization amplitude is

$$\bar{P}(t) = 2\mu_{12}N\int_{-\infty}^{\infty} d\omega_{21}\tilde{\rho}_{12}(t,\omega_{21})g_{inh}(\omega_{21}-\omega_{21}^0) \tag{A9}$$

where $g_{inh}(\omega_{21}-\omega_{21}^0)$ is the inhomogeneous line shape. Setting $\omega_{21}-\omega_{21}^0 = \omega'$ and $\omega_L = \omega_{21}^0$ and inserting $\tilde{\rho}_{12}(t)$ from (A7)

$$\bar{P}(t) = \bar{P}(0)e^{-t/T_2}\int_{-\infty}^{\infty} d\omega' g_{inh}(\omega')e^{i\omega' t}, \tag{A10}$$

where $\bar{P}(0) = -iN\mu_{12}$.

This amplitude is destroyed in times of the order of $2\pi/\Delta\omega_{inh}$ because the monotonically decreasing Fourier transform of $g_{inh}(\omega')$ for t>0 has already taken on a small value.

Now, an extremely short $\pi$-pulse is irradiated with a delay $t_d$ with respect to the first pulse ($(1/\Delta\omega_{inh}) << t_d \leq T_2$). Immediately after the $\pi$-pulse we obtain

$$\tilde{\rho}_{12}(t_D) = -\tilde{\rho}_{12}(0)e^{-\frac{t_d}{T_2}}e^{i(\omega_L-\omega_{21})t_d}. \tag{A11}$$

Thus from (A7)

$$\tilde{\rho}_{12}(t) = -\tilde{\rho}_{12}(0)e^{-\frac{t}{T_2}}e^{-i(\omega_L-\omega_{21})(t-2t_d)}. \qquad \text{(A12)}$$

From (A9) we obtain the macroscopic polarization, which for $t > t_d$, i.e. after the action of the π-pulse, is thus given by

$$\overline{P}(t) = \overline{P}(0)e^{-t/T_2}\int_{-\infty}^{\infty} d\omega' g_{inh}(\omega')e^{i\omega'(t-2t_d)}. \qquad \text{(A13)}$$

After the doubled delay time $t = 2t_d$ the polarization becomes

$$\overline{P}(t) = \overline{P}(0)e^{-2t_d/T_2}, \qquad \text{(A14)}$$

where the normalization condition $\int_{-\infty}^{\infty} d\omega' g_{inh}(\omega') = 1$ was used. Obviously the initial state is reproduced apart from the relaxation factor $\exp(-2t_d/T_2)$. Therefore, a strong emission can again occur after the time $2t_d$ due to a collective radiation effect. This phenomenon is called photon echo. As long as the duration of the process is small compared to the optical dephasing time $T_2$, it is possible to reproduce the original state. First use a short pulse whose area equals π/2 (to maximize the polarization) to excite the sample, then use a π pulse to reverse the polarization phase 180° at a delay time $t_d < T_2$. One should observe a strong emission of light(echo) at $2t_d$, see figure A1. The amplitude of the two-pulse echo is proportional to $\exp(-2t_d/T_2)$ for inhomogeneously broadened materials. Thus, by measuring the echo intensity as a function of time delay $t_d$, $T_2$ can be determined.

In photon echoes, the wave propagation effect is also important. Consider a light pulse detected by a detector at $\vec{r} = 0$ and time $t$, the actual interaction of the pulse with

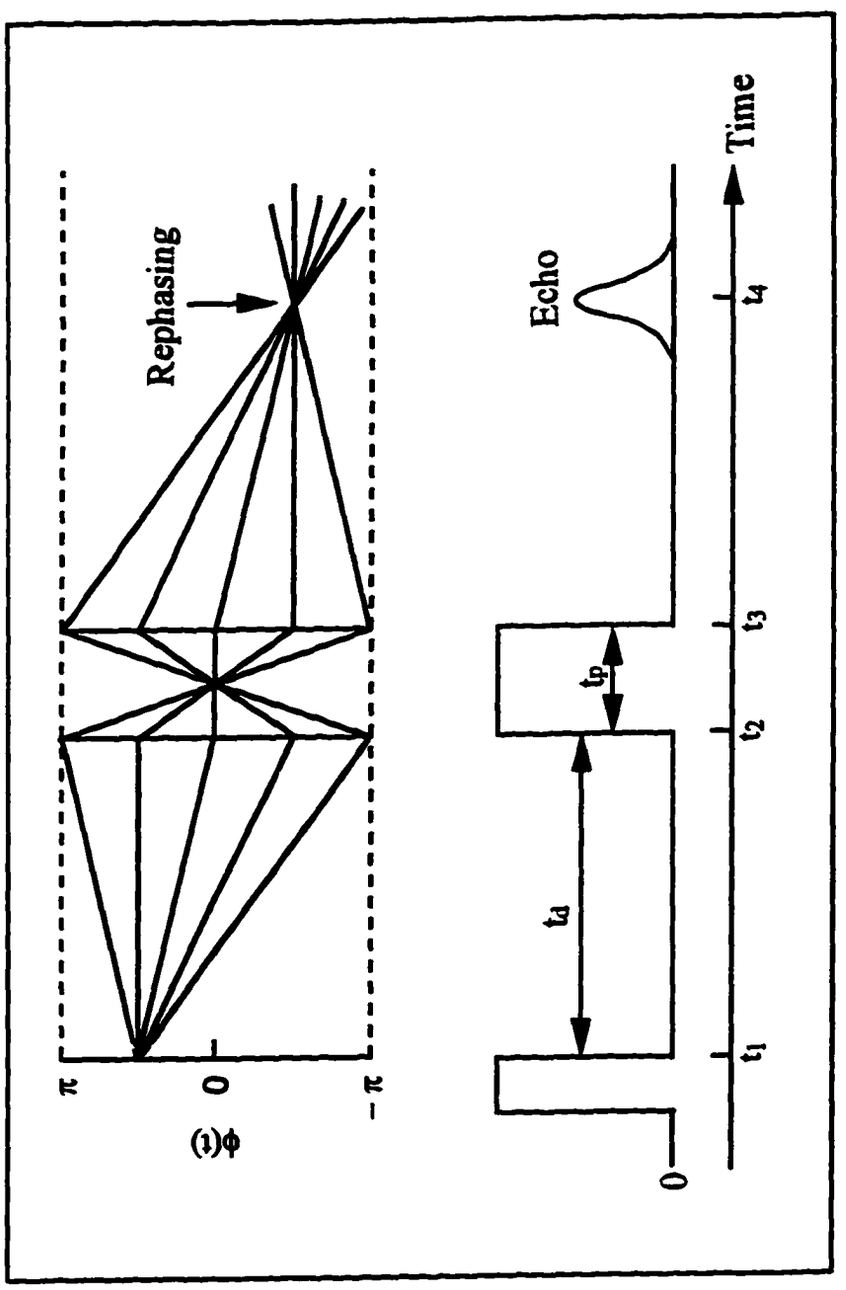


Fig. A1 The principle of the two-pulse photon echo.

the atoms at $\vec{r}$ occurs at the retarded time $t-\vec{k}\cdot\vec{r}/\omega$. Thus, more correctly, retarded time should be used in the above discussion. The photon echo should then appear when[2]

$$(t_4-\vec{k}_4\bullet\frac{\vec{r}}{\omega})-(t_3-\vec{k}_2\bullet\frac{\vec{r}}{\omega})=(t_2-\vec{k}_2\bullet\frac{\vec{r}}{\omega})-(t_1-\vec{k}_1\bullet\frac{\vec{r}}{\omega}) \qquad \text{(A15)}$$

where $t_1$, $t_2$, $t_3$ and $t_4$ are times at the end of the ($\pi$/2)-pulse, the beginning of the $\pi$-pulse, the end of the $\pi$-pulse and the middle of the echo, and $k_1$, $k_2$ and $k_4$ are, respectively, the wavevectors of the ($\pi$/2)-pulse, the $\pi$-pulse and the photon echo. Equation (A15) yields the conditions for the photon echo:

$$t_4-t_3=t_2-t_1 \qquad \text{and} \qquad \vec{k}_4=2\vec{k}_2-\vec{k}_1. \qquad \text{(A16)}$$

The second condition in (A16) is actually the phase-matching requirement for the generation of the photon echo.

## References

1. Joachim Herrmann and Bernd Wilhelmi *Lasers For Ultrashort Light Pulses*, Akademie-Verlag Berlin 1987.

2. Y. R. Shen *The Principles Of Nonlinear Optics*, John Wiley & Sons, New York(1984)

# Bibliography

R. J. Abraham, G. E. Hawkes and K. M. Smith *Tetrahedron Leet.* **16**, 1483(1974)

R. R. Alfano *The Supercontinuum Laser Source*, Springer-Verlag New York(1989)

R. R. Alfano ed. *Biochemical events Probed by Ultrafast Laser Spectrascopy*, Academic Press, San Diego(1982)

R. R. Alfano and S. L. Shapiro *Phys. Rev. Lett.* **24**, 584(1970)

B. Aton, A. G. Doukas, D. Narva, R. H. Callender, U. Dinur and B. Honig *Biophys. J.* **29**, 79(1980)

B. Aton, R. H. Callender and B. Honig *Nature* **273**, 784(1978)

R. R. Birge *Biochimica Biophysica Acta* **1016**, 293(1990) and references therein

R. R. Birge *Ann. Rev. Phys. Chem.* **41**, 683(1990)

R. R. Birge, C. M. Einterz, H. M. Knapp and L. P. Murray *Biophys. J.* **53**, 367(1988)

R. R. Birge, L. M. Hubbard *Biophys. J.* **34**, 517(1981)

R. R. Birge, L. M. Hubbard *J. Am. Chem. Soc.* **102**, 2195(1980)

D. J. Bradley in *Ultrafast Laser Pulses ch2 ed. by S. L. Shapiro*, Springer-Verlag, New York(1977)

J. Buchert, V. Stefancic, A. G. Doukas, R. R. Alfano, R. H. Callender, J. Pande, H. Akita, V. Balogh-Nair and K. Nakanishi *Biophys. J.* **43**, 279(1983)

G. E. Busch, M. L. Applebury, A. A. Lamola and P. M. Rentsepis *Proc. Natl. Acad. Sci. (USA)* **69**, 2802(1972)

R. H. Callender in *Biochemical events Probed by Ultrafast Laser Spectrascopy ch9* ed by R. R. Alfano, Academic Press, San Diego(1982)

R. H. Callender, A. Doukas, R. Crouch, and K. Nakanishi *Biochemistry* **15**, 1621(1976)

G. Castro, D. Haarer, R. M. Macfarlane and H. P. Trommsdroff, U.S. patent 4,101,976(July 18, 1978)

A. Cooper *Nature (Lond.)* **282**, 531-533(1979)

S. J. Doig, P. J. Reid and R. A. Mathies *J. Phys. Chem.* **95**, 6372(1991)

A. G. Doukas, R. H. Callender and R. R. Alfano *Applications of Fluorescence in the Biomedical Sciences*, pages 69-89, Alan R. Liss, Inc.(1986)

A. G. Doukas, M. R. Junnarkar, R. R. Alfano, R. H. Callender and V. Balogh-Nair *Biophys. J.* **47**, 795(1985)

A. G. Doukas, M. R. Junnarkar, R. R. Alfano, R. H. Callender, T. Kakitani and B. Honig *Proc. Natl. Acad. Sci. (USA)* **81**, 4790(1984)

A. G. Doukas, J. Buchert and R. R. Alfano in *Biochemical events Probed by Ultrafast Laser Spectrascopy* ed by R. R. Alfano, Academic Press, San Diego(1982)

A. G. Doukas, P. Y. Lu and R. R. Alfano *Biophys. J.* **35**, 547(1981)

A. G. Doukas, V. Stefancic, T. Suzuki, R. H. Callender and R. R. Alfano *Photobiochem. Photobiophys.* **1**, 305(1980)

W. G. van Drop, S. H. Schoemaker, M. Soma and J. H. van der Waals *Molecular Physics* **30**, 1701(1975)

G. Eyring, B. Curry, A. Broek, J. Lugtenberg and R. Mathies *Biochemistry* **21**, 384(1982)

G. Eyring, B. Curry, R. Mathies, R. Fransen, I. Paling and J. Lugtenberg *Biochemistry* **19**, 2410(1980)

G.Eyring and R. Mathies *Proc. Natl. Acad. Sci. (USA)* **76**, 33(1979)

J. Favrot, J. M. Leclercq, R. Roberge, C. Sandorfy and D. Vocelle *Photochem. And Photobio.* **29**, 99(1979)

R. L. Fock *Optics Lett.* **11**, 629(1986)

R. L. Fock, O. E. Martinez and J. P. Gondon *Optics Lett.* **9**, 150(1984)

R. L. Fork, C. V. Shank, R. Yen and C. A. Hirlimann *IEEE J. Quantum Electron.* **19**, 500(1983)

R. L. Fork, C. V. Shank and R. T. Yen *Appl. Phys. Lett.* **41**, 233(1982)

R. L. Fork, B. I. Greene and C. V. Shank *Appl. Phys. Lett.* **38**, 671(1981)

A. A. Gorokhovsky, V. Kh. Korrovits, V. V. Palm and M. A. Trummal *Laser Optics of Condensed Matter* ed. by J. L. Birman *et al*, Plenum Press, New York and London(1988)

A. A Gorokhovsky, R. K Kaarli, L. A. Rebane *JEPT Lett.* **20**, 216(1974)

M. Gouterman *Optical Spectra and Electronic Structure*, The Porphyrins Vol. III, Academic Press Inc., New York(1978)

M. Gouterman and G. Khalil *Journal of Molecular Spectroscopy* **53**, 88(1974)

A. T. Gradyushko and M. P. Tsvirko *Optical Spectroscopy* **31**, 291(1971)

B. H. Green, T. G. Monger, R. R. Alfano, B. Aton and R. H. Callender *Nature(london)* **269**, 179(1977)

B. Green, T. Monger, R. Alfano, B. Aton and R. Callender *Nature (London)* **264**, 179(1977)

B. I. Greene, J. Orenstein, R. R. Millard and L. R. Williams *Chem.Phys. Lett.* **139**, 381(1987)

G. Hayward, W. Carlsen, A. Siegman and L. Stryer *Science* **211**, 942(1981)

Joachim Herrmann and Bernd Wilhelmi *Lasers For Ultrashort Light Pulses*, Akademie-Verlag Berlin(1987)

W. H. Hesselink and D. A. Wiersma *Phys. rev. Lett.* **43**, 1991(1979)

R. M. Hochstrasser and C. K. Johnson in *Ultrafast Laser Pulses and Applications ed. by W. Kaiser*, Topics in Applied Physics **60**, Springer-Verlag, New York(1988)

B. Honig, T. Ebrey, R. H. Callender, U. Dinur and M. Ottolenghi *Proc. Natl. Acad. Sci. U.S.A.* **76**, 2503(1979)

E. P. Ippen and C. V. Shank in *Ultrashot light Pulses* ed by S. L. Shapiro, Springer-Verlag, New York(1977)

J. D. Kafka and T. Baer *Optics Lett.* **6**, 401(1987)

H. Kandori, S. Matuoka, Y. Shichida and T. Yoshizawa *Photochem. Photobiol.* **49**, 181(1989)

H. Kandori, Y. Shichida and T. Yoshizawa *Biophys. J.* **56**, 453(1989)

B. M. Kharlamov, R.I. Personov, L. A. Bykovskaya *Opt. Commun.* **12**, 191(1974)

M. D. Levenson in *Introduction to Nonlinear Spectroscopy*, Academic Press, San Diego(1981)

A. Lewis and L. V. Del Priore *Phys. Today* **Jan.**, 38(1988)

A. Lewis *Proc. Natl. Acad. Sci. (USA)* **75**, 549(1978)

G. R. Loppnow and R. A. Matehies *Biophys. J.* **54**, 35(1988)

R. M. Macfarlane and R. M. Shelby, *Journal of Luminescence* **36**, 179(1987)

R. A. Mathies, S. O. Smith and I. Palings in *Biological Applications Of Raman Spectroscopy ch2 ed. by T. G. Spiro*, John Wiley & Sons, Inc., New York(1987)

K van der Meer, J. J. C. Mulder and J. Lugtenberg *Photochem. And Photobio.* **24**, 363(1976)

T. W. Mossberg *Opt. Lett.* **7**, 77(1982)

T. G. Monger, R. R. Alfano and R. H. Callender *Biophys. J.* **27**, 105(1979)

A. R. Oseroff and R. H. Callender *Biochemistry* **13**, 4243(1974)

I. Paling, J. A. Pardoen, E. van den Berg, C. Winkel, J. Lugtenberg and R. Mathies *Biochemistry* **26**, 2545(1987)

L. A. Peteanu, R. W. Schoenlein, Q. Wang, R. A. Mathies and C. V. Shank *Proc. Natl. Acad. Sci. (USA)* **90**, 11762(1993)

K. Peters, M. Applebury and P. Rentzepis *Proc. Natl. Acad. Sci. U.S.A.* **74**, 3119(1977)

A. Popp, L. Ujj and G. H. Atkinson *Journal of Physical Chemistry* **99**, 10043(1995)

K. G. Purchase, D. J. Brady and K. Wagner *Optics Letters* **18**, 2129(1993).

A. Rebane, J. Aaviksoo and J. Kuhl *Appl. Phys. Lett.* **54**, 93(1989)

A. Rebane and D. Haarer, *Optics Communication* **70**, 478(1989)

K. K. Rebane and A. A. Gorokhovsky *Journal of* Luminescence **36**, 237(1987)

L. A. Rebane, A. A. Gorokhovsky and J. V. Kikas *Appl. Phys.* **B29**, 235(1982)

P. M. Rentzpis *Science* **202**, 174(1978)

T. Rosenfeld, B. Honig, M. Ottolenghi, j. Hurley and T. G. Ebrey *Pure Appl. Chem.* **49**, 341(1977)

P. Saari, R. Kaarli and A. Rebane *Opt. Spektrosk* **56**, 387(1984)

F. Salin and A. Brun *J. Appl. Phys.* **61**, 4736(1987)

G. A. Schick, T. M. Cooper, R. A. Holloway, L. P. Murray and R. R. Birge *Biochemistry* **26**,2556-2562(1987)

R. W. Schoenlein, L. A. Peteanu, Q. Wang, R. A. Mathies and C. V. Shank *J. Phys. Chem.* **97**, 12087(1993)

R. W. Schoenlein, L. A. Peteanu, R. A. Mathies, C. V. Shank *Science* **254**, 412(1991)

C. V. Shank in *Ultrafast Laser Pulses and Applications ed. by W. Kaiser*, Topics in Applied Physics **60**, Springer-Verlag, New York(1988)

S. L. Shapiro ed. *Ultrashot light Pulses*, Springer-Verlag, New York(1977)

Y. R. Shen *The Principles Of Nonlinear Optics*, John Wiley & Sons New York(1984)

Y. Shichida, S. Matuoka and T. Yoshizawa *Photobiochem. Photobiophys.* **7**, 221(1984)

K. N. Solov'ev, I. E. Zalesski, V. N. Kotlo, S. F. Shkirman *JETP Lett.* **17**, 332(1973)

M. Stix and E. P. Ippen *IEEE J.* **19**, 250(1983)

A. Stylere *Biochemistry* 3rd Edition, John Wiley & Sons, New York(1990)

A. Szabo, U.S. patent 3,896,420(July 22, 1975)

K. Taiji, K. Bryl, M. Nakagawa, M. Tsuda and T. Kobayashi *Photochem. Photobiol.* **56**, 1003(1992)

J. R. Tallent, E. W. Hyde, L. A. Findsen, G. L. Fox, R. R. Birge *J. Am. Chem. Soc.* **114**, 1581(1992)

J. T. Verdeyen *Laser Electronics* Prentice-Hall, New Jersey(1981)

S. Volker, J. H. van der Waals *Molecular Physics* **34**, No. 6, 1703(1976)

George Wald *Nature* **219**, 800(1968)

George Wald *Science* **162**, 230(1968)

Q. Wang, R. W. Schoenlein, L. A. Peteanu, R. A. Mathies and C. V. Shank *Science* **266**, 422(1994)

R. M. Weiss and A. Warshel *J. Am. Chem. Soc.* **101**, 6131(1979)

A. Warshel *Proc. Natl. Acad. Sci. (USA)* **75**, 2558(1978)

A. Warshel *Nature* **260**, 679(1976)

M. Yan, D. Manor, R. R. Alfano and R. H. Callender, L. J. Rothberg *Proc. of the International Conference on Lasers '92, Dec. 7 - 10*, 422(1992)

M. Yan and R. R. Alfano *Bio-Laser News* (Spring 1992)

Ming Yan, D. Manor, G. Weng, H. Chao, L. Rothberg, T. M. Jedju, R. R. Alfano and R. H. Callender *Proc. Natl. Acad. Sci. (USA)* **88**, 9809(1991)

A. Yariv *Quantum Electronics* 3rd Ed., Wiley, New York(1989)

T. Yoshizawa and G. Wald *Nature (Lond.)* **197**, 1279(1963)

I. Zeylikovich, G. Bai, A. Gorokhovsky and R. R. Alfano *Optics Letters* **20**, 749(1995).

I. Zeylikovich, Q. D. Liu, G. Bai, N. Zhadin, A. Gorokhovsky and R. R. Alfano *Opt. Commun.* **115**, 485(1995).

S. P. Zurer *C&EN Washington* **Nov.**, 25(1983)

# List of Publications


1. "Intermediate excited states in rhodopsin photochemistry", L. J. Rothberg, M. Yan, T. M. Jedju, R. H. Callender, G. Bai, R. R. Alfano *APS March Meeting/Session J23*(1996).

2. "The initial photochemistry of vision", Ming Yan, Louis Rothberg, Guang Bai, T. M. Jedju, Robert Alfano, Robert Birge, and Robert Callender. To be submitted.

3. "Spectral and time domain studies of accumulated photon echo", I. Zeylikovich, G. Bai, A. Gorokhovsky and R. R. Alfano *Molecular Crystals and Liquid Crystals* **291**, 277(1996)

4. "Ultrafast retrieval of femtosecond photon echo signal", I. Zeylikovich, G. Bai, A. Gorokhovsky and R. R. Alfano *OSA Annual Meeting/ILS-XI Program*(1995)

5. "Real time observation of light diffraction by femtosecond correlation interferometry", I. Zeylikovich, G. Bai and R. R. Alfano *OSA Annual Meeting/ILS-XI Program*(1995)

6. "Observation of light diffraction by time-resolved femtosecond correlation interferometry", I. Zeylikovich, G. Bai and R. R. Alfano *Optics Letters* **20**, 1580(1995)

7. "Terabit speed retrieval of femtosecond accumulated photon echoes", I. Zeylikovich, G. Bai, A. Gorokhovsky and R. R. Alfano *Optics Letters* **20**, 749(1995)

8. "Interferometric 2D imaging amplitude correlator for ultrashort pulses", I. Zeylikovich, Q. D. Liu, G. Bai, N. Zhadin, A. Gorokhovsky and R. R. Alfano *Opt. Commun.* **115**, 485(1995)

9. "Spontaneous photon-emission spectrum of tunneling electrons in a double-barrier structure", Guang Bai, Kai Shum and R. R. Alfano *J. Appl. Phys.* **70**(2), 1025(1991)